THE PENETRATION BEHAVIOR OF REPEATED HEMISPHERE CORE SANDWICH STRUCTURES: AN EXPERIMENTAL AND NUMERICAL STUDY

A Thesis Submitted to
The Graduate School of Engineering and Sciences of
İzmir Institute of Technology
in Partial Fulfillment of the Requirements for the Degree of

DOCTOR OF PHILOSOPHY

in Mechanical Engineering

by
Ali Kıvanç TURAN

July 2018
İZMİR

We approve the thesis of **Ali Kıvanç TURAN**

Examining Committee Members:

Prof. Dr. Alper TAŞDEMİRCİ
Department of Mechanical Engineering, İzmir Institute of Technology

Prof. Dr. Meltem Evren TOYGAR
Department of Mechanical Engineering, Dokuz Eylül University

Assoc. Prof. Dr. H. Seçil ARTEM
Department of Mechanical Engineering, İzmir Institute of Technology

Prof. Dr. Hasan YILDIZ
Department of Mechanical Engineering, Ege University

Assist. Prof. Dr. Selçuk SAATCI
Department of Civil Engineering, İzmir Institute of Technology

05 July 2018

Prof. Dr. Alper TAŞDEMİRCİ
Supervisor, Department of
Mechanical Engineering
İzmir Institute of Technology

Prof. Dr. Mustafa GÜDEN
Co-Supervisor, Department of
Mechanical Engineering
İzmir Institute of Technology

Prof. Dr. Metin TANOĞLU
Head of the Department of
Mechanical Engineering

Prof. Dr. Aysun SOFUOĞLU
Dean of the Graduate School of
Engineering and Sciences

ACKNOWLEDGEMENTS

First of all, I would like to thank my advisor Prof. Dr. Alper Taşdemirci for his patience and supportive manner throughout the study. His motivational acts and guidance is very much appreciated during the work presented in this thesis. I would like to propose my sincere and warm regards as I have learned a lot from him during my MSc. and PhD training. I also would like to thank my co-advisor Prof. Dr. Mustafa Güden for all of his efforts and support on understanding the key characteristics of investigated geometries. I would like to thank TUBITAK for the grant number 112M141 and IYTE for grant number 2013IYTE18 for financial support of the study.

I'm thankful for the support of Delphi Technologies Powertrain Division, fuel rail product engineering team manager Ernur Kazancı, Taner Bekar and Bora Iyiuyarlar on my PhD programme. Special thanks to our team's FEA engineer Bekir Han Biçim for fruitful conversations on modeling of experimental study, Emre Tavkaya and Nihat Sert for their support.

I would like to thank my colleagues Doğuş Zeren, Kutlay Odacı, Ali Kara, Selim Şahin, Atacan Yücesoy, Onur Yenigün, Tümcan Şen, Mümine Gerçek, Alper Çankaya and Mustafa Karaman for their great friendship through the years I work as a Res. Assist. at IZTECH. Presence and support of you helped me keep my motivation high during the study. Also, I'm very happy for having a chance to meet the researchers Fulya Akbulut, Erkan Güzel, Fırat Tüzgel, Çetin Uysal, Semih Berk Seven and Mustafa Kemal Sarıkaya; thank you all for good memories.

This study, as the ones before, is dedicated to my beautiful family. I would like to express my gratitude to my father Yavuz Selim Turan and my mother Hülya Turan for their absolute guidance and moral support in every condition; without them it would not be possible to complete this study. I also would like to say thank you to Onur Turan and Senem Turan for cheering me up in every situation I felt losing the track.

Last but not least, I'm thankful for the love and support of my lady and my beloved wife, Selin Turan. Her understanding of long work hours and studies even on weekends enabled me to complete this thesis.

ABSTRACT

THE PENETRATION BEHAVIOR OF REPEATED HEMISPHERE CORE SANDWICH STRUCTURES: AN EXPERIMENTAL AND NUMERICAL STUDY

In this study, penetration behavior of novel core structure consisting hemispherical and cylindrical parts was investigated. Core units were manufactured with deep drawing method in two thicknesses to have monolithic form without any sort of assembly method or element. Produced specimens were then subjected to penetration tests at low and intermediate velocities against blunt, conical and hemispherical tipped indenters using special fixtures and apparatuses on conventional testing equipment. Effect of heat treatment on penetration behavior was investigated to observe whether residual stresses arise from manufacturing process changes the penetration behavior. Confinement effects were studied experimentally with a special fixture, allowing tested specimen to be radially confined with other core units as in an armor structure. Finally, experimental work was finished by conducting a case study where core units were subjected to spherical projectile impact up to impact velocities of 180 $m.s^{-1}$ in a composite sandwich structure. Results show that each indenter geometry showed unique deformation characteristics in testing of both core units and both of the core geometries were able to hold a steel spherical projectile with mass of 110 g without full perforation at impact velocity of 180 $m.s^{-1}$. Details of experimental results were presented in each chapter.

Study also included modeling parts where core units were numerically produced with residual stresses and strains and good correlation was noted where thickness was compared with actual measurements on core units. Test conducted on single core structure in as-received and heat-treated condition were also repeated in numerical environment, where numerical study exhibited good correlation on both force-displacement curves and deformation of core units with tests. Correlation achieved with experimental study has led into further investigations of strain rate and micro-inertia where behavior of core units was studied at numerical impact velocities of 300 $m.s^{-1}$. Results show that both strain rate and micro-inertia increase the local maximums and average of force levels. Effect of strain rate and micro-inertia is clearly distinguished for a threshold displacement level where micro-inertia is further dominant on behavior.

ÖZET

TEKRARLI YARIMKÜRE ÇEKİRDEKLİ SANDVİÇ YAPILARIN PENETRASYON DAVRANIŞI: DENEYSEL VE SAYISAL BİR ÇALIŞMA

Bu çalışmada, yarıküre ve silindirik kısımlardan oluşan yeni bir çekirdek yapının delinme davranışı incelenmiştir. Çekirdek yapılar monolitik yapıda olup herhangi bir montaj yöntemi ya da elemanı olmadan derin çekme metodu ile iki farklı kalınlıkta üretilmiştir. Üretilen numuneler daha sonra düz, konik ve yarıküresel uçlu delicilerle konvansiyonel test ekipmanları ve özel fikstürler kullanılarak düşük ve orta hızlarda delinme testlerine maruz bırakılmıştır. Üretim metodundan gelen kalıntı gerilme ve birim şekil değştirmelerin delinme davranışına etkilerinin olup olmadığı da ısıl işlemin delinme davranışına etkileri ile araştırılmıştır. Sınırlandırma şartlarının delinme davranışına etkisi de özel bir fikstür yardımıyla deneysel olarak incelenmiş ve test edilen numunenin bir zırh yapısındaki gibi çekirdek yapılarla etrafının radyal olarak sarılması sağlanmıştır. Son olarak deneysel çalışma bir vaka çalışması ile tamamlanmış ve çekirdek yapılar kompozit bir sandviç yapı içerisinde 180 $m.s^{-1}$ çarpma hızlarına kadar küresel projektil çarpmasına maruz bırakılmıştır. Sonuçlar her delici geometrisinin her çekirdek yapı için kendine has deformasyon karakteristiğini gösterdiğini ve iki çekirdek geometrisinin de 110 g ağırlıklı küresel projektili 180 $m.s^{-1}$ çarpma hızlarına kadar tam delinme olmaksızın tutabildiğini göstermiştir. Deneysel sonuçlar her bölümde sunulmuştur.

Çalışma ayrıca modelleme çalışmalarında da çekirdek yapıların kalıntı gerilme ve birim şekil değiştirmeler ile nümerik olarak modellenmesini içermiş, kalınlık değerlerinde gerçek ölçümlerle uyum yakalanmıştır. Üretildiği gibi ve ısıl işlemli tekli çekirdek yapıda tamamlanan testler nümerik ortamda da tekrarlanmış, nümerik sonuçlarda hem kuvvet-yer değiştirme hem de hasar şekillerinde deneysel çalışmayla uyum görülmüştür. Elde edilen bu uyum saesinde ileri araştırmalarla delinme davranışıdaki birim şekil değiştirme ve mikro-atalet etkileri de 300 $m.s^{-1}$ nümerik çarpma hızlarında incelenmiştir. Sonuçlar hem birim şekil değiştirme hızının hem de mikro ataletin lokal ve ortalama kuvvet değerlerini arttırdığını ortaya koymuştur. Birim şekil değiştirme hızı ve mikro-atalet etkilerinin farkı sınır bir yer değiştirme değerinden sonra ayrıştırılır hale gelmiş ve mikro-atalet etkilerinin baskın olduğu görülmüştür.

TABLE OF CONTENTS

LIST OF FIGURES ix

LIST OF TABLES xv

CHAPTER 1. INTRODUCTION 1

1.1. Introduction 1

1.2. Aim of the Study 2

1.3. Scope of the Study 2

CHAPTER 2. LITERATURE SURVEY 4

2.1. Indentation & Penetration of Shell Structures 4

2.2. Penetration of Sandwich Structures with Various Core Materials 15

CHAPTER 3. MANUFACTURING OF INVESTIGATED STRUCTURE AND SPECIAL TESTING EQUIPMENT 27

3.1. Manufacturing of Core Structure 27

3.1.1. Manufacturing of Combined Geometry Shells 28

3.2. Manufacturing of Composite Face Sheets 30

3.3. Manufacturing of Special Testing Equipment 31

CHAPTER 4. MECHANICAL CHARACTERIZATION AND PERFORMANCE EVALUATION TESTS OF CORE STRUCTURE 34

4.1. Mechanical Characterization of 304 L Stainless Steel 34

4.1.1. Quasi-Static Strain Rate Tests 34

4.1.2. High Strain Rate Tests 35
4.2. Results of Mechanical Characterization Studies 37
4.2.1. Johnson-Cook Constitutive Equation 38
4.3. Performance Evaluation Tests of Core Structure 42
4.3.1. Tests of R75t1 Structure 42
4.3.2. Tests of R75t05 Structure 47
4.3.3. Investigation of Deformation Progress on Performance Evaluation Tests 51
4.4. Numerical Studies on Performance Evaluation Tests 58
4.5. Strain Rate and Micro-inertia Effects 70

CHAPTER 5. EXPERIMENTAL AND NUMERICAL INVESTIGATION OF EFFECT OF HEAT TREATMENT ON PENETRATION BEHAVIOR 73
5.1. Heat Treatment of Core Structures 73
5.2. Performance Evaluation Tests of Heat Treated Core Structure 74
5.3. Numerical Studies on Performance Evaluation Tests of Heat Treated Core Structure 80

CHAPTER 6. INVESTIGATION OF EFFECT OF CONFINEMENT ON PENETRATION BEHAVIOR 82
6.1. Materials and Method 82
6.2. Performance Evaluation Tests of Radially Confined Core Units 83

CHAPTER 7. INVESTIGATION OF PERFORMANCE OF CORE STRUCTURE AGAINST BALLISTIC TESTS 95
7.1. Materials and Method 95
7.2. Ballistic Tests of Core Structure 97

CHAPTER 8 104

CONCLUSIONS 104

REFERENCES 109

LIST OF FIGURES

Figure **Page**

Figure 1.1. Some examples of IEDs made from (a) plastic bottles filled with explosives 1

Figure 2.1. Schematic of indenters ranging from point to plate load 5

Figure 2.2. Change in deformation with increase in ratio of thickness to radius 5

Figure 2.3. Unsymmetrical buckling observed in experimental study 6

Figure 2.4. Unsymmetrical buckling observed in experimental study 6

Figure 2.5. Analytical calculation of deformation under rigid body 7

Figure 2.6. Analytical calculation of deformation under compressive plate 7

Figure 2.7. Progress of deformation on steel and bronze shells 8

Figure 2.8. Comparison of initial collapse loads for different boss sizes from experimental, numerical and analytical results for investigated materials, bronze on the right 9

Figure 2.9. Comparison of experimental and numerical results against loading from square bar and circular bar 9

Figure 2.10. Comparison of analytical and experimental study. 11

Figure 2.11. Comparison of experimental and numerical results 12

Figure 2.12. Comparison of numerical (a) and experimental (b) results with analytical calculations 13

Figure 2.13. Comparison of experimental and numerical damage 14

Figure 2.14. Comparison of experimental and numerical load-displacement curves 14

Figure 2.15. Tested sandwich structure 16

Figure 2.16. Comparison of experimental and numerical deformation 17

Figure 2.17. Effect of strain rate on (a) Damage modes, (b) Energy Dissipation levels 18

Figure 2.18. Comparison of experimental and numerical results in terms of (a) residual velocities (b) deformation profile (on the left, blunt-nosed projectile; on the right, hemispherical-nosed projectile). 20

Figure 2.19. Test set-up, projectile geometries and fixturing types applied in the study 22

Figure 2.20. Schematic of experimental set-up used in the study 23

Figure 2.21. Comparison of ballistic limit velocities 24

Figure 2.22. Composite layers (a) and spherical structures (b) used as arrays in the study 25
Figure 2.23. Energy absorption percentages of proposed structure 26
Figure 3.1. Technical drawings and exact images of core structures. 28
Figure 3.2. Measured thickness variation contours of combined geometry shells; (a) R75T1, (b) R75T05 specimens 29
Figure 3.3. Manufacturing of composite plates using VARTM method. 30
Figure 3.4. Composite plates after surface grinding operation. 31
Figure 3.5. Penetrators used in tests at (a) quasi-static, (b) intermediate strain rates. 32
Figure 3.6. Specimen fixture with single core and radial confinement set-ups. 33
Figure 4.1. Specimens used in mechanical characterization studies. 35
Figure 4.2. Split Hopkinson Tension Bar used in high strain rate tests. 35
Figure 4.3. SHTB voltage history of a test done on AISI 304L stainless steel. 36
Figure 4.4. Quasi-static true stress – true plastic strain curves. 39
Figure 4.5. High strain rate behavior of 304 L stainless steel. 40
Figure 4.6. Curve fitting of test results. 41
Figure 4.7. Strain rate sensitivity of AISI 304L stainless steel. 41
Figure 4.8. Comparison of test results of R75t1 structure against blunt tipped indenter. 43
Figure 4.9. Comparison of test results of R75t1 structure against conical tipped indenter. 44
Figure 4.10. Comparison of test results of R75t1 structure against hemispherical tipped indenter. 44
Figure 4.11. Comparison of test results of R75t1 structure against various indenters. .. 45
Figure 4.12. Effect of increasing cross-head velocity on the penetration behavior of R75t1 core structure against blunt tipped indenter. 46
Figure 4.13. Effect of increasing cross-head velocity on the penetration behavior of R75t1 core structure against conical tipped indenter. 47
Figure 4.14. Comparison of test results of R75t05 structure against blunt tipped indenter. 47
Figure 4.15. Comparison of test results of R75t05 structure against conical tipped indenter. 48
Figure 4.16. Comparison of test results of R75t05 structure against hemisphere tipped indenter. 49

Figure 4.17. Comparison of test results of R75t05 structure against various indenters. 49
Figure 4.18. Comparison of test results of R75t05 structure against blunt tipped indenter at low and intermediate velocity levels. 50
Figure 4.19. Comparison of test results of R75t05 structure against conical tipped indenter at low and intermediate velocity levels. 51
Figure 4.20. Deformation progress of R75t1 specimen against blunt tipped penetrator. 52
Figure 4.21. Deformation progress of R75t1 specimen against conical tipped penetrator (0.013 $m.s^{-1}$). 53
Figure 4.22. Progress of deformation of R75t1 specimen against conical tipped penetrator (0.13 $m.s^{-1}$). 54
Figure 4.23. Deformation progress of R75t1 specimen against hemispherical tipped penetrator. 55
Figure 4.24. Force-displacement curves of R75t05 specimen and deformation progress against blunt tipped penetrator. 56
Figure 4.25. Force-displacement curves of R75t05 specimen and deformation progress against conical tipped penetrator. 57
Figure 4.26. Force-displacement curves of R75t05 specimen and deformation progress against hemispherical tipped penetrator. 58
Figure 4.27. Finite element model of deep-drawing method. 59
Figure 4.28. (a) Thickness change of R75 t1 specimen, (b) comparison of measured and numerical thicknesses 60
Figure 4.29. Finite element model of core structure against various types of indenters. 61
Figure 4.30. Comparison of experimental and numerical force-displacement curves of R75t1 core structure against blunt tipped indenter (1.3 $mm.s^{-1}$). 62
Figure 4.31. Comparison of experimental and numerical deformation of R75t1 core structure against blunt tipped indenter (1.3 $mm.s^{-1}$). 62
Figure 4.32. Comparison of experimental and numerical force-displacement curves of R75t1 core structure against conical tipped indenter (1.3 $mm.s^{-1}$). 63
Figure 4.33. Comparison of experimental and numerical force-displacement curves of R75t1 core structure against hemispherical tipped indenter (1.3 $mm.s^{-1}$). 64

Figure 4.34. Comparison of experimental and numerical deformation of R75t1 core structure against hemispherical tipped indenter (1.3 $mm.s^{-1}$). 64
Figure 4.35. Comparison of experimental and numerical force-displacement curves of R75t05 core structure against blunt tipped indenter (0.13 $mm.s^{-1}$). 65
Figure 4.36. Comparison of experimental and numerical deformation of R75t05 core structure against blunt tipped indenter (1.3 $mm.s^{-1}$). 65
Figure 4.37. Comparison of experimental and numerical force-displacement curves of R75t05 core structure against conical tipped indenter (0.13 $mm.s^{-1}$).... 66
Figure 4.38. Comparison of experimental and numerical force-displacement curves of R75t05 core structure against hemispherical tipped indenter (1.3 $mm.s^{-1}$)..... 67
Figure 4.39. Comparison of experimental and numerical deformation of R75t05 core structure against hemispherical tipped indenter (1.3 $mm.s^{-1}$). 67
Figure 4.40. Comparison of experimental and numerical force-displacement curves of R75t1 core structure against blunt tipped indenter (3.5 $m.s^{-1}$). 68
Figure 4.41. Thickness distribution of R75t1 core units in initial (on the left) and final stages of deformation. 69
Figure 4.42. Effect of strain rate and inertia on behavior of R75t1 core units. 711
Figure 4.43. Effect of strain rate and inertia on behavior of R75t05 core units. 72
Figure 5.1. Specimens before and after heat treatment operation. 74
Figure 5.2. Comparison of test results of heat treated R75t1 structure against blunt tipped indenter. 75
Figure 5.3. Comparison of test results of heat treated R75t1 structure against conical tipped indenter. 75
Figure 5.4. Comparison of test results of heat treated R75t1 structure against hemisphere tipped indenter. 76
Figure 5.5. Comparison of test results of heat treated R75t05 structure against blunt tipped indenter. 77
Figure 5.6. Comparison of test results of heat treated R75t05 structure against conical tipped indenter. 77
Figure 5.7. Comparison of test results of heat treated R75t05 structure against hemisphere tipped indenter. 78

Figure 5.8. Comparison of experimental and numerical force-displacement curves of heat treated R75t05 core structure against blunt tipped indenter (1.3 mm.s^{-1})..... 81
Figure 5.9. Comparison of experimental and numerical force-displacement curves of heat treated R75t1 core structure against hemispherical tipped indenter (0.13 mm.s^{-1})..... 81
Figure 6.1. Specimen fixture used in experimental study and actual image captured before tests. 82
Figure 6.2. Comparison of test results and deformed specimens with confined and unconfined states (R75t1 core units against blunt tipped indenter). 83
Figure 6.3. Comparison of test results and deformed specimens with confined and unconfined states (R75t1 core units against conical tipped indenter). 84
Figure 6.4. Comparison of test results and deformed specimens with confined and unconfined states (R75t1 core units against hemisphere tipped indenter)... 85
Figure 6.5. Comparison of test results and deformed specimens with confined and unconfined states (heat treated R75t1 core units against blunt tipped indenter). 86
Figure 6.6. Comparison of test results and deformed specimens with confined and unconfined states (heat treated R75t1 core units against conical tipped indenter). 87
Figure 6.7. Comparison of test results and deformed specimens with confined and unconfined states (heat treated R75t1 core units against hemispherical tipped indenter). 88
Figure 6.8. Comparison of test results and deformed specimens with confined and unconfined states (R75t05 core units against blunt tipped indenter)..... 89
Figure 6.9. Comparison of test results and deformed specimens with confined and unconfined states (R75t05 core units against conical tipped indenter) 90
Figure 6.10. Comparison of test results and deformed specimens with confined and unconfined states (R75t05 core units against hemisphere tipped indenter). 91
Figure 6.11. Comparison of test results and deformed specimens with confined and unconfined states (heat treated R75t05 core units against blunt tipped indenter). 92

Figure 6.12. Comparison of test results and deformed specimens with confined and unconfined states (heat treated R75t05 core units against conical tipped indenter). 93
Figure 6.13. Comparison of test results and deformed specimens with confined and unconfined states (heat treated R75t05 core units against hemisphere tipped indenter). 94
Figure 7.1. Sandwich structures with (a) as-received, (b) heat treated core units. 96
Figure 7.2. Ballistic test chamber of IZTECH. 97
Figure 7.3. Change of impact velocity with chamber pressure. 97
Figure 7.4. Photographs of sandwich structure with R75t1 core units; (a) impacted core structure, (b) backing plate (impact velocity: 141.44 $m.s^{-1}$). 98
Figure 7.5. Photographs of sandwich structure with R75t1 core units; (a) impacted core structure, (b) backing plate (impact velocity: 179.69 $m.s^{-1}$). 99
Figure 7.6. Photographs of sandwich structure with R75t05 core units; (a) impacted core structure, (b) backing plate (impact velocity: 155.82 $m.s^{-1}$). 100
Figure 7.7. Photographs of sandwich structure with R75t05 core units; (a) impacted core structure, (b) backing plate (impact velocity: 178.65 $m.s^{-1}$). 100
Figure 7.8. Photographs of sandwich structure with R75t1HT core units; (a) impacted core structure, (b) backing plate (impact velocity: 142.94 $m.s^{-1}$). 101
Figure 7.9. Photographs of sandwich structure with R75t1HT core units; (a) impacted core structure, (b) backing plate (impact velocity: 181.63 $m.s^{-1}$). 102
Figure 7.10. Photographs of sandwich structure with R75t05HT core units; (a) impacted core structure, (b) backing plate (impact velocity: 140.30 $m.s^{-1}$). 103
Figure 7.11. Photographs of sandwich structure with R75t05HT core units; (a) impacted core structure, (b) backing plate (impact velocity: 176.41 $m.s^{-1}$). 103

LIST OF TABLES

Table **Page**

Table 2.1. Results obtained from experimental and numerical studies 10

Table 2.2. Results obtained from experimental and numerical studies 19

Table 2.3. Ballistic limit of projectiles used in experimental study 21

Table 2.4. Configuration of layers used in experimental study 23

Table 3.1. Chemical composition of AISI 304L stainless steel 27

Table 3.2. Geometrical parameters of core geometries. 29

Table 4.1. Material properties of SHTB test setup. 36

Table 4.2. Parameters of Johnson-Cook material model used in numerical studies of AISI 304L stainless steel 42

Table 4.3. Experimental and numerical results. 70

Table 5.1. Comparison of performance evaluation tests' results of as-received and heat treated core structures. 79

Table 8.1. AEF values of core units against test velocity of 0.13 $mm.s^{-1}$. 107

CHAPTER 1

INTRODUCTION

1.1. Introduction

In recent years, modern warfare has evolved into a new shape which occurs on various types of battlefields varying from rural areas to downtowns of cities with a common name; terrorism. During last decades, attacks of terrorist organizations had become extremely lethal with improved ambush tactics since these attacks catch national armed forces completely off guard and inflict heavy casualties. Ambush attacks are mainly formed during passage of lightly armored personnel carriers or infantry by remotely triggering land mines or improvised explosive devices (IEDs). Some examples of IEDs caught unexploded given in Figure 1.1.

(a) (b)

Figure 1.1. Some examples of IEDs made from (a) plastic bottles filled with explosives (Source: www.nato.int), (b) artillery shells (Source: www.rfsystemlab.us).

Explosions of these bombs create two main threats; target structure is first hit by blast wave which globally damages the whole structure and then blast propelled fragments or shrapnels damage the surroundings which causes more localized damage and penetration of projectiles into the armor. A properly engineered armor should resist both of these threats and totally eliminate or minimalize the number of casualties. It is also important to have such system to be manufactured with domestic capabilities as it

will expand our country's inventory on fighting against terrorism and reduce the need of other countries or companies' technology on national defense.

1.2. Aim of the Study

Although otherwise is highly desired, it is evident from recent situation that Turkey's fight against terrorism is not going to end in near future due to our country's geographical position and political condition of neighboring countries. In order to cover our country's needs in military defense industry, it is required to develop an armor structure which resistant against blast wave and penetration of blast propelled projectiles. The developed structure must also be manufactured with relatively cheap materials and low engineering knowledge which further allows it to be manufactured easily countrywide. In this study, a novel structure which has proven itself against blast wave damage is investigated under penetration of different projectile geometries, aiming to be an alternative as a core structure in a sandwich armor system which can be manufactured with domestic capabilities and engineering knowledge.

1.3. Scope of the Study

This thesis summarizes the experimental and numerical work that includes the performance evaluation of core structure against different projectile geometries as well as changes of physical conditions such as conducting heat treatment on core structure and/or radially confining the core geometry with other core units to observe if these have an effect on penetration behavior. Following chapter on literature summarizes the studies that have been investigating the penetration of shell and sandwich structures with their own aspects. Manufacturing of core units and other components of sandwich structure along with special testing equipment was detailed in Chapter 3. Steel that was used in manufacturing of core units was mechanically characterized in Chapter 4, followed by performance evaluation tests of core units against different projectiles. Effect of heat treatment on penetration behavior was presented in Chapter 5 while details and results of confinement effect was given in Chapter 6. A case study was presented in Chapter 7 which investigates the penetration behavior of structure against

ballistic tests and Chapter 8 concludes the experimental and numerical results that were obtained during the whole study.

CHAPTER 2

LITERATURE SURVEY

Starting from mid of 19th and through the 20th century, war industry of mankind has evolved into a new form where open field infantry battles has exchanged with combat of heavily armored vehicles where protection of various threats and mobility with light weight is expected. In order to ensure these requirements, various types of armor systems made of different constituents were proposed. As the investigated structure in this thesis is a shell core unit of a sandwich armor, following subsections give an insight to deformation of spherical shell structures and studies on sandwich armor structures with various core geometries and/or materials.

2.1. Indentation & Penetration of Shell Structures

Limited number of studies was presented on indentation and penetration behavior of hemispherical structures as previous authors mostly focused on compression of shell structures rather than indentation. Nasto et. al conducted a study on localization of deformation of thin shells under indentation both experimentally and numerically (Nasto, Ajdari, Lazarus, Vaziri, & Reis, 2013). In this paper, polymeric hemispherical shells were produced by shell molding and differently sized indenters were manufactured investigate the ratio of the radii of the indenter to hemispherical shells, termed as Γ. Range of Γ was set between the values of 0 and ∞ which represent the transition between point load to plate load, presented in Figure 2.1. Experimental study was conducted on quasi-static regime and progressive damage of s-cone formation in shell structure was observed. Increasing the value of Γ has led into increase in number of s-cones for sharp indenters (Γ <1) while total number of 5 s-cones were formed when structure is subjected to plate loading. For blunt indenters (Γ >2), number of s-cones were further increased when Γ is decreased towards 2. It was also noted that nature of the contact between indenter and shell affects the behavior under axial loading. Conducted numerical study was also reported to be matching very well with experiments in terms of behavior and damage progress.

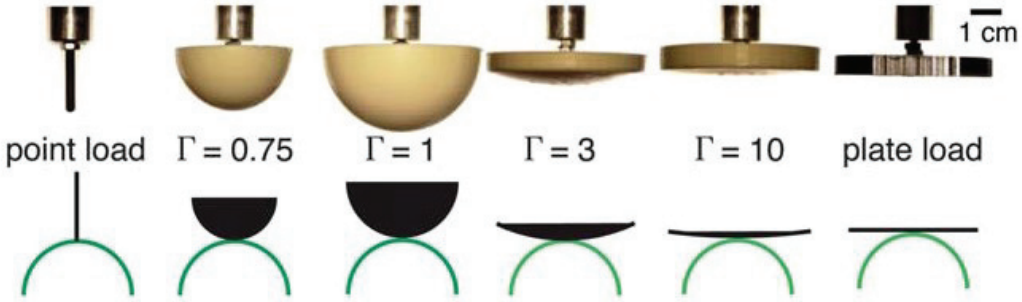

Figure 2.1. Schematic of indenters ranging from point to plate load (Source: Nasto et al., 2013).

Another study was conducted by Nasto and Reis on localized damage of indented hemispherical shell and case study investigated in previous work was further studied numerically (Nasto & Reis, 2014). In this article, material model used in FE models were changed from Neo-Hookian hyper elastic to linear elastic to observe its effects on numerical results. In addition, effect of the self-weight, radius and thickness of the shell was also investigated. Results showed that deformation behavior mainly depends on ratio of thickness to shell radius and it was noted that number of s-cones tends to increase with increasing indentation on thin shells. Aforementioned increase in s-cones was also observed, for shells with intermediate thickness, to a total number of three to four. Beyond the thickness to radius ratio of 0.06, localization of damage was observed to be suppressed and deformation was observed to be axisymmetric. Self-weight and material model were found to be ineffective in behavior of structure. Change in deformation behavior with increase in thickness to radius ratio is given in Figure 2.2.

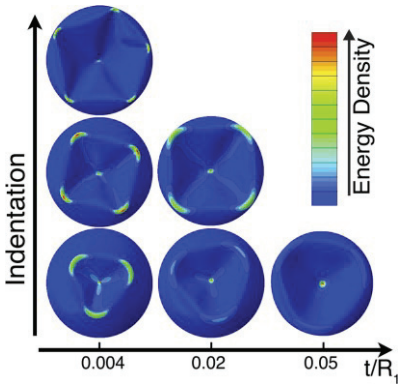

Figure 2.2. Change in deformation with increase in ratio of thickness to radius (Source: Nasto & Reis, 2014).

Studies on hemispherical capped structures with larger dimensions are also available on literature. Lupker investigated the critical impact velocity of LPG tank

during an impact from train part (Lupker, 1990). It was reported that during the crash of a LPG tank, impact energy is absorbed by deformation of hemispherical part of the body and under frame. In order to further investigate this behavior, study included tests on scaled models as well as numerical models and analytical investigations. Finite element models used BOSOR5 software with Kirchoff-Love assumptions with J2-deformation and J2-flow theories while analytical calculations were based on (A. J. M. C. R. Calladine, 1969). Results show that, experiments conducted as central loading indicated unsymmetric buckling with multiple lobes ranging between 3 to 5, as presented in Figure 2.3. Both numerical and analytical models were able to represent the force-deflection behavior and were presented in Figure 2.4.

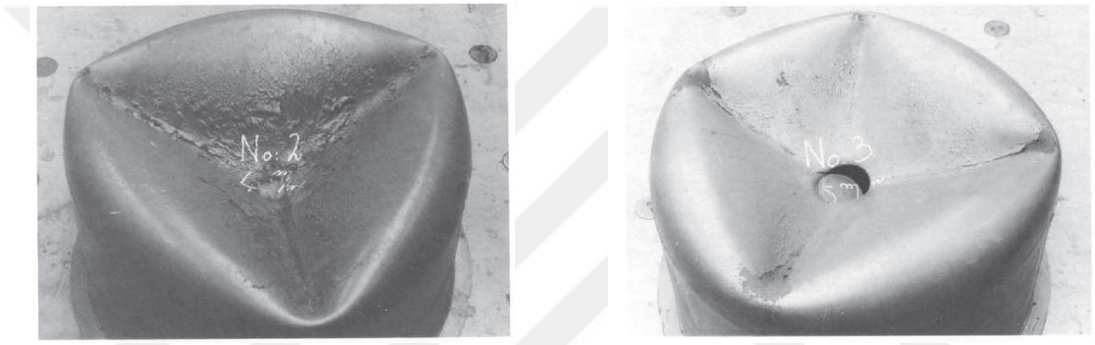

Figure 2.3. Unsymmetrical buckling observed in experimental study (Source: Lupker, 1990).

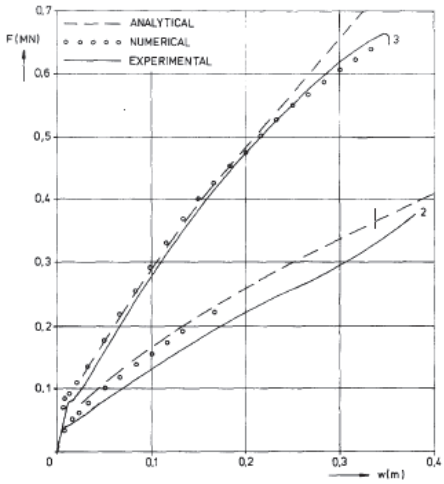

Figure 2.4. Unsymmetrical buckling observed in experimental study (Source: Lupker, 1990).

One of the milestone works conducted on spherical shell deformation was done by De Oliveira and Wierzbicki (De Oliveira & Wierzbicki, 1982). In this study, spherical shell structures which were deformed under point load, rigid compression

plates and externally applied pressure were analytically investigated. Authors were focused to propose equations on crushing behavior with respect to width of compressing plate, deflection, shell thickness and outer radius of target geometry which was validated by previous studies and/or actual results. All of the proposed analytical solutions indicated a good correlation and comparative results of loading under rigid boss and compressive plate were presented in Figure 2.5 and 6, respectively.

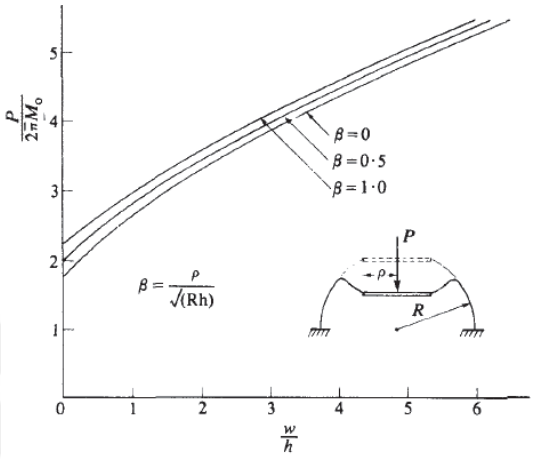

Figure 2.5. Analytical calculation of deformation under rigid body (Source: De Oliveira & Wierzbicki, 1982).

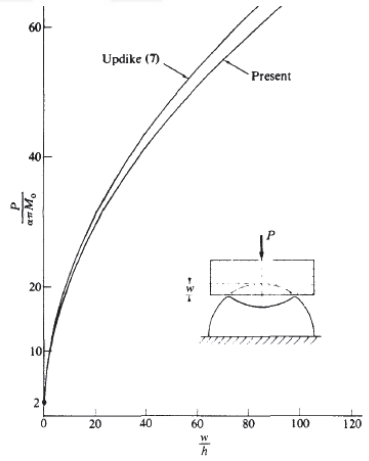

Figure 2.6. Analytical calculation of deformation under compressive plate (Source: De Oliveira & Wierzbicki, 1982).

Amiri and Rasheed conducted an analytical, experimental and numerical study on hemispherical shells which were subjected to concentrated load at the center of hemispherical region (Amiri & Rasheed, 2012). In this study, hemispherical shells made from stainless steels and bronze with radii of 50 and 75 mm, respectively were subjected to point loading at their apex. Three different indenters with boss sizes of

1.25, 2.5 and 5 mm were selected for experimental study and hemispherical shells were confined at their fixture contacting edge with a groove to allow deflection only in single axis. Tests on stainless steel showed axisymmetric deformation followed by bifurcation at later stages and bronze indicated a similar behavior under loading with experimental results presented in Figure 2.7. Effect of indenting boss's thickness is found to increase the initial collapse load and size of the dimpling noted during experimental study. Analytical studies were able to offer a prediction of outer diameter to shell thickness ratio around 100 while numerical model can duplicate the experimental behavior well. Dimensionless initial collapse load versus boss size graphs were presented in Figure 2.8 and a fair correlation is present with minor differences which was related with plastic deformation induced in manufacturing method.

Figure 2.7. Progress of deformation on steel and bronze shells
(Source: Amiri & Rasheed, 2012).

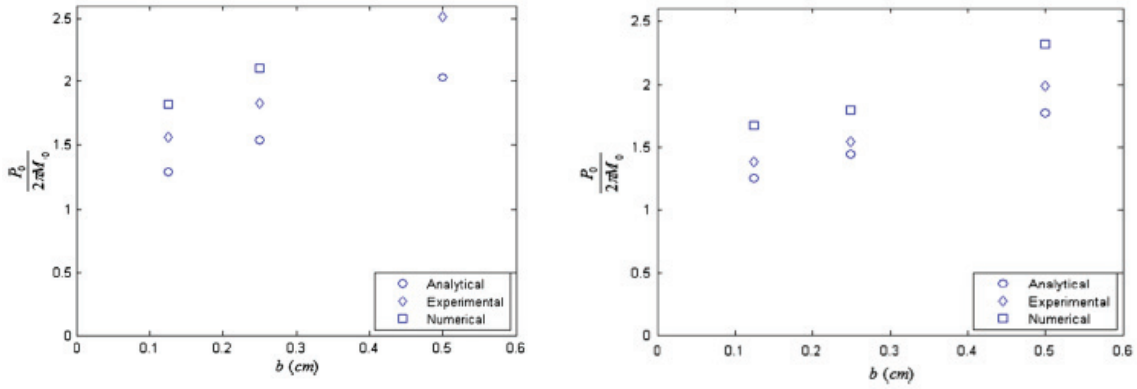

Figure 2.8. Comparison of initial collapse loads for different boss sizes from experimental, numerical and analytical results for investigated materials, bronze on the right (Source: Amiri & Rasheed, 2012).

Shariati and Allahbakhsh investigated the deformation behavior of thin shells made from mild steel alloy when subjected to axial loading from different geometries (Shariati & Allahbakhsh, 2010). Geometrical variations of the components that applied to load includes a rigid plate, rigid indenters with different cross sections such as circle, square and sphere as well as rigid tube. Numerical study was also conducted using ABAQUS commercially available finite element software and results were compared with experimental ones in terms of load-deformation curves and deformation shapes. Study concluded that energy absorption capability of the shells increases linearly with thickness increase and load-displacement curves indicate a quadratic curve. Also, deformation was observed in the form of stationary or rolling plastic hinges and results indicated rolling plastic hinges increase when the thickness of shell and its outer diameter increase. Numerical study also yielded good correlation with experimental results and comparison of both were presented in Figure 2.9.

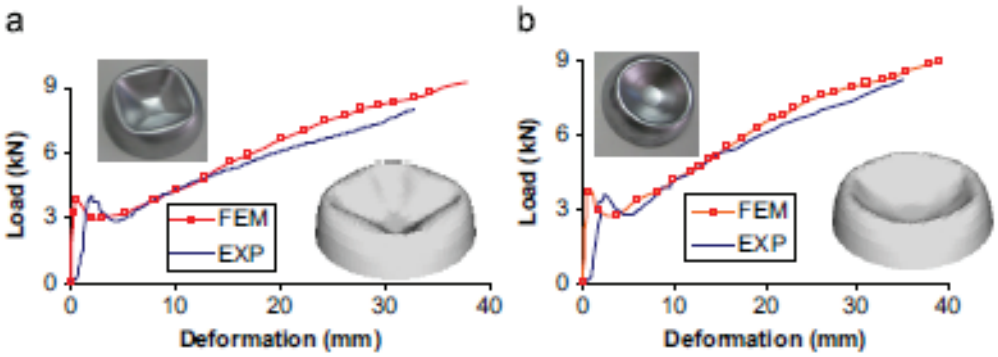

Figure 2.9. Comparison of experimental and numerical results against loading from square bar and circular bar (Source: Shariati & Allahbakhsh, 2010).

Studies on crushing behavior of spheres, conical frustum, and tubes are likely to be found on literature but penetration and/or crushing of combined geometry shells are found to be rarely studied. Gupta et al. investigated the crushing behavior of combined geometry shells under axial impact conditions (Gupta, Mohamed Sheriff, & Velmurugan, 2008a). In this study, combined geometry of aluminum thin shells and shallow hemispherical cap were subjected to crushing loads at quasi-static and impact regimes. Ratio of cap radius to thickness (R/t) of investigated structure varied between 27 and 180 while ratio of mean diameter to thickness (D_m/t) of conical portion of structure changed between 79 and 190. Conducted numerical studies on LS-DYNA were also validated by experiments and results were given in Table 2.1. They reported progressive collapse of specimens beginning with the initial flattening, axisymmetric inward dimpling and/or non-symmetric lobe formation which was followed by the collapse of the conical portion. It was also concluded that numerical results match fairly well with experiments in terms of damage modes and load-compression curves.

Table 2.1. Results obtained from experimental and numerical studies (Source: Gupta, Mohamed Sheriff, et al., 2008a).

Specimen	Thickness	Velocity	Compression (mm)		Mean Load (kN)	
			Exp.	Num.	Exp.	Num.
S1	1.6	8	28.18	30.0	7.92	8.76
S2	0.7	2	25.0	24.76	2.2	2.31
S3	1.2	4	28.90	30.0	8.12	8.93
S4	0.7	2	25.0	26.0	2.15	2.12
S5	0.7	2	25.0	27.0	2.22	2.12
S6	0.7	2	60.0	57.30	0.89	0.97
S6	0.9	6	73.80	75.0	6.22	6.52
S6	1.2	4	41.20	43.0	7.98	8.22
S6	1.6	8	77.40	80.20	11.82	11.97
S7	1.6	8	26.70	28.0	20.94	22.21
S8	1.6	10	95.35	101.20	15.28	17.09
S9	0.9	2	75.0	76.0	4.28	4.42
S10	0.7	2	89.0	91.0	2.52	2.54

Another study was conducted by Gupta et al. on buckling of thin spherical shells under axial load (Gupta, Mohamed Sheriff, & Velmurugan, 2008b). Specimens with the geometries of hemispherical and shallow shells were subjected to axial crushing loads which resulted in different modes of damage due to change in geometry; specimens with R/t values less than 38.13 were reported to deform rolling plastic hinge and inward dimple while specimens with R/t values ranging between 40 and 218 tend to fail with multiple lobe formation. An analytical and numerical study was also conducted and it was concluded that results of both studies match well with experiments. Comparison of experimental and analytical study is given in Figure 2.10.

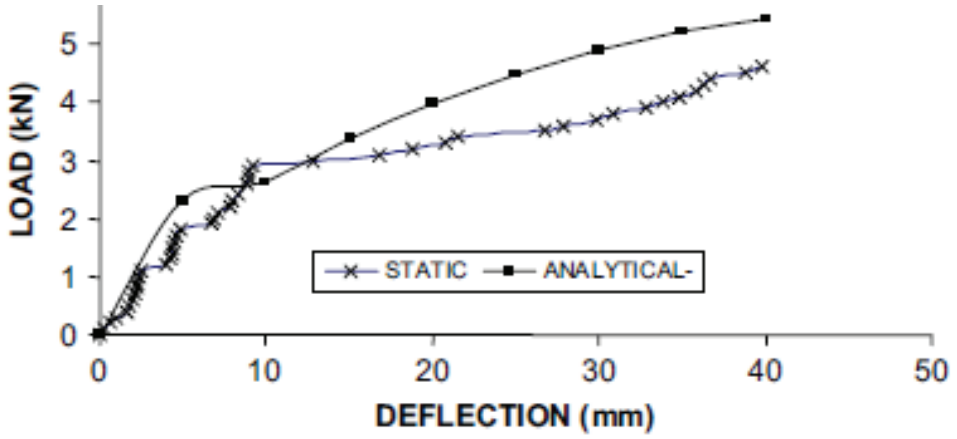

Figure 2.10. Comparison of analytical and experimental study
(Source: Gupta, Mohamed Sheriff, et al., 2008b).

Gupta and Venkatesh studied dynamic axial compression of thin walled spherical shells experimentally and numerically (Gupta & Venkatesh, 2004). Authors dealt with dynamic testing of spherical shells with R/t ratio between 13 and 85. Experimental study was completed using gravity drop hammer tests with an impact mass of 34.75 kg and impact velocity ranging between 2-9 $m.s^{-1}$. In addition to impact tests, static crushing tests were also performed on ZWICK machine with a capacity of 25 T at the cross-head speed of $10mm.min^{-1}$. Forge2 software was occupied for numerical studies and specimens were assumed as rigid-viscoplastic with Von Misses yield criteria. Study concluded that low values of R/t and thickness greater than 1.5 mm deformed with formation of rolling plastic hinge and inward dimple. However, when the thickness is equal to or less than 1.5 mm, an integral number of lobes tend to form at a certain stage of compression. It was also concluded that numerical study corresponds well with experiments in terms of damage formation and load-deformation curves.

Comparison of damage of experimental and numerical study was given with load-deformation curves in Figure 2.11a and 11b, respectively.

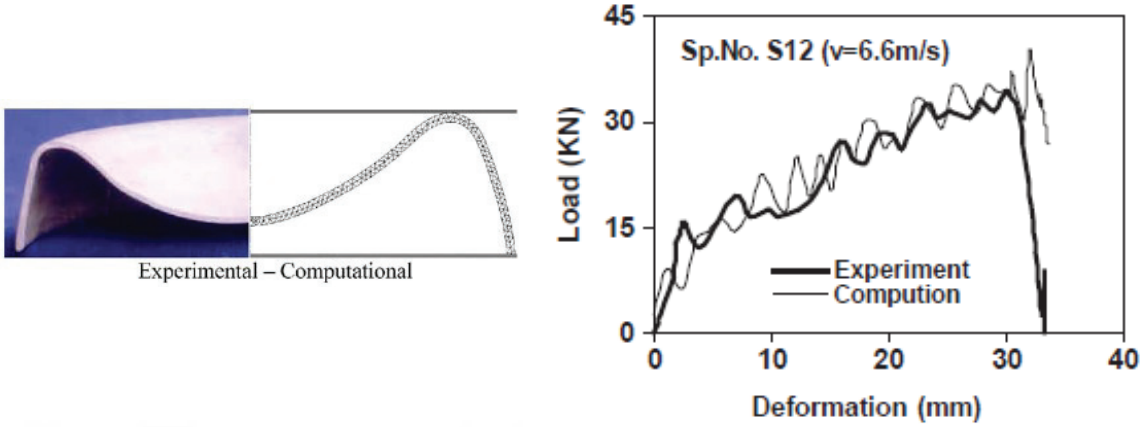

(a) (b)

Figure 2.11. Comparison of experimental and numerical results
(Source: Gupta & Venkatesh, 2004).

Beside forms of spheres, various studies have been presented on different shell geometries to investigate their energy absorption capability. Tabiei and Nilankantan investigated energy absorption capability of tubes under axial crushing due to mine blast, targeting to reduce the injuries caused by mine blast (Tabiei & Nilakantan, 2009). In this study, shell tubes in cylindrical form were offered as energy absorbing structures in seats of infantry vehicles and comparative study has been undertaken as analytical, numerical and experimental forms. An analytical formulation is proposed by study to predict the form of kinetic energy and energy dissipated in plastic deformation occurring during axial crushing force of a previous work. Comparative results indicated that numerical and analytical solutions were in very good agreement and results were proposed in Figure 2.12a. Second comparison was done with actual data to observe the capability of analytical formulation in an event of free falling and results were presented in Figure 2.12b with respect to acceleration in G scale. Analytical calculations indicated good correlation with experimental and numerical results with negligible overshooting of acceleration.

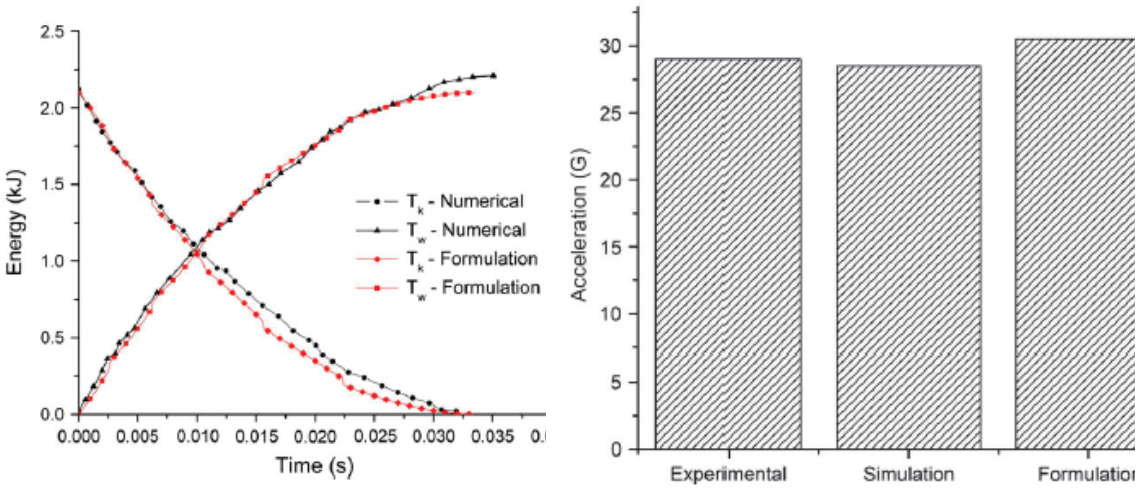

(a) (b)

Figure 2.12. Comparison of numerical (a) and experimental (b) results with analytical calculations (Source: Tabiei & Nilakantan, 2009).

Taşdemirci investigated the effect of tube end constraining on the axial crushing behavior of an aluminum tube experimentally and numerically (Alper Tasdemirci, 2008). Through the experimental portion of the study, deep drawn 3003-H14 aluminum tubes were subjected to axial compression at a cross-head speed of 100 $mm.min^{-1}$. During experiments, constraining of single or both ends of specimens with various combinations of specimen holder was investigated to observe if there is any constraint-related behavior. Experimental process was also modeled in LS-DYNA and mass scaling was occupied by scaling up the masses of finite element model with a factor of 1000. Study concluded that free and single-end constraint tubes deformed in concertina mode both experimentally and numerically. Mixed/diamond mode of deformation was observed in experimental and numerical study of tubes with fully-inward constraint while concertina/mixed mode of deformation was noted for double-end fully and inward-outward tubes. Numerical study also agreed well with experiments in terms of load-displacement curves and comparison of experimental and numerical damage progress is given in Figure 2.13.

Aktay, Toksoy and Güden experimentally and numerically investigated axial crushing of extruded polystyrene foam-filled thin-walled aluminum tubes (Aktay, Toksoy, & Güden, 2006).

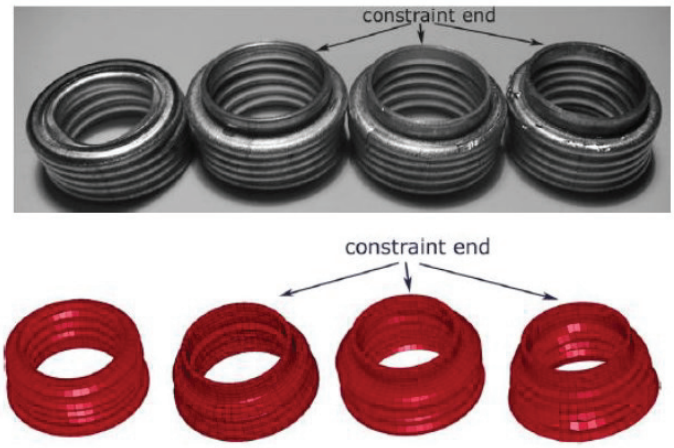

Figure 2.13. Comparison of experimental and numerical damage
(Source: Alper Tasdemirci, 2008).

In this study, cold deep drawn aluminum tubes with common outer diameter of 16 and 25 mm were filled with extruded polystyrene foam (XPS) with 2 different densities. As received and foam filled tubes were then subjected to quasi-static compression with a deformation rate of 100 $mm.min^{-1}$. Numerical models of aforementioned study were created with ANSYS and solved using finite element code PAM-CRASH. Eight node solid elements were used in modeling of XPS foam and test plates while Belytschko-Tsay shell elements were occupied for modeling of aluminum tubes. Authors concluded that, along with absorbed energy, number of folds on aluminum tubes tend to increase with foam filling and foam density. In addition, numerical results showed good correlation with experiments in terms of both load-displacement curves and comparison of them were given in Figure 2.14.

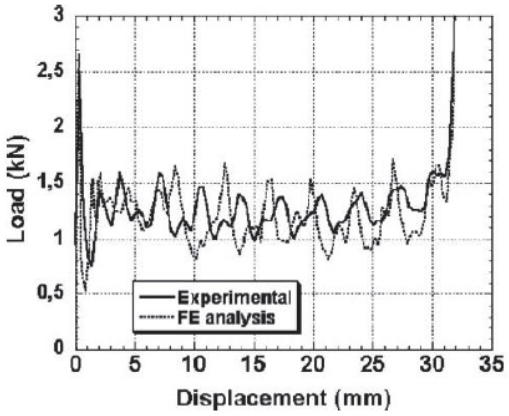

Figure 2.14. Comparison of experimental and numerical load-displacement curves
(Source: Aktay et al., 2006).

2.2. Penetration of Sandwich Structures with Various Core Materials

In military history, first examples of armor structures were proposed as monolithic geometries which provided safety against different threads by increasing thickness of the structure. This resulted in a number of disadvantages on mobile units as the increased weight causes reduced mobility on different terrain conditions and extra weight brings in increased fuel consumption which means economical and logistics handicap. As an alternative, multi-layered and sandwich structures were studied proposed with their high energy absorption rates and low weight when compared with monolithic armors.

Previous studies on penetration and perforation behavior had shown that core material and its geometry have a pronounced effect on performance of sandwich structures. Along with variations in core material (Jover, Shafiq, & Vaidya, 2014; A. Tasdemirci, Tunusoglu, & Güden, 2012; Zeng, Pattofatto, Zhao, Girard, & Fascio, 2010; Zhao, Elnasri, & Girard, 2007), numerous studies on penetration and perforation behavior of sandwich structures with different structural elements have been conducted. Studied sandwich structures included variations of face and backing plates (Kolopp, Rivallant, & Bouvet, 2013; Yang et al., 2015) and layering combinations (Deng, Zhang, & Cao, 2013; Ramadhan, Abu Talib, Mohd Rafie, & Zahari, 2013; Wang et al., 2013; Wei, Yunfei, Sheng, & Gang, 2012).

Kolopp et al. investigated the behavior of sandwich structures with different face plates against medium velocity impact (Kolopp et al., 2013). In this study, aluminum or dry fabric Aramid was used as front skin while core geometry was selected as honeycomb made of aluminum or Nomex. Single staged gas gun with impact velocities around 120 $m.s^{-1}$ was occupied for experimental study and a hardened steel projectile with a diameter of 30 mm was used during tests. Authors concluded that, along with reduced weight, sandwich structures with dry fabric front face showed better perforation characteristics when compared to aluminum sandwich structures or plates. In addition, dry fabrics indicated better performance against sandwiches with resin impregnated front face since local failure due to resin presence was observed through the experiments. Tested sandwich structure with dry face sheet and Nomex core is given in Figure 2.15.

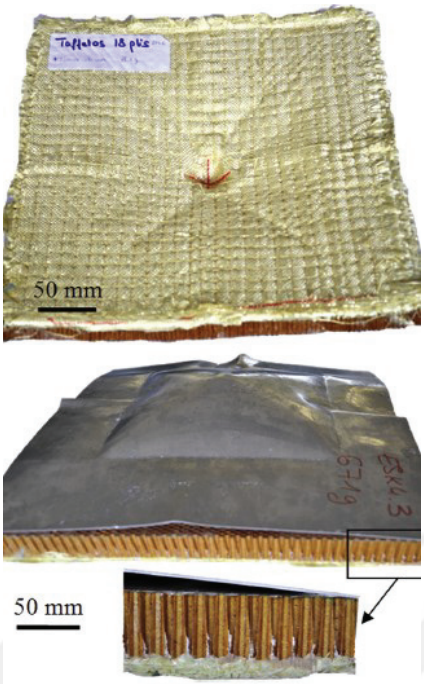

Figure 2.15. Tested sandwich structure
(Source: Kolopp et al., 2013).

Previously, numerous authors presented articles on impact and penetration behavior of various structures. These studies included penetration behavior of metals, composites and sandwich structures against various types of indenter geometries such as flat, conical, ogival and hemispherical tipped indenters at impact velocities ranging between 35 to 800 $m.s^{-1}$ (Børvik, Hopperstad, Langseth, & Malo, 2003; Børvik, Langseth, Hopperstad, & Malo, 1999, 2002; Børvik, Leinum, Solberg, Hopperstad, & Langseth, 2001; Chen, Yang, Lu, & Chen, 2008; Dey, Børvik, Teng, Wierzbicki, & Hopperstad, 2007; Forrestal, Luk, & Brar, 1990; Gupta, Iqbal, & Sekhon, 2006, 2008; Hou, Zhu, Lu, & Fang, 2010; Jordan & Naito, 2014; Kpenyigba, Jankowiak, Rusinek, Pesci, & Wang, 2015; Y.-W. Lee, Woertz, & Wierzbicki, 2004; Lundberg, Renström, & Lundberg, 2006; Manes, Serpellini, Pagani, Saponara, & Giglio, 2014; Mines, Roach, & Jones, 1999; Mohagheghian, McShane, & Stronge, 2015; Mohan & Velu, 2014; Nesterenko, Goldsmith, Indrakanti, & Gu, 2003; Rosenberg & Dekel, 2009; Tan & Khoo, 2005; Teng, Wierzbicki, & Huang, 2008; Warren & Forrestal, 1998; Warren & Tabbara, 2000; Wen, 2000). These studies indicated some of the critical damage mechanisms on penetration phenomena of single or multi-layered structures.

Kpenyigba et. al investigated the effect of projectile shape on steel sheets. Projectile geometries of conical, hemisphere and their combinations as double-nose were impacted to steel sheets with velocities ranging between 35-180 $m.s^{-1}$ (Kpenyigba et al., 2015). Projectiles used in this study had a weight of 13 g and indenter diameter to span of plate was kept constant to 3.85. Experimental study included characterization of steel plates as well as impact tests on gas gun and process was numerically modeled. After experimental and numerical work, study concluded that ballistic limit, energy absorption capability and damage mode were dependent on projectile geometry. Dominant damage mode was observed to be petaling for conical tipped projectiles while plugging was observed on experimental and numerical studies of hemisphere tipped projectiles. Experimental and numerical studies indicated good correlation in terms of residual velocity levels and damage formation. Comparison of experimental and numerical damage is given in Figure 2.16.

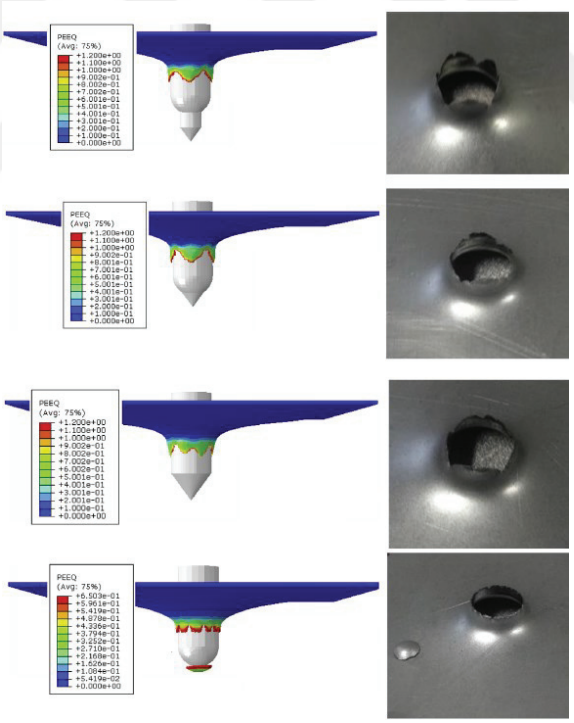

Figure 2.16. Comparison of experimental and numerical deformation (Source: Kpenyigba et al., 2015).

Hou et. al studied the impact behavior of metallic sandwich structures with aluminum foam core (Hou et al., 2010). CYMAT^{TM} closed cell aluminum foam core structure was bonded to face sheets of Al-5005H34 in four different thicknesses by

using epoxy adhesive and then subjected to quasi-static indentation or projectile impact tests. Tests at lower strain rates were conducted on conventional MTS testing equipment at a cross head velocity of 2.10^{-2} $m.s^{-1}$ while impact test were conducted on gas gun against conical, flat and hemispherical tipped projectiles at impact velocities ranging from 100 $m.s^{-1}$ to 246 $m.s^{-1}$. Experimental study showed that increasing the thickness of face sheets and density of core structure resulted in observation of higher ballistic limit velocity and increase in deformation area along with absorbed energy. It was also noted that changing the strain rate regime from quasi-static to dynamic indicated change of damage on back plate and increase in absorbed energy. Damaged back plates and levels of dissipated energy were compared in Figure 2.17.

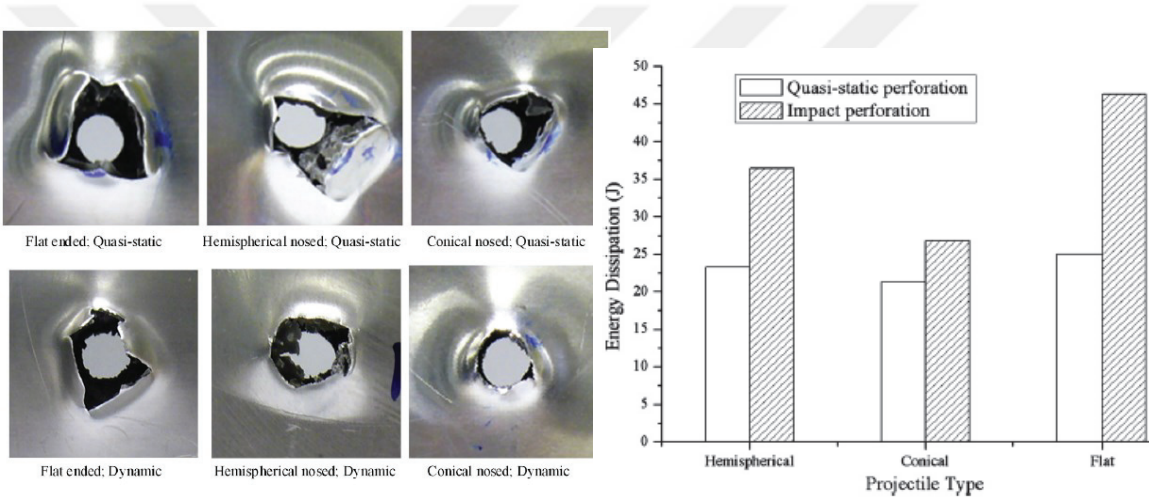

Figure 2.17. Effect of strain rate on (a) Damage modes, (b) Energy Dissipation levels (Source: Hou et al., 2010).

Gupta et. al experimentally and numerically investigated the behavior of thin 1100-H12 aluminum plates subjected to impact by hollow projectiles (Gupta et al., 2006). In this study, plates of 1 mm thickness were impacted by hollow hemispherical and blunt nosed projectiles at various impact velocities to observe the change of damage formation, impact velocities and residual velocities. Single staged gas gun was occupied for impact tests and projectiles which were made of EN-24 stainless steel with a common diameter of 19 mm were used. Measured values of impact velocity (V_i), residual velocity (V_r) , absorbed energy (E_{abs}) and maximum deformation of target (D_{max}) is tabulated on Table 2.2.

Table 2.2. Results obtained from experimental and numerical studies (Source: Gupta et al., 2006).

Test	V_i (m.s^{-1})	V_r (m.s^{-1})	E_{abs} (J)	D_{max} (mm)
Blunt-1	115.6	92.9	124.2	8.9
Blunt-2	104.0	80.2	115.0	8.9
Blunt-3	102.5	79.2	111.1	10.1
Blunt-4	92.5	67.5	105.0	11.0
Blunt-5	87.5	58.3	111.7	11.4
Blunt-6	73.9	43.8	93.0	11.8
Hemisphere-1	114.7	92.3	109.0	12.2
Hemisphere-2	109.7	86.8	105.7	13.3
Hemisphere-3	106.1	80.1	113.7	14.1
Hemisphere-4	105.5	79.0	114.8	14.3
Hemisphere-5	98.3	71.0	108.6	15.1
Hemisphere-6	92.3	63.5	105.4	15.8

Numerical study was also conducted on impact of thin aluminum plates and ABAQUS finite element modeling software was used. Behavior of aluminum was modeled using Johnson-Cook material model whose parameters were found by tension tests. It was concluded from impact experiments that blunt-nosed projectiles caused the formation of plug which has the same diameter with indenter whereas relatively greater bending was observed on tests of hemispherical-nosed projectile which further result in local thinning. Plug formation was also observed in impact tests of hemispherical-nosed projectile but its diameter was found to be relatively smaller due to aforementioned damage mechanism. Relatively higher ballistic limit velocity was noted for hemispherical-nosed projectile. Numerical study indicated that Johnson-Cook material model is capable of modeling penetration problem and experimental results match fairly well with experiments in terms of residual velocities and deformation profiles. Comparison of experimental and numerical results was given in Figure 2.18.

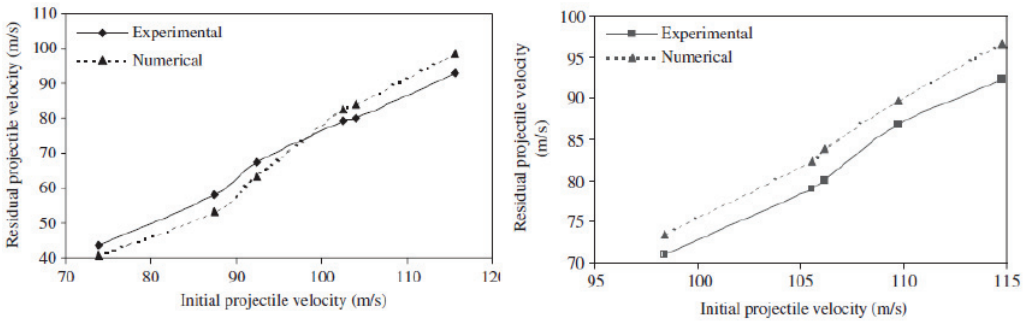

(a)

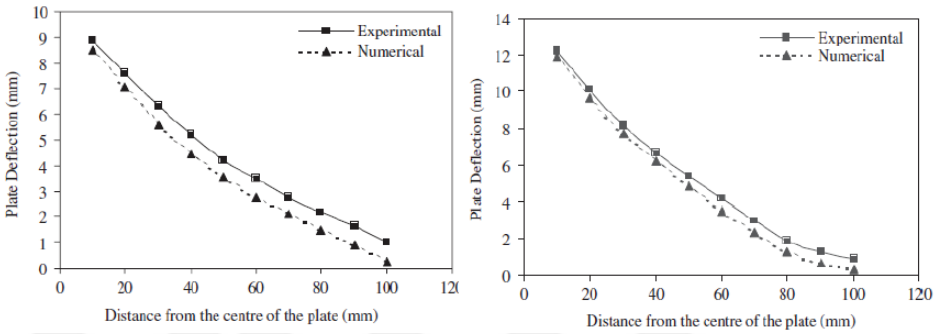

(b)

Figure 2.18. Comparison of experimental and numerical results in terms of (a) residual velocities (b) deformation profile (on the left, blunt-nosed projectile; on the right, hemispherical-nosed projectile) (Source: Gupta et al., 2006).

Behavior of sandwich structures under impact loading was also widely investigated. Jordan and Naito studied the effect of nose shape on fragments penetrating Glass Fiber Reinforced Plastic (GFRP) (Jordan & Naito, 2014). E-Glass/Phenolic glass reinforced plastic plates with thicknesses of 4, 9 and 14 mm were subjected to impact of chisel, 30 CAL fragment simulated projectile (FSP), 120 degree conical, right circular cylinder, hemispherical, parallelepiped and cube projectiles. All of the projectiles used in this study was propelled from powder gun. Ballistic limit of each projectile type was determined with respect to MIL-STD-662F using four shot ballistic limit. In addition, four additional shots were made with intervals of 50 $m.s^{-1}$ above ballistic limit velocity to obtain impact velocity-residual velocity curves. Total of 360 ballistic experiments were conducted and ballistic limit velocities of projectiles were tabulated in Table 2.3. Experimental study concluded that ballistic limit and absorbed impact energy is directly related with projectile nose geometry. Sharper nose geometry (hemispherical and chisel) was found to be relatively more efficient in penetration while flat-nosed projectiles were observed to be least efficient in penetration. Difference of ballistic limit velocities of

most and least efficient projectiles was found to be 326 $m.s^{-1}$ for the thickness of 14 mm.

Table 2.3. Ballistic limit of projectiles used in experimental study (Source: Jordan & Naito, 2014).

Projectile	**Target Thickness (mm)**	**Ballistic Limit Velocity (v_{bl}, $m.s^{-1}$)**	**Shots used in calculation of v_{bl}**	**Error ($m.s^{-1}$)**
RCC	14	828	4	3
30 Cal FSP	14	813	4	4
Modified 30 Cal FSP	14	680	4	9
Conical	14	677	4	7
Chisel	14	598	4	8
Hemispherical	14	535	4	6
RCC	9	541	4	9
30 Cal FSP	9	541	4	7
Conical	9	474	6	14
Modified 30 Cal FSP	9	441	4	2
Hemispherical	9	398	4	9

Latest studies in 2018 included the penetration behavior of sandwich and multilayered structures against different levels of impact velocities (Guo et al., 2018; Huang, Zhang, Deng, & Jiang, 2018; Kõrgesaar, Romanoff, Remes, & Palokangas, 2018; Kyner, Dharmasena, Williams, Deshpande, & Wadley, 2018; D.-W. Lee, Park, Park, Choi, & Song, 2018; D. Li et al., 2018; X. Li et al., 2018; Qin, Zheng, Zhang, Yuan, & Wang, 2018; Zhou, Mei, & Zhang, 2018; L. Zhu, Guo, Li, Yu, & Zhou, 2018; W. Zhu, Huang, Feng, & Stronge, 2018). Zhu et al. investigated the effect of lateral displacements on the penetration behavior of polyethylene-reinforced cross ply laminates (W. Zhu et al., 2018). Experimental study included ballistic tests of plates with varying thicknesses ranging between 2 to 8 mm, against conical tipped projectiles with different nose angles. Schematic of experimental set-up with specimen fixturing conditions were presented in Figure 2.19.

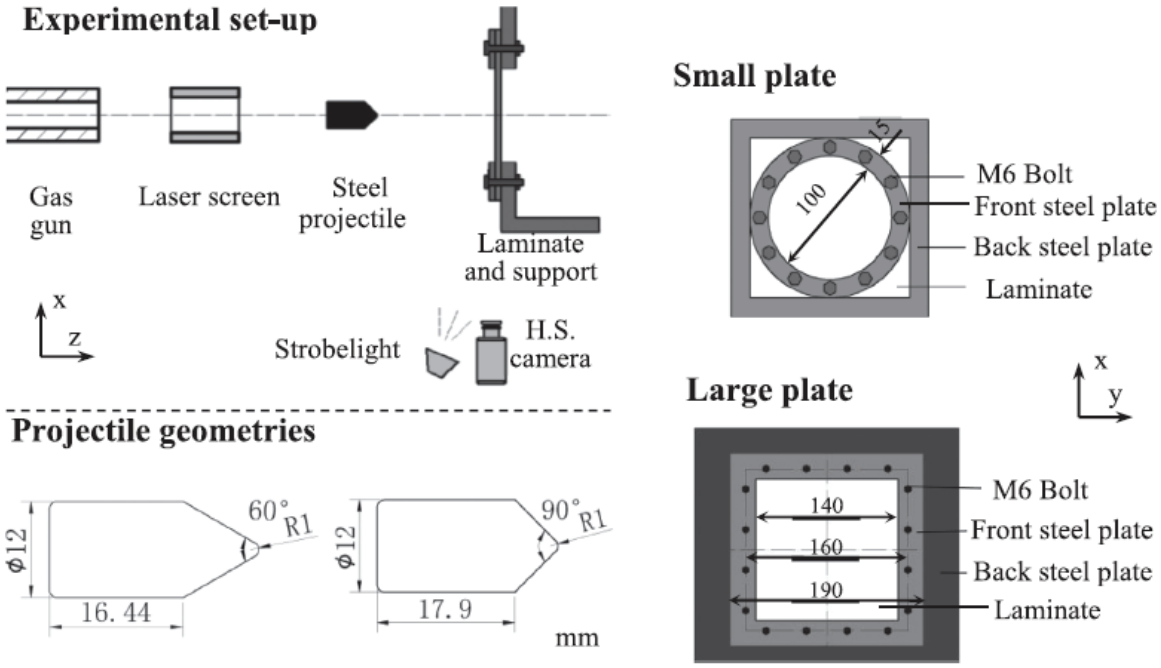

Figure 2.19. Test set-up, projectile geometries and fixturing types applied in the study (Source: W. Zhu et al., 2018).

Experimental study showed that global behavior of the laminate such as bulging or bending is more effective on the energy absorption characteristics of the projectile rather than total number of failed fibers. Projectile nose geometry was found to affect the localized direct tension of fibers, indicating more stretching on tests with sharper nose geometry, which further resulted in reduced energy absorption.

Huang et al. investigated the ballistic response of the multilayered aluminum and polymer plates (Huang et al., 2018). In this study, combinations of polycarbonate, polymethyl methacrylate and 2024-T4 aluminum were subjected to ballistic tests against blunt and ogive-shaped projectiles. A gas gun with impact velocities between 60 and 150 $m.s^{-1}$ was occupied for dynamic testing while quasi-static tensile tests were also conducted to determine the mechanical properties. Experimental set-up was given on Figure 2.20 while test configuration was tabulated in Table 2.4.

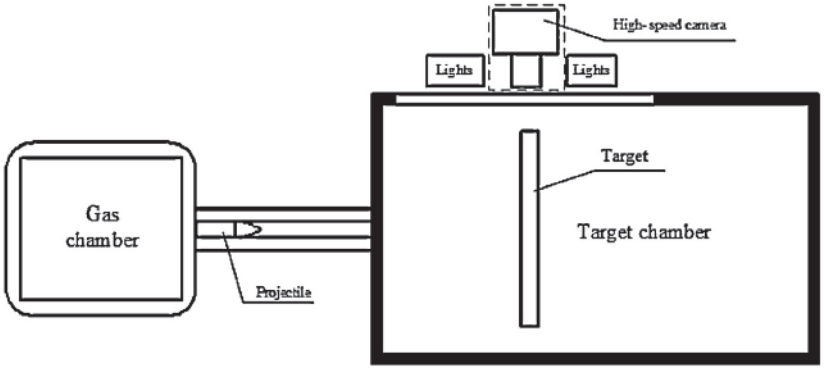

Figure 2.20. Schematic of experimental set-up used in the study (Source: Huang et al., 2018).

Table 2.4. Configuration of layers used in experimental study (Source: Huang et al., 2018).

Target Code	Configuration	Material	Thickness (mm)
AL-2	Monolithic layer	AA2024-T4	2
AL-3	Monolithic layer	AA2024-T4	3
AL-4	Monolithic layer	AA2024-T4	4
PC-F	Bi-layer: PC in front	PC+AA2024	2+2
PC-B	Bi-layer: PC in back	AA2024+PC	2+2
PM-F	Bi-layer: PMMA in front	PMMA+AA2024	2+2
PM-B	Bi-layer: PMMA in back	AA2024+PMMA	2+2

Ballistic test results showed that blunt nosed projectile indicated deformation mode of plug formation independent from tested configuration while petaling was observed on tests of ogive-nosed projectile with number of petals changing with the configuration of tested structure. The polycarbonate was found to perform better when positioned on impact side against blunt nosed projectile, outperforming the monolithic aluminum plate with same mass. Also, performance of polycarbonate was noted to be better in terms of ballistic limit velocities when compared to polymethyl methacrylate. Ballistic limit velocity of polymethyl methacrylate was found to be less than monolithic aluminum plate when subjected to impact of blunt and ogival-nosed projectiles. Figure

2.21 summarizes the experimental work by comparison of ballistic limit velocities for all combinations aforementioned above.

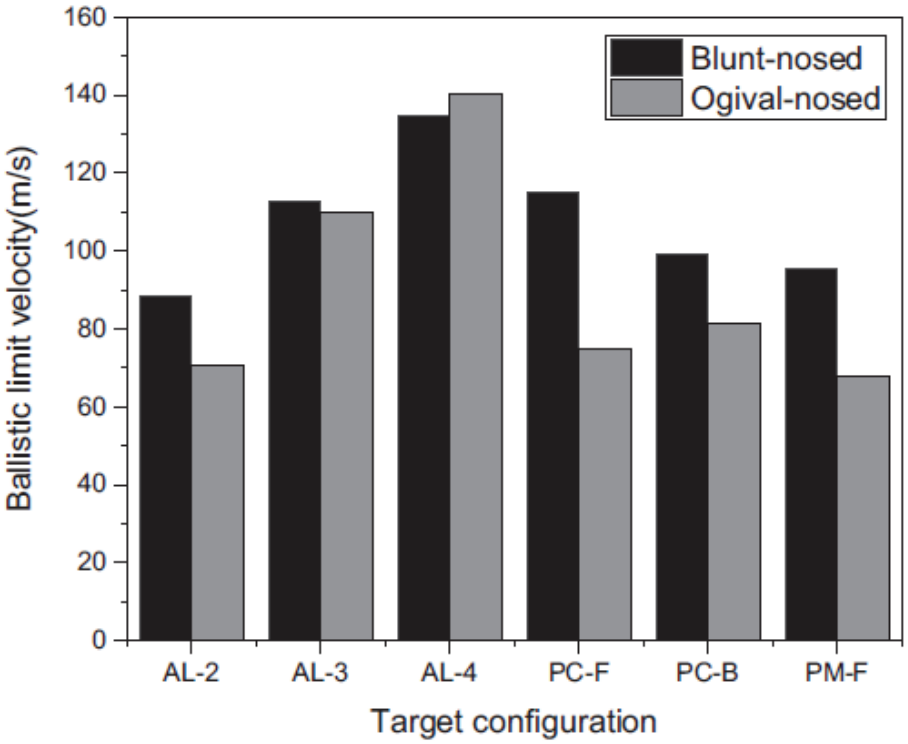

Figure 2.21. Comparison of ballistic limit velocities
(Source: Huang et al., 2018).

Rather than solid multilayered structures, alternative geometries with repeating layer geometries are also present and Zhou et al. studied impact response of a composite multilayer array structure (Zhou et al., 2018). In this article, a novel geometry with three layers of composite spherical structures were sandwiched between four layers of hybrid composite layers. Hybrid composite layers were made from Q235B naval steel, combined with glass fiber reinforced prepregs of SW220 fiberglass and 430LV resin. Each laminate included three layers of steel and two layers of composite. Remaining units of multilayered structure, namely as array of composite spheres, were manufactured by filament winding of composite over buoyant core structure. Sketches of both layers were presented in Figure 2.22.

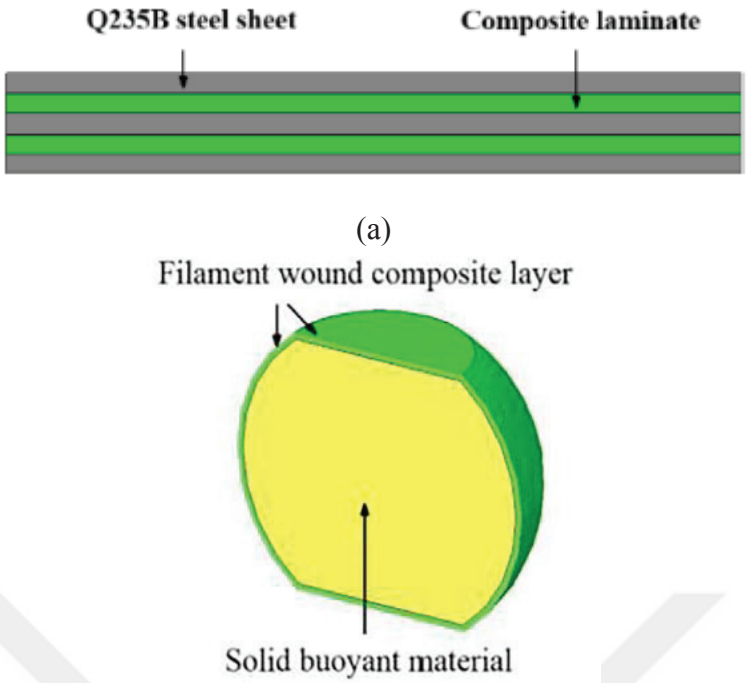

Figure 2.22. Composite layers (a) and spherical structures (b) used as arrays in the study (Source: Zhou et al., 2018).

After the mechanical characterization studies of constituents, low velocity impact tests were conducted to the multilayered structure. For this purpose, a drop weight testing equipment with a spherical impactor was occupied with additional mass of 300 kg and impact height of 4.13 m. Experimental study was then modeled in ABAQUS/Explicit commercially available finite element software with using related material model for each parameter; Johnson-Cook material model was used to simulate the behavior of steel while material model of Deshpande-Fleck crushable foam was used to mimic the behavior of buoyant material. Hashin damage criteria was used to model the deformation behavior of glass fiber reinforced layers. Experimental and numerical results showed that nearly half of the impact energy (46%) was mitigated by first layer elements and laminate while remaining portion of absorbed energy is almost evenly distributed to the remaining constituents of the multilayered structure. Other important output of the study was noted as higher percentage of impact energy was mitigated by layers (72%) rather than composite array of elements. Comparison of energy absorption percentages of constituents were presented in Figure 2.23.

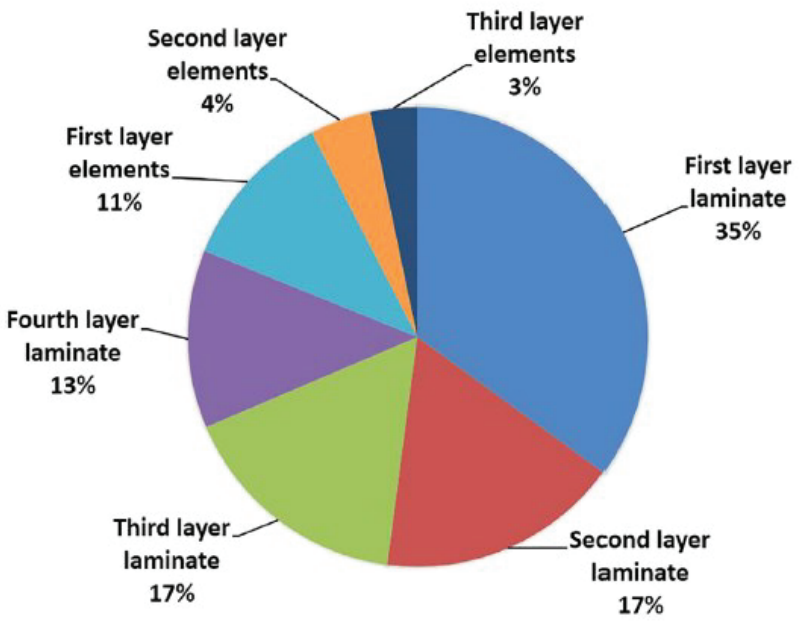

Figure 2.23. Energy absorption percentages of proposed structure (Source: Zhou et al., 2018).

CHAPTER 3

MANUFACTURING OF INVESTIGATED STRUCTURE AND SPECIAL TESTING EQUIPMENT

The following chapter summarizes the manufacturing of investigated core structure, composite plates that were used in later stages of experimental study and special testing equipment for performance evaluation tests of core structure.

3.1. Manufacturing of Core Structure

Core structure investigated in this study can be defined as combined geometry which includes a hemispherical dome and cylindrical portion. This geometry was achieved by deep-drawing sheet metals of 304 L stainless steel, whose elemental ingredients according to EN 10088-3 is given in Table 3.1. (DIN, 2014).

Table 3.1. Chemical composition of AISI 304L stainless steel
(Source: DIN, 2014).

C (%wt)	Cr (%wt)	Ni (%wt)	Mn (%wt)	S (%wt)	P (%wt)
0.03	17.5-19.5	8.0-10.0	2.0	0.030	0.045

This material was selected for its superior ductility, strong strain rate dependent behavior, very good corrosion resistance and relatively cheaper cost. Highly ductile metals are well known to be energy absorbing structures and this is favored on applications of armor structures. Strain rate dependency is advantageous on engineering problems where dynamic and post-yield behavior is important as materials are able to endure increased stresses at same strain values at elevated strain rates. High corrosion resistance is vital for an armor component as the structure is used during four seasons with varying temperature and humidity values and rust is known to alter the mechanical properties of every metal. Cost of each element in a multi-component armor structure is very important as on serial production level, defense industry produce tens of thousands of a proven armor structure which may cost millions of dollars more when high cost

components are used. It should be also noted that Turkish national industry on metal forming and tooling has a solid experience on 304 L stainless steel and this allows the candidate structure to be easily produced domestically with relatively less effort when compared with thick, monolithic armors.

3.1.1. Manufacturing of Combined Geometry Shells

Core materials investigated in this work is a combined geometry shell which is a single unit that combines a hemispherical shell attached and a cylindrical segment. In order to reduce the structural weaknesses of any sort of assembly (welding etc.), deep-drawing method was chosen to manufacture this geometry. Occupation of this method is also advantageous as this deep-drawing method needs relatively less know-how and yields high production rate, easy and low-cost operation.

Basically, deep-drawing operation includes 3 different parts namely as punch, blank and die. As first step of forming operation, blank was fed between the upper and lower pieces of die. Then, a punch having the inner geometry of combined geometry shells were guided in longitudinal direction to achieve desired shape. During forming, it is essential to apply appropriate amount of axial force to blank between parts of die to prevent wrinkling. Required dimensions of core structure were achieved by cutting the excess length on a CNC lathe after deep-drawing operation. Exact images of investigated core structures were given in Figure 3.1 while dimensions of specimens were tabulated in Table 3.2.

Figure 3.1. Technical drawings and exact images of core structures.

Table 3.2. Geometrical parameters of core geometries.

Designation	Outer radius (mm)	Thickness (mm)	Total Height (mm)
R75t05	15	0.50	13.00
R75t1	15	1.00	13.00

It is presumed that, as the implied production method is based on forming of sheet metal on plastic level, operation will result in variation of thicknesses along the geometry. This theory was proven during the study by conducting thickness measurements for investigated geometries and results were presented in Figure 3.2. During the study, measurements were done with a pre-defined interval and point clouds of thickness values were obtained. Then, these values were converted into a 3D shape which indicates the overall thickness of each region with a color scale. It can be seen from figure that thicknesses of the structures vary with distance from apex and this also indicates that residual stresses and strains also vary within the structure. It is vital to have such information at earlier stages of the study as future numerical studies must include these post-yield stresses and strains to obtain more realistic and consistent results with respect to conducted experiments. For this purpose, modeling of the deep-drawing operation was done and numerical specimens created to better mimic the performance evaluation tests. Method followed the basics that has been given in prior art (Alper Tasdemirci, Kara, Turan, & Sahin, 2015; Alper Tasdemirci, Sahin, Kara, & Turan, 2015).

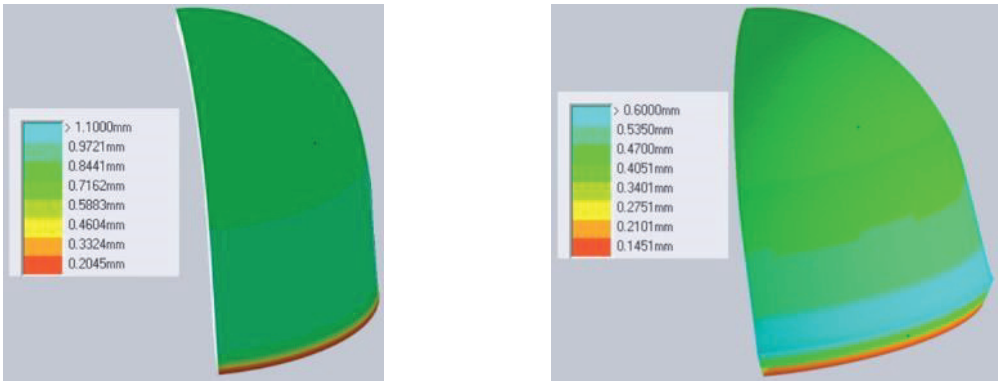

(a) (b)

Figure 3.2. Measured thickness variation contours of combined geometry shells; (a) R75T1, (b) R75T05 specimens (Source: Kara, 2015).

3.2. Manufacturing of Composite Face Sheets

Upcoming chapters of this thesis include ballistic testing of the sandwich structures which includes aforementioned combined geometry to be used as core units. For this purpose, Glass Fiber Reinforced Polyester (GFRP) was selected as face and backing material of sandwich structures with fiber orientation in 0°/90° due to its superior strength to weight ratio, relatively low material cost and easier manufacturing operations. Manufacturing of composites includes several methods such as hand lay-up, resin transfer molding (RTM), filament winding and tube rolling. In this study, Vacuum Assisted Resin Transfer Molding (VARTM) method was occupied to fabricate composite plates and create sandwich structures. In VARTM process, fiber is cut in desired dimensions and placed under plastic bagging to form an air tight environment. After that, externally mixed resin was fed from carefully positioned intake points and spread through fibers with the help of vacuum from manifold, resulting a full and homogeneous wetting throughout the composite plates. Image of a GFRP plate under vacuum during VARTM process is given in Figure 3.3. During the study, square plates with side dimensions of 900 mm were created.

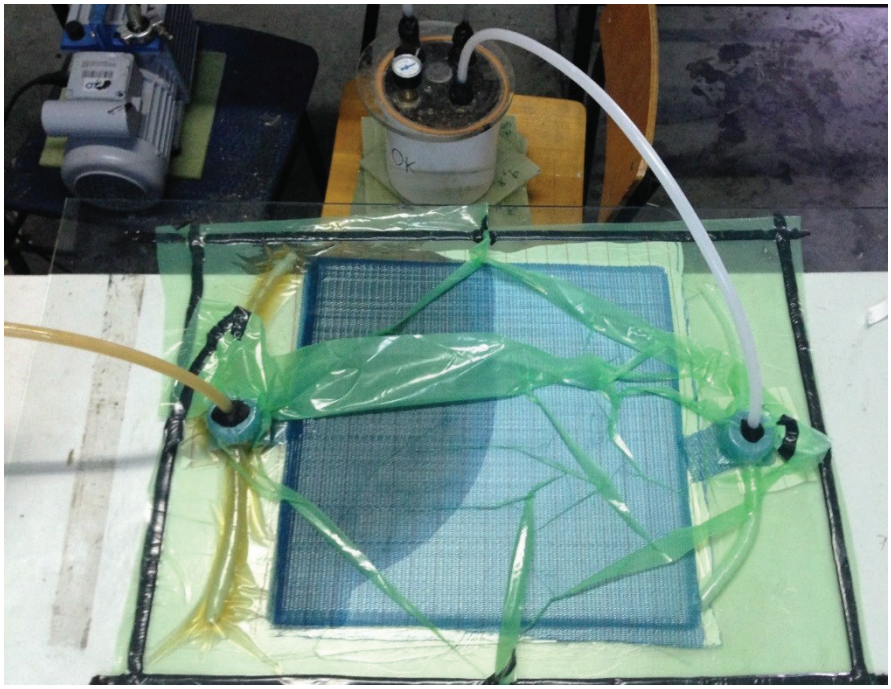

Figure 3.3. Manufacturing of composite plates using VARTM method.

After completion of VARTM process, composite plates were cut into square shapes with a side length of 180 mm using a water-cooled diamond cutter. Finally, square shaped composite plates were surface grinded to achieve flat and parallel surfaces with a thickness of 5 mm. Image of a composite plate after surface grinding is given in Figure 3.4.

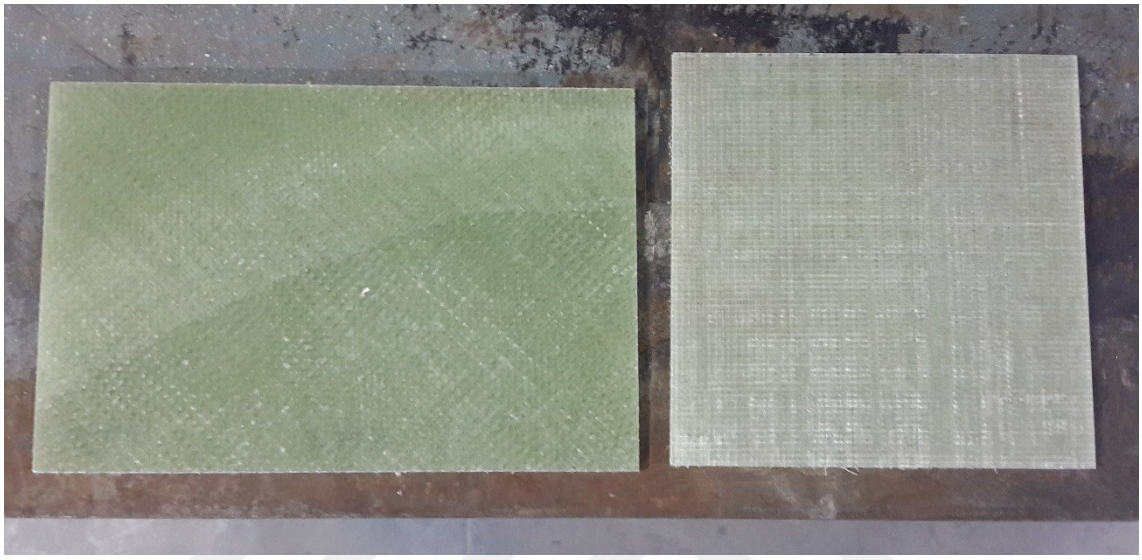

Figure 3.4. Composite plates after surface grinding operation.

3.3. Manufacturing of Special Testing Equipment

Scope of this study is to investigate the penetration behavior of the aforementioned combined geometry core structures by conducting performance evaluation tests at different strain rates. In order to mimic the real-life conditions better, experimental study included penetration tests that requires to be completed at quasi-static, intermediate and high strain rates. Implementation of a non-conventional testing method resulted in necessity of design and manufacturing of special testing tools and equipment which was fully detailed in this subsection.

Previous studies investigating penetration performance mainly focused on three penetrator geometries with blunt, conical and hemisphere tips (Alavi Nia & Hoseini, 2011; Babaei, Shokrieh, & Daneshjou, 2011; Deng, Zhang, & Cao, 2012; Gupta, Iqbal, et al., 2008; Mines et al., 1999). According to information obtained from literature, penetrators with a common diameter of 7.62 mm to represent armor piercing (AP) rounds of NATO were designed and AISI 4140 steel was selected as penetrator material

due to its capability of thermal hardening. Manufacturing of the penetrators were initiated by diameter reduction of bar material to achieve the target of 7.62 mm on a CNC lathe, followed by forming of penetrator tips to desired shape. In addition, heat treatment operations were conducted and final hardness of 52 HRC was achieved which corresponds to an average yield stress of 1500 MPa with technical data available online ("AISI 4140 Steel, oil quenched, 205°C (400°F) temper, 25 mm (1 in.) round,"). Photographs of penetrators used in tests at quasi-static and intermediate strain rates were given in Figure 3.5.

(a)

(b)

Figure 3.5. Penetrators used in tests at (a) quasi-static, (b) intermediate strain rates.

Before the study was initiated, it was expected to observe different types of damage behavior such as folding of structure, variations in tearing of different segments

of geometry and inverse forming which may lead to excess displacement values. Thus, in addition to penetrators described above, it is obligatory to design and manufacture a custom specimen fixture which allows greater displacements to be reached while constraining the movement of specimen by holding it stationary during testing. For this purpose, specimen fixture given in Figure 3.6 was designed to keep the specimen fixed during single core unit testing. Center of the fixture was drilled thoroughly and threaded for centering plug, which allows observing excessive displacement values without interference of penetrator and specimen fixture. Moreover, specimen fixture was designed in such a way that one face is planned to test single core unit while opposing face is capable of constraining specimen with other core units as in a sandwich structure. The AISI 4140 was also selected as specimen fixture material but no hardening operation was conducted since fixture is not going to be subjected to loads. Photographs of specimen fixture with single core unit and radial confinement condition is given in Figure 3.6.

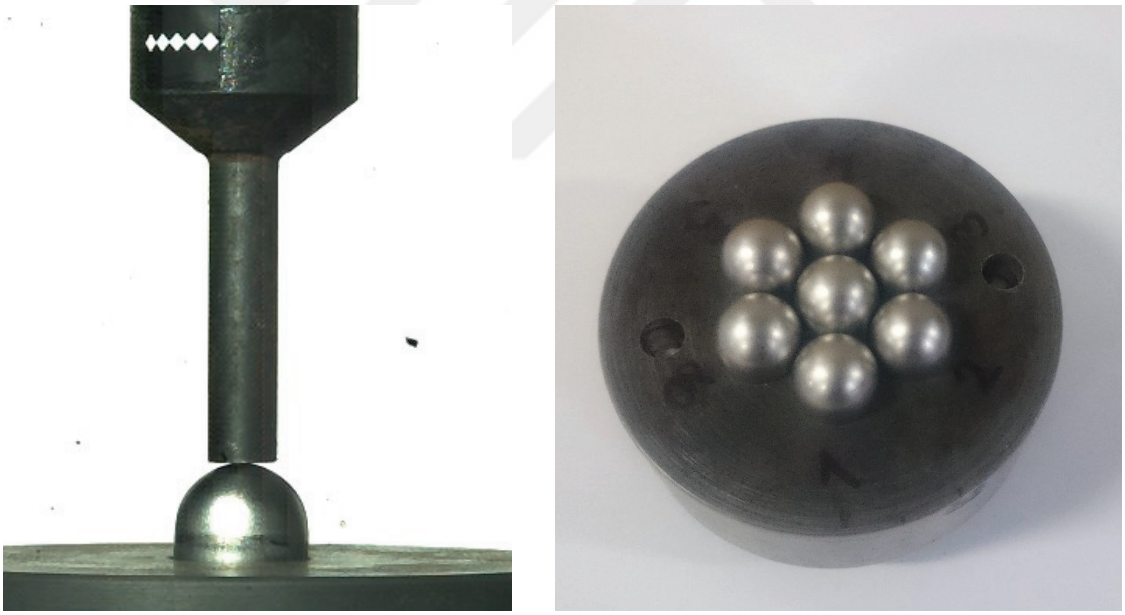

Figure 3.6. Specimen fixture with single core and radial confinement set-ups.

CHAPTER 4

MECHANICAL CHARACTERIZATION AND PERFORMANCE EVALUATION TESTS OF CORE STRUCTURE

This chapter of the thesis summarizes the mechanical characterization studies conducted on 304 L stainless steel and performance evaluation tests (penetration tests) that were done on both geometries. Results of numerical study were also given in subsections of this chapter.

4.1. Mechanical Characterization of 304 L Stainless Steel

As noted in scope of the study, investigation of penetration behavior included both experimental and numerical work to be done. A proper numerical study must include mechanical properties of investigated material and this can be obtained either from literature or by conducting mechanical characterization studies. 304 L stainless steel has already been characterized by previous studies (Karnesky, Damazo, Chow-Yee, Rusinek, & Shepherd, 2013; Maurel-Pantel, Fontaine, Thibaud, & Gelin, 2012) but it should be noted that each study indicates its very own parameters and this may result in deviation from actual behavior under loading at different strain rates. Therefore, it was decided to conduct mechanical characterization studies on the 304 L stainless steel. Material which was also used in deep-drawing operations were obtained from the steel supplier in sheet metal form and specimens were manufactured to conduct tension tests at quasi-static and high strain tests to cover the material behavior at all strain rates. More information on each testing method was given with details in following sub-sections.

4.1.1. Quasi-Static Strain Rate Tests

Mechanical characterization studies were initiated by conducting tension tests at quasi-static strain rates. For this purpose, ASTM E8M testing standard was selected as basis for experimental study on both specimen geometry and testing conditions.

Specimens were manufactured by using the Wire-cut Electrical Discharge Method to obtain the geometry noted on standard and final shape of specimens used in quasi-static and high strain rate tests were given in Figure 4.1 in which the geometry given on the right was used during tests at quasi-static strain rates.

Figure 4.1. Specimens used in mechanical characterization studies.

4.1.2. High Strain Rate Tests

Dynamic behavior of the AISI 304 L stainless steel was investigated using a Split Hopkinson Tension Bar. The testing equipment is highly preferred in mechanical characterization of various materials at high strain rates and an example of testing equipment is given in Figure 4.2.

Figure 4.2. Split Hopkinson Tension Bar used in high strain rate tests.

Material properties of bars occupied on Split Hopkinson Tension Bar testing equipment were tabulated in Table 4.1.

Table 4.1. Material properties of SHTB test setup.

Material	**Density (kg/m^3)**	**Modulus of Elasticity (GPa)**	**Poisson's ratio**	**Yield Strength (MPa)**
316L Stainless Steel	8000	193	0.3	300

Testing with Split Hopkinson Tension Bar takes the elastic wave propagation theory as the base line and method can be summarized as follows: upon release of pressurized gas from gas gun, striker is propelled to hit the incident bar and a one-dimensional stress wave is created initially at the impact. Then, created stress wave propagates along the incident bar and initial form of wave is captured via strain gages of incident bar as "incident wave". As the stress wave reaches the specimen contacting end of incident bar, some portion of the incident wave is transferred to specimen and deforms it plastically while rest is reflected back from free-end, named as "reflected wave". Finally, stress wave which deforms the specimen is also propagated to transmitted bar and it is recorded as "transmitted wave". After the test is completed, these waves were used to obtain stress-strain curves of investigated material. An example of these waves was presented in Figure 4.3.

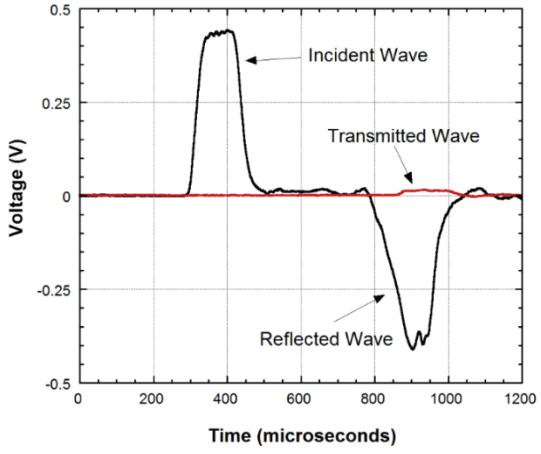

Figure 4.3. SHTB voltage history of a test done on AISI 304L stainless steel.

Voltage-time curves recorded during high strain rate tests were first converted into strain-time data using the (4.1). Note that V_{exc}, GF and K_{gain} are the parameters that are unique to each testing equipment and represent excitation voltage, gage factor and gain of the system, respectively.

$$\varepsilon(t) = \frac{4 \times Voltage(t)}{V_{exc} \times GF \times K_{gain}} \tag{4.1}$$

Strain histories of each wave is then used in following equations to obtain the strain ε, stress σ and strain rate $\dot{\varepsilon}$ of the material.:

$$\varepsilon(t) = -\frac{2C_b}{L_s}\int_0^t \varepsilon_r(t)\,dt \tag{4.2}$$

$$\varepsilon(t) = -\frac{2C_b}{L_s}\int_0^t \varepsilon_r(t)\,dt \tag{4.3}$$

$$\dot{\varepsilon}(t) = -\frac{2C_b}{L_s}\varepsilon_r(t) \tag{4.4}$$

where C_b represents elastic wave velocity of the bar, L_s represents the length of the specimen and A_s and A_b represent the sample and bar cross-sectional area, respectively. ε_i, ε_r, and ε_t are, respectively, the time-dependent strain data (strain histories) of the incident, reflected and transmitted waves measured via strain gages on the bar. It should be noted that equations given above were derived assuming that the forces at sample-bar interfaces are equal.

4.2. Results of Mechanical Characterization Studies

Further studies of this thesis require selection of an appropriate numerical model to successfully mimic the material behavior at desired physical conditions. Next section defines the material and damage model to be used in numerical studies, along with parameters found out through the experimental study.

4.2.1. Johnson-Cook Constitutive Equation

Penetration phenomenon investigated in this study involves plastic deformation of structure and it is obligatory to simulate this behavior in finite element modeling by using a material model which is capable to mimic material behavior beyond elastic region. Studies in literature indicate that Johnson-Cook material model is successful on modeling of engineering problems where large strains are reached and thus selected to be used in upcoming numerical studies. Constitutive equation, which defines the behavior upon applied forces of Johnson-Cook material model (Johnson, 1983) stands as follows:

$$\sigma_{eq} = \left(A + B{\varepsilon_{eq}}^{n}\right)\left(1 + Cln\left(\frac{\dot{\varepsilon}_{eq}}{\dot{\varepsilon}_0}\right)\right)\left(1 - T^{*m}\right) \tag{4.5}$$

$$T^{*} = \frac{T - T_r}{T_m - T_r} \tag{4.6}$$

where, ε_{eq} represent equivalent plastic strain, $\dot{\varepsilon}_0$ is a user defined reference strain rate, $(\dot{\varepsilon}_{eq})$ is the equivalent plastic strain and A, B, n, C and m are the material constants. Thermal parameters were defined in last bracket of (4.5) as T represents absolute temperature, T_r and T_m represent room and melting temperatures, respectively.

The failure of material was also represented in numerical studies and Johnson–Cook damage model was used (Johnson, 1983). This damage model calculates the fracture strain as given in following equation:

$$\varepsilon_f = \left[D_1 + D_2 e^{D_3 \sigma^{*}}\right]\left[1 + D_4\, ln\left(\frac{\dot{\varepsilon}}{\dot{\varepsilon}_0}\right)\right](1 + D_5 T^{*}) \tag{4.7}$$

where D_1, D_2, D_3, D_4 and D_5 are damage parameters and is ratio of stress triaxiality, defined as;

$$\sigma^{*} = \frac{\sigma_m}{\sigma_e} \tag{4.8}$$

In the current study, the stress state does not change a lot during penetration tests and damage mode focused on strain rate sensitivity of the material. As in fracture strain equation, effect of the thermal parameters was also neglected in damage model.

$$\varepsilon_f = D_1 \left[1 + D_4 \, ln\left(\frac{\dot{\varepsilon}}{\dot{\varepsilon}_0}\right)\right] \tag{4.9}$$

As mentioned in Chapter 4.1, mechanical characterization studies planned to be conducted at quasi-static and high strain rates to obtain material parameters since core units were planned to be subjected to loads at both strain rates. Previous studies on 304 L stainless steel also indicate that material is strain rate sensitive and this fortifies the need to conduct mechanical characterization studies at high strain rates (Lichtenfeld, Van Tyne, & Mataya, 2006; Nishida et al., 2015; Steichen, 1973; Stout & Follansbee, 1986). Mechanical characterization tests at quasi-static strain rates were done at three different strain rates namely as 10^{-3}, 10^{-2} and 10^{-1} s^{-1} and results were presented on Figure 4.4. Strain rate dependency of material is evident even in quasi-static regime and higher stress values were noted for a constant strain value when the strain rate was increased.

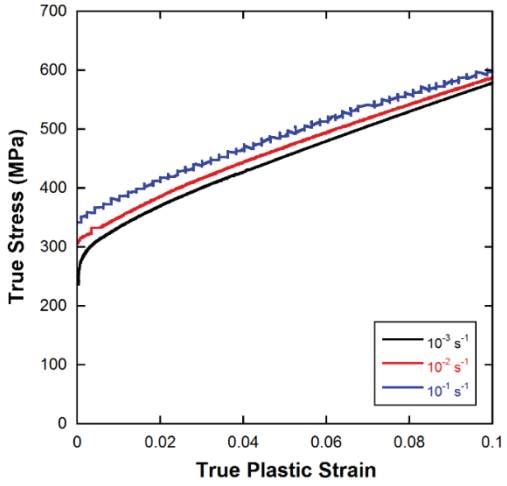

Figure 4.4. Quasi-static true stress – true plastic strain curves.

High strain rate tests were conducted at two different pressure levels of gas gun and change in impact velocity of striker bar resulted in difference in average strain rates of the tests. During dynamic tests, average strain rates of 900 s^{-1} and 1400 s^{-1} were calculated and high strain rate behavior of AISI 304 L stainless steel were given in

Figure 4.5. It can be noted from stress-strain graph that strain rate dependent behavior also continues to govern at dynamic tension test, indicating an increase in stress with increasing average strain rate, on a constant strain level.

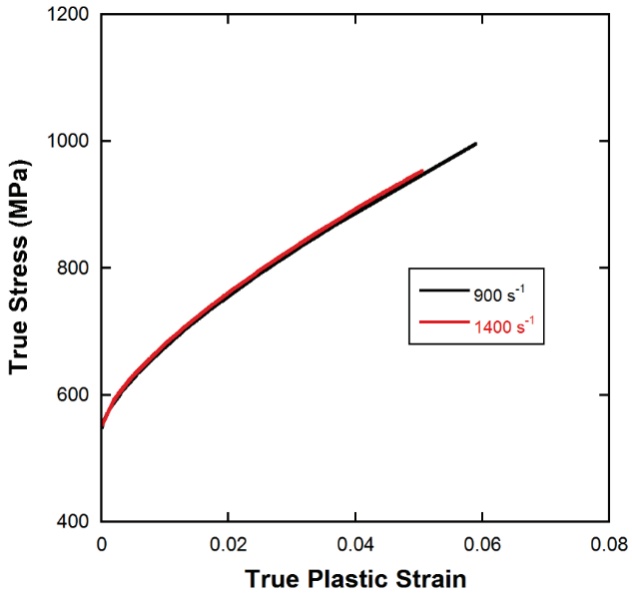

Figure 4.5. High strain rate behavior of 304 L stainless steel.

After completion of experimental study on mechanical characterization, quasi-static and high strain rate tests results were then evaluated to obtain parameters of Johnson-Cook material model. First bracket of the equation 4.5 indicates the strain hardening parameters of the material model and they were achieved by curve fitting of test results, given in Figure 4.6. Parameters *A*, *B* and *n* were used later on calculation of strain rate hardening parameters. Parameters found in strain hardening bracket of material model were adopted to obtain strain rate hardening constant C by conducting curve fitting on experimental results. After calculations made on KaleidaGraph software, curve fitted graph of stress-strain rate was achieved and were presented on Figure 4.7. This graph also indicates the strain rate sensitivity of the 304 L stainless steel over quasi-static and high strain rates.

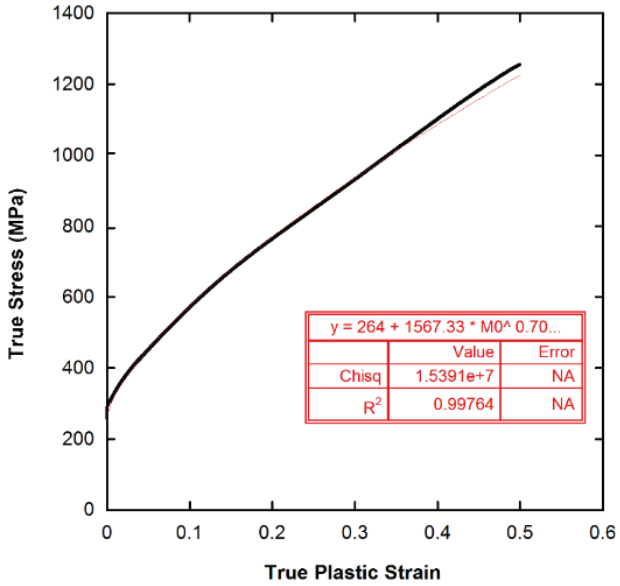

Figure 4.6. Curve fitting of test results.

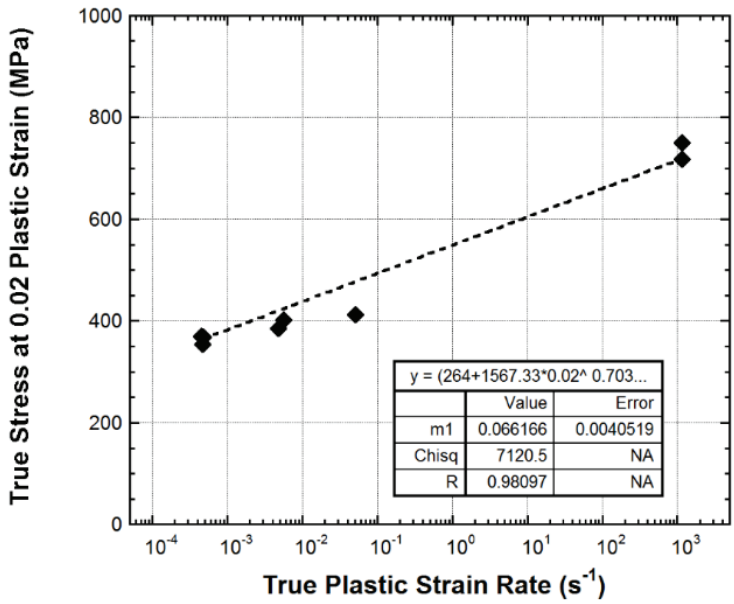

Figure 4.7. Strain rate sensitivity of AISI 304L stainless steel.

Test results and curve fitting of material behavior indicate the following material parameters which were tabulated in Table 4.2. It should be noted that these material constants have been proven on previous studies of same geometry and material against static and dynamic crushing events (Alper Tasdemirci, Kara, et al., 2015; Alper Tasdemirci, Sahin, et al., 2015).

Table 4.2. Parameters of Johnson-Cook material model used in numerical studies of AISI 304L stainless steel (Source: Alper Tasdemirci, Sahin, et al., 2015).

ρ (kg/m^3)	G (GPa)	E (GPa)	υ	A (MPa)	B (MPa)	n	C
7830	80	193	0.305	264	1567.33	0.703	0.067
$D1$	$D2$	$D3$	$D4$	T_R (^{o}K)	T_m (^{o}K)	m	D5
0.53467	0	0	-0.01913	296	1698	1.0	0

4.3. Performance Evaluation Tests of Core Structure

This section defines the experimental and numerical work done on as-received single core unit to investigate its penetration behavior. Testing equipment detailed in previous pages was used and results were compared with numerical studies in terms of force-displacement curves and absorbed energy levels up to fracture.

4.3.1. Tests of R75t1 Structure

The R75t1 structure given in Figure 3.1. was tested against blunt, conical and hemispherical tipped indenters at quasi-static and intermediate strain rate regimes. Tests at quasi-static strain rates were conducted at penetrator velocities of 0.013, 0.13 and 1.3 mm.s^{-1} which corresponds to average strain rates of 10^{-3},10^{-2} and 10^{-1} s^{-1} for a bulk material with same dimensions. Displacement of penetrator was traced with a camera and an extensometer attached to its body to avoid adding the body extension. Tests were also recorded with a stationary camera to observe the behavioral change with increasing displacement.

Performance evaluation tests of R75t1 specimens were initiated with quasi-static tests against blunt tipped indenter and results were given in Figure 4.8. It can be seen clearly from figure that local minimum and maximums of force change inversely with increase in indenter velocity. Failure of structure tend to occur at displacements above 6 mm for higher indenter velocities of quasi-static regime while increase in level of force and decrease in level of displacement was observed for failure of structure at lowest

indenter velocity of experimental study. Plug formation was observed after tests at all strain rates.

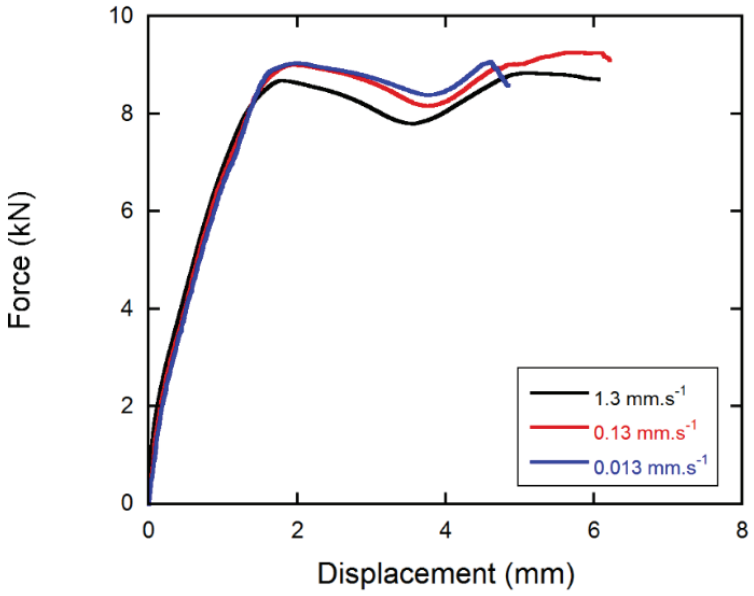

Figure 4.8. Comparison of test results of R75t1 structure against blunt tipped indenter.

Performance evaluation tests of R75t1 structure was followed by quasi-static tests against conical tipped indenter and results were given in Figure 4.9. Strong indenter velocity dependency was observed on behavior of structure and along with second local maximums, force levels on failure increased with increase in indenter velocity. Displacement levels at failure were found to be around 8 mm for all test conditions. Final form of deformation was found to be petaling for tests at lowest velocity level while symmetrical tearing was observed on specimens tested above cross head velocity of 0.13 $mm.s^{-1}$.

Quasi-static performance evaluation tests of R75t1 structure was finalized by conducting tests against hemispherical tipped indenter and comparative results were given in Figure 4.10. It was noted from figure that behavior of the structure did not change with indenter velocity and force-displacement curves obtained from tests were tend to fall nearly coincident. Tests were stopped around a displacement level of 12 mm and hemispherical cap formation was observed as main deformation mode for this structure.

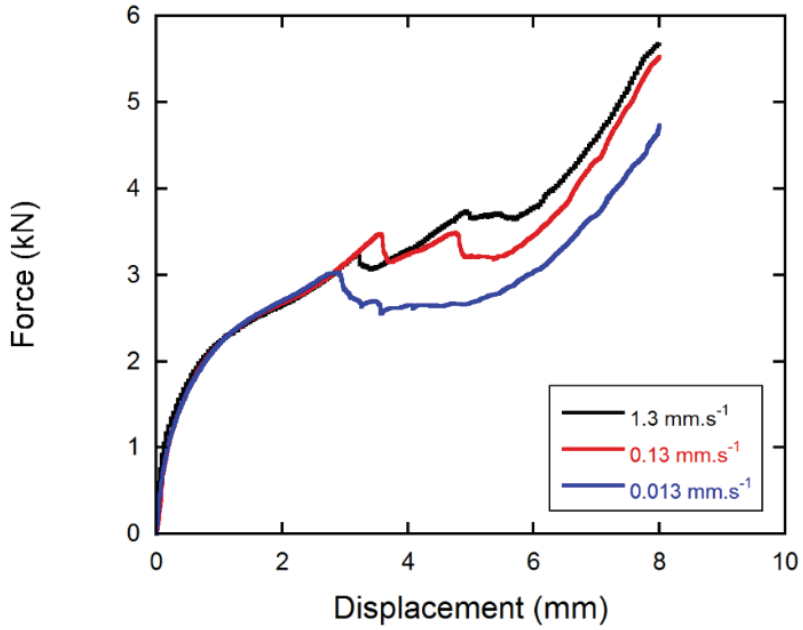

Figure 4.9. Comparison of test results of R75t1 structure against conical tipped indenter.

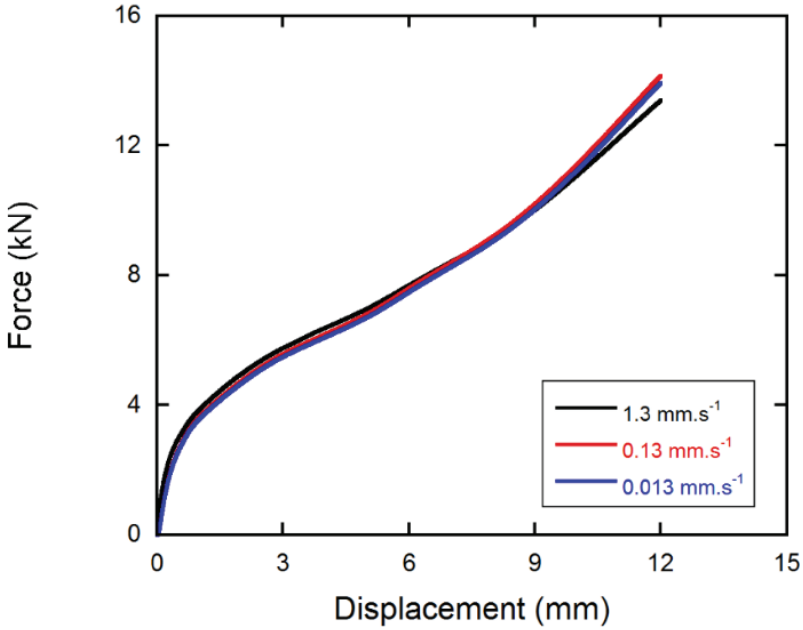

Figure 4.10. Comparison of test results of R75t1 structure against hemispherical tipped indenter.

Quasi-static performance evaluation tests' results of R75t1 structure conducted at 0.13 $mm.s^{-1}$ were compared in Figure 4.11. It is evident from figure that all of the indenters have their own unique characteristics which result in differences in shapes of force-displacement curves, values of forces and displacements at failure and final form of deformation. Among all of the indenters, lowest values of local and failure forces

were observed on tests of conical tipped indenter. Main reason behind this is the difference of contact surface area of indenters during tests; conical tipped indenter deforms the structure at the very tip of indenter and local progressive damage result in early failure while hemispherical tipped indenter leads to a more global failure with further increased contact surface area. In contrast to conical and hemispherical tipped indenters, contact surface area of blunt tipped indenter decreased with increased displacement; indenter was contacting the larger area of core structure at the initial displacement values which has led into global deformation but contact surface was reduced to perimeter of indenter tip after inward dimpling was occurred on structure. This resulted in a sharp increase of force on early displacement levels but also a sudden failure was observed at relatively low displacement values due to localization of applied force.

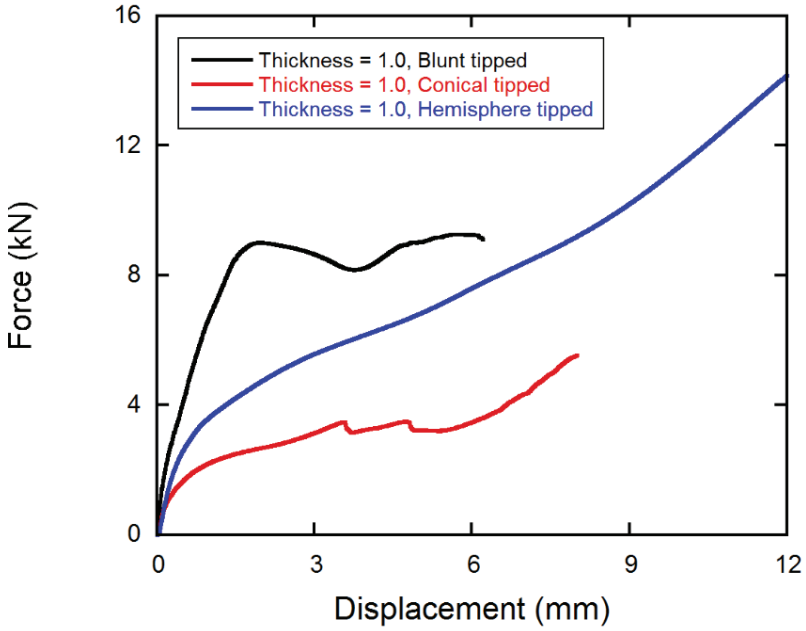

Figure 4.11. Comparison of test results of R75t1 structure against various indenters.

In addition to performed quasi-static tests on R75t1 core structure, performance evaluation tests at intermediate strain rates were also conducted. Fractovis Plus drop weight testing equipment was used during the study and impact speed was selected as 3.5 $m.s^{-1}$. Assembly weight of the indenter and striker was measured as 5.72 kg and no additional mass was used in drop weight mechanism since main aim of the tests were to

observe the effect of strain rate rather than impact energy on penetration behavior. Thus, impact energy was calculated as 35 J.

Force-displacement curves of quasi-static and intermediate strain rate tests of blunt and conical tipped indenters were given in Figure 4.12 and 4.13, respectively. It can be seen from both figures that effect of strain rate on quasi-static regime was also continued to govern the behavior at intermediate strain rates; strain rate dependency was observed for conical tipped indenter while further decrease in levels of fracture force and displacement was noted with increase in strain rate for blunt tipped indenter. Intermediate strain rate tests of hemispherical tipped indenter were unable to be completed since indenter tip was slipped to the either side of core structure during the experimental study.

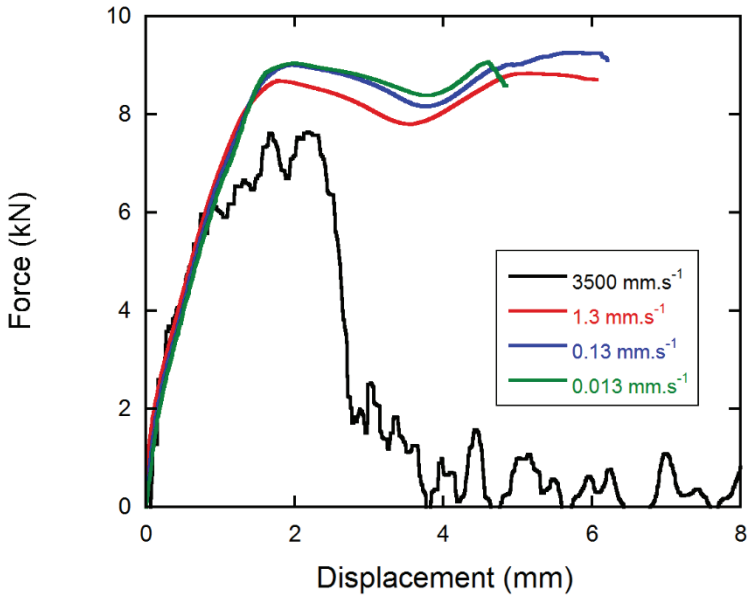

Figure 4.12. Effect of increasing cross-head velocity on the penetration behavior of R75t1 core structure against blunt tipped indenter.

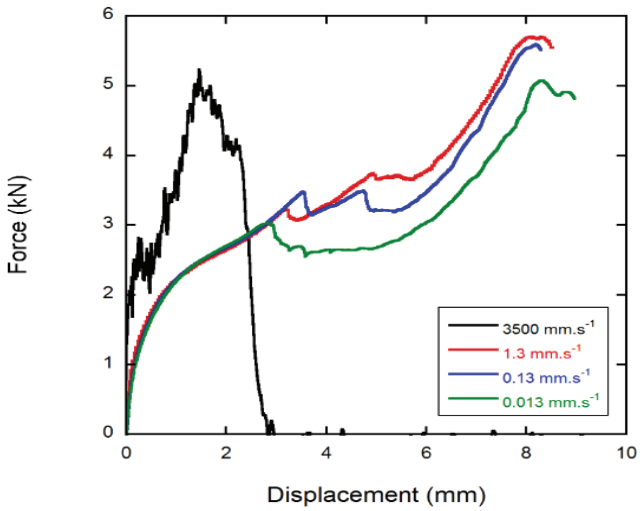

Figure 4.13. Effect of increasing cross-head velocity on the penetration behavior of R75t1 core structure against conical tipped indenter.

4.3.2. Tests of R75t05 Structure

Performance evaluation tests of R75t05 core structure was also conducted at quasi-static regime. Comparative test results of R75t05 core structure against blunt tipped indenter is given on Figure 4.14. It can be seen from graph that force-displacement curves follow a common trend regardless of test velocities of experimental study. Maximum force of 6 kN was noted at the displacement value of 12 mm and plug formation was observed on specimens after failure.

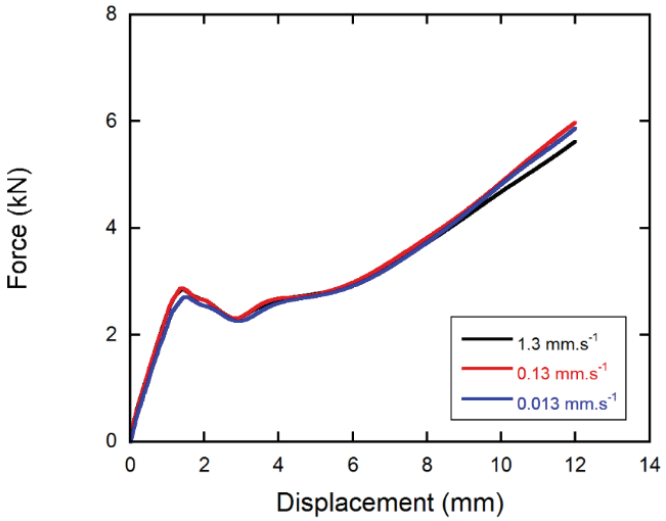

Figure 4.14. Comparison of test results of R75t05 structure against blunt tipped indenter.

Quasi-static performance evaluation tests of R75t05 core structure continued with tests against conical tipped indenter and experimental results were presented on Figure 4.15. Comparative force-displacement results show that R75t05 core structure indicates a common behavior which does not change with indenter velocity. Two local minimums and maximums were also observed during tests where failure occurred around a displacement value of 7 mm. Force level around failure was found to be 2 kN. Symmetrical tearing was observed on specimens as final deformation mode after experiments.

Performance evaluation tests of R75t05 core structure was completed with tests against hemisphere tipped indenter. Comparison of tests at different indenter velocities were given in Figure 4.16. Again, velocity independent behavior was observed on tests where tearing of inversely formed conical cap was noted on specimens.

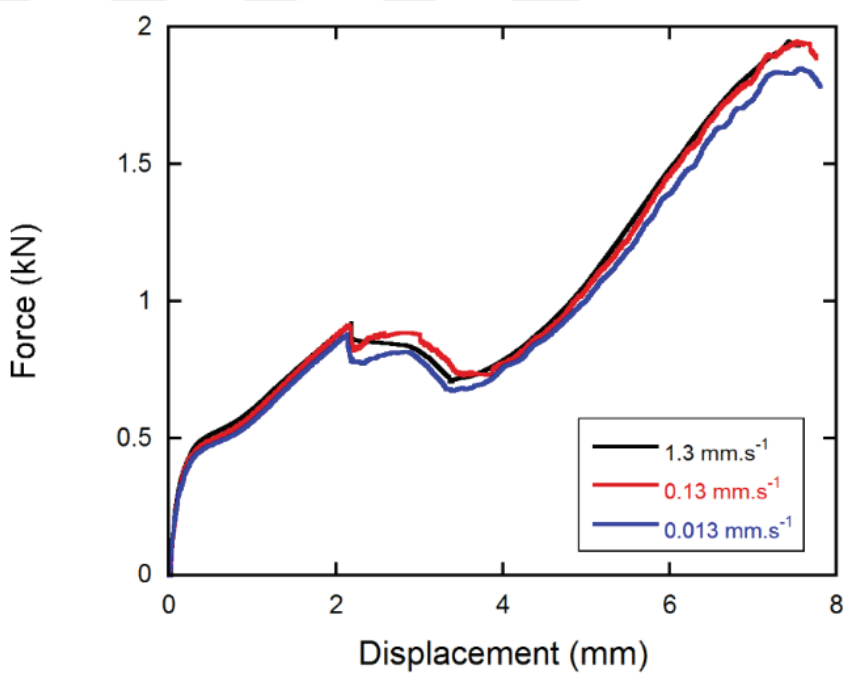

Figure 4.15. Comparison of test results of R75t05 structure against conical tipped indenter.

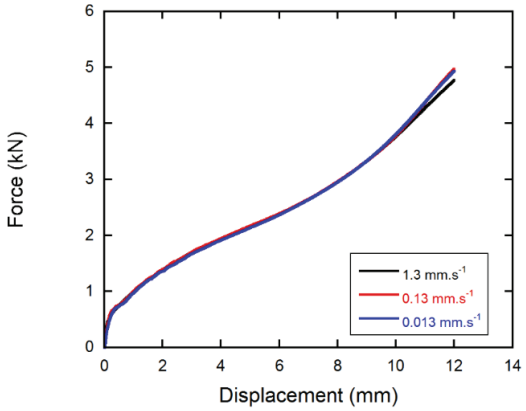

Figure 4.16. Comparison of test results of R75t05 structure against hemisphere tipped indenter.

Effect of tip geometry on behavior of R75t05 core structure is given on Figure 4.17. Tests completed at the cross-head velocity of 0.13 $mm.s^{-1}$ were selected for comparison and highest failure force along with highest displacement value was observed on tests against blunt tipped indenter, which was followed by hemispherical tipped indenter. Least failure force and displacement values were observed on tests against conical tipped indenter where local progressive deformation is believed to dominate the behavior of core structure. In addition to comments above, experimental study showed that when the thickness is reduced to 0.5 mm, deformation mode of shearing of core units requires higher energy than inversely forming with a hemispherical tipped indenter, indicating the result of difference between force-displacement curves of core units against blunt and hemispherical tipped indenters.

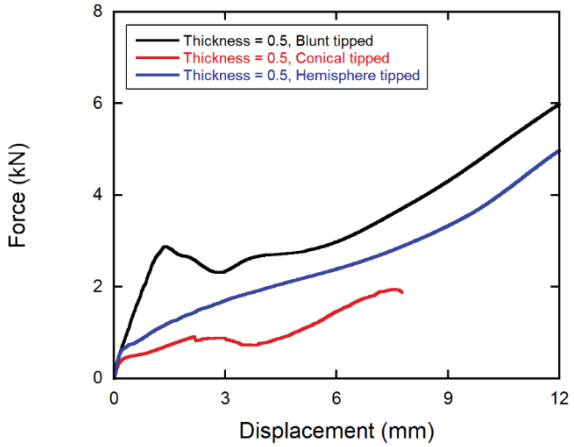

Figure 4.17. Comparison of test results of R75t05 structure against various indenters.

Experimental study also included tests of R75t05 geometry at intermediate impact velocities and same equipment used during drop-weight tests of R75t1 core units were occupied. Tests were conducted using blunt and conical tipped indenters at impact velocities of 3.5 $m.s^{-1}$ with impact mass of 5.78 kg, corresponding to an impact energy around 35 J.

Comparison of low and intermediate velocity tests against blunt tipped indenter was presented in Figure 4.18 and results show similar behavior as in R75t1 structure which indicates an alteration of force-displacement curve. Reduction of maximum force value beyond a threshold displacement level can be related with dynamic thinning of hemispherical region related with shear dominant behavior. Final deformation mode was noted to be plugging, as in low velocity tests.

Tests of R75t1 core units against conical tipped indenter were given in comparison with low velocity tests in Figure 4.19. Similar trend was observed on force-displacement curves of tests conducted at both velocity levels. Final form of deformation was found to be symmetrical tearing as in tests done at low velocity levels which also confirms the similarity of behavior with previously conducted experimental study.

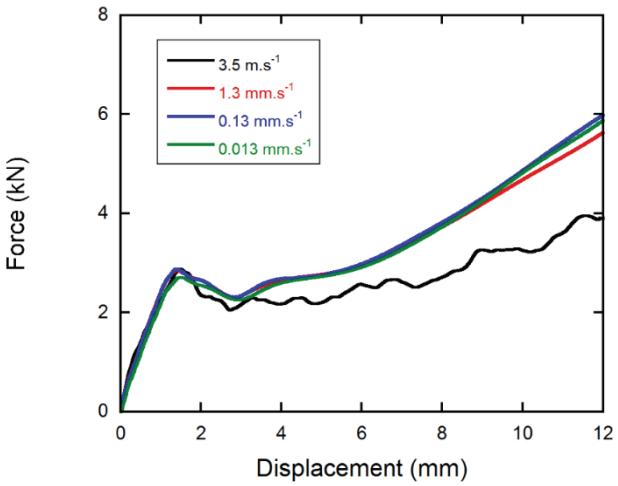

Figure 4.18. Comparison of test results of R75t05 structure against blunt tipped indenter at low and intermediate velocity levels.

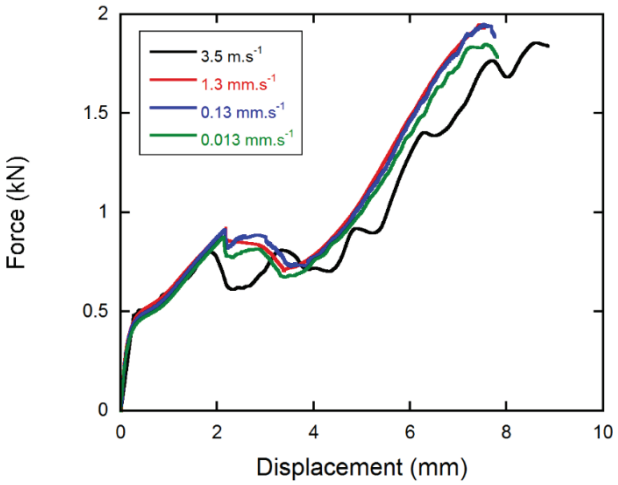

Figure 4.19. Comparison of test results of R75t05 structure against conical tipped indenter at low and intermediate velocity levels.

4.3.3. Investigation of Deformation Progress on Performance Evaluation Tests

During the preliminary experimental study, it was noted that it is impossible to track the progress of deformation during performance evaluation tests since presence of core units blocks the view of relatively smaller indenter, making it impossible to trace the deformation progress. In order to avoid this problem, displacement-controlled tests were performed to monitor the possible changes of deformation modes on critical points of force-displacement curves. These tests used the same methodology with reference experimental study and similar values of force and displacement were noted on pre-defined points which indicates very good correlation with previous tests. Displacement controlled tests were conducted at an indenter velocity of 0.13 $mm.s^{-1}$ except tests of R75t1 core structure where different types of deformation was observed after tests conducted at the indenter velocities of 0.013 and 0.13 $mm.s^{-1}$.

Performance evaluation tests' results of R75t1 specimens against blunt tipped indenter and deformation progress at increasing displacement levels are given in Figure 4.20. It is noted from figure that local maximum of the curves were around 2 mm and a sudden decrease of force was observed since deformation mode of progressive inward folding was started hemispherical cap. As the displacement was increased, small sized tears on radial direction and plug formation was noted which resulted in fracture of specimen.

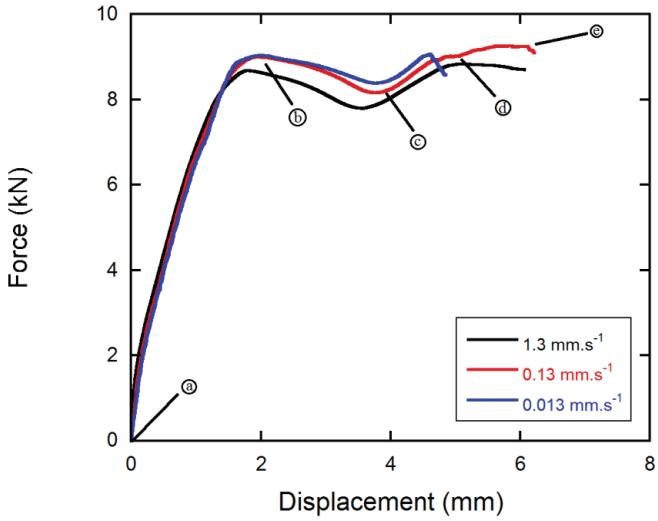

a) 0 mm b) 2 mm c) 4 mm d) 5 mm e) 6 mm

Figure 4.20. Deformation progress of R75t1 specimen against blunt tipped penetrator.

Comparison of performance evaluation tests' results of R75t1 specimen along with images taken from controlled displacement tests at the indenter velocities of 0.013 and 0.13 $mm.s^{-1}$ were given in Figures 4.21 and 4.22, respectively. Images of (a) and (b) of both figures indicated similar deformation that hemispherical cap was indented by penetrator. Tearing of hemispherical region was initiated around displacement values of 4 mm for both of tests and beyond that point, symmetrical tearing was observed for the test conducted at 0.13 $mm.s^{-1}$ while petaling was observed on specimen which was tested at 0.013 $mm.s^{-1}$.

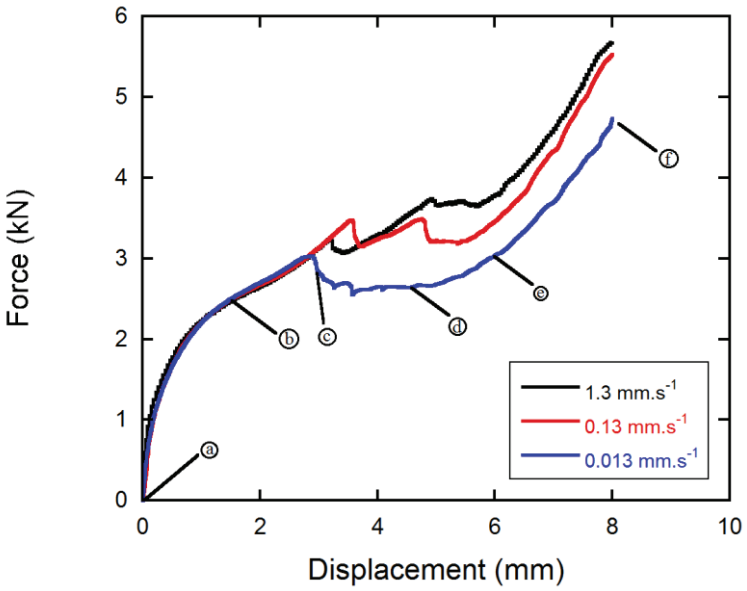


a) 0 mm


b) 1.5 mm


c) 3 mm


d) 4.5 mm


e) 6 mm


f) 8 mm

Figure 4.21. Deformation progress of R75t1 specimen against conical tipped penetrator (0.013 $m.s^{-1}$).

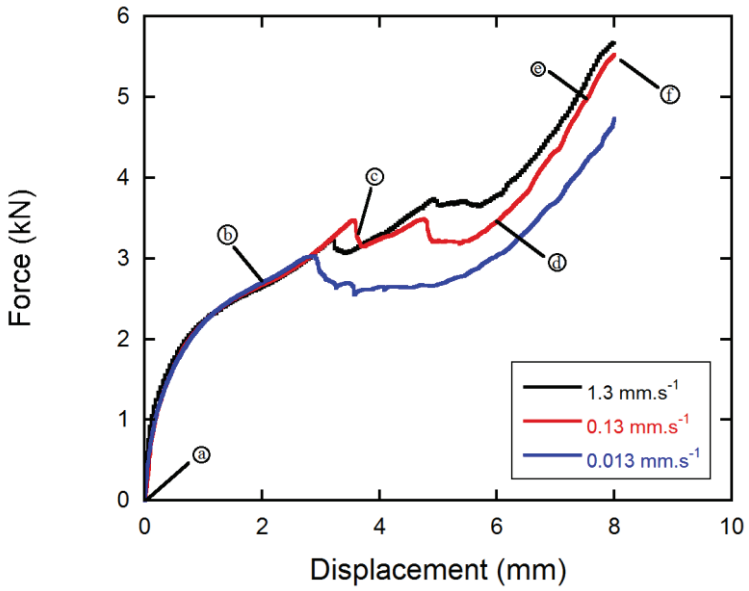

a) 0 mm b) 2 mm c) 3.6 mm

d) 6 mm e) 7.5 mm f) 8 mm

Figure 4.22. Progress of deformation of R75t1 specimen against conical tipped penetrator (0.13 m.s^{-1}).

Quasi-static performance evaluation test results of R75t1 core structure against hemispherical tipped indenter and images of deformation progress are given in Figure 4.23. Displacement controlled test indicated that hemispherical cap flattens around 3 mm of displacement and inward formed hemispherical cap is observed around displacements of 6 mm. Fracture occurred on core geometry due to radial shearing of inversely folded cylindrical segment at the force levels of 14 kN.

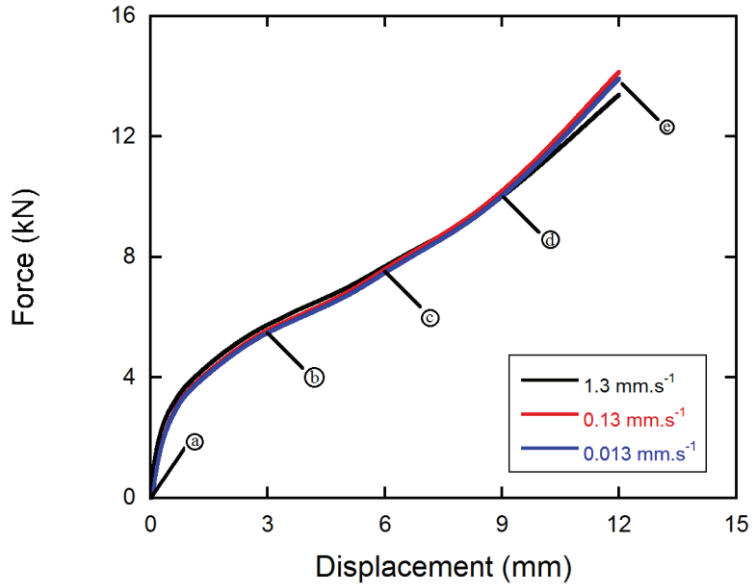

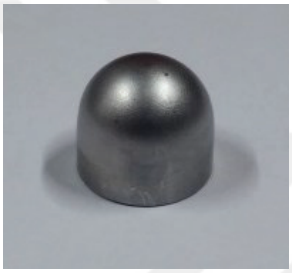
a) 0 mm


b) 3 mm


c) 6 mm


d) 9 mm


e) 12 mm

Figure 4.23. Deformation progress of R75t1 specimen against hemispherical tipped penetrator.

Controlled displacement tests were also conducted on R75t05 core structure and images of deformation progress along with test results against blunt tipped indenter were given in Figure 4.24. It can be seen from figure that deformation was initiated by flattening of hemispherical cap followed by inward folding around displacement of 4 mm. After that, cylindrical segment of core structure deformed with progressive folding on longitudinal direction which resulted in an increase in both force and displacements. Plug formation due to shearing at excessive displacements was observed on fracture of core structure.

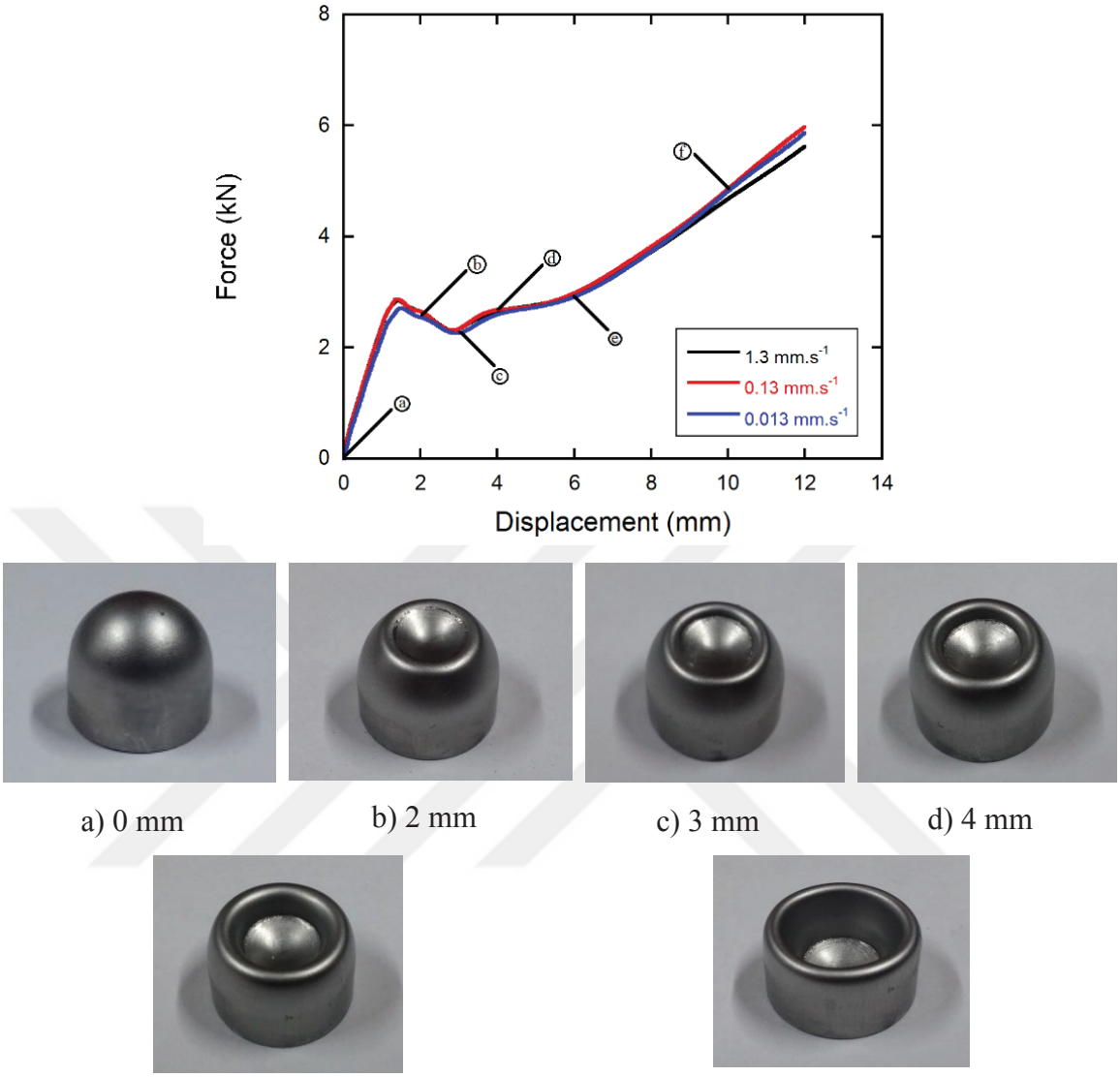

a) 0 mm b) 2 mm c) 3 mm d) 4 mm

e) 6 mm f) 10 mm

Figure 4.24. Force-displacement curves of R75t05 specimen and deformation progress against blunt tipped penetrator.

Progress of deformation on R75t05 core geometry in displacement-controlled tests against conical tipped indenter and experimental results are given in Figure 4.25. First few images taken during displacement-controlled tests revealed local deformation and indentation of hemispherical segment. Around a displacement of 4 mm, tearing was initiated on structure with simultaneous inward folding of hemispherical region. Symmetrical tearing was observed to be the main deformation mode while inward folding tended to propagate to cylindrical segment. It was noted that core structure did not able to carry loads beyond a displacement of 8 mm.

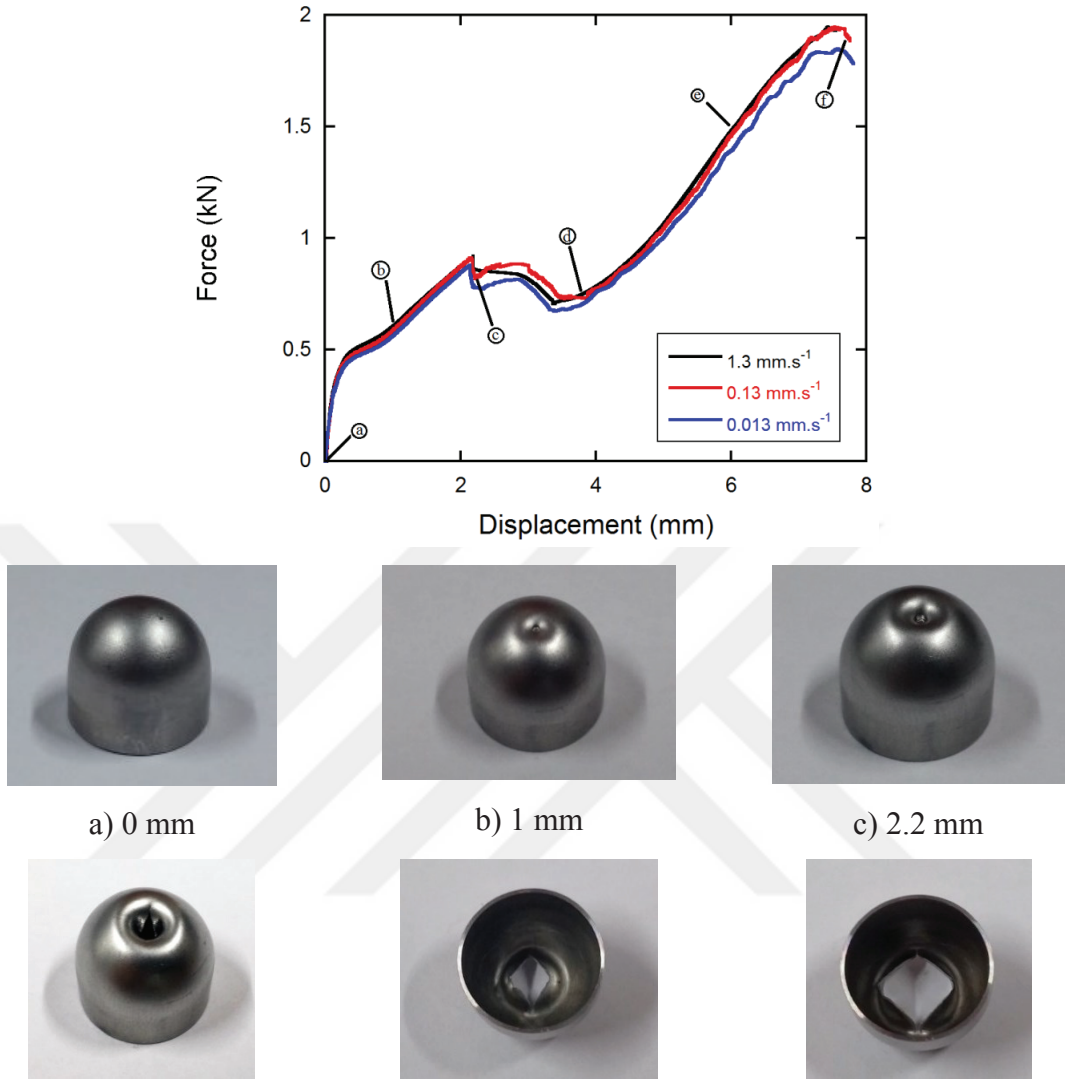

Figure 4.25. Force-displacement curves of R75t05 specimen and deformation progress against conical tipped penetrator.

Test results of R75t05 core structure against hemispherical tipped indenter and recorded images of deformation progress is given in Figure 4.26. Displacement controlled tests indicated that at the initial steps, indenter first flattened hemispherical segment of core structure which was followed by progressive inward folding and formation of hemispherical domed cone. It was also observed that deformation was evolved in to local from global and was formed as radial shearing of cone area beyond a threshold displacement level.

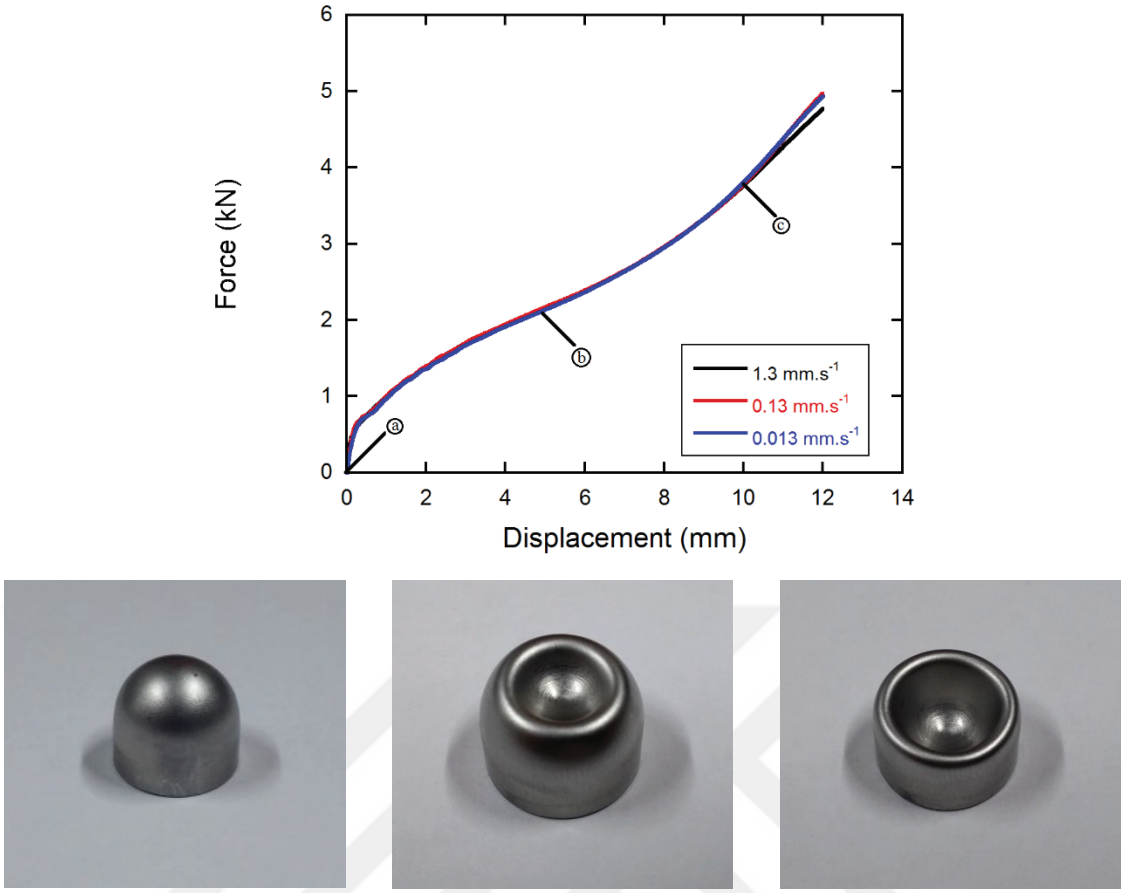

a) 0 mm b) 5 mm c) 10 mm

Figure 4.26. Force-displacement curves of R75t05 specimen and deformation progress against hemispherical tipped penetrator.

4.4. Numerical Studies on Performance Evaluation Tests

As described in previous chapters of this thesis, manufacturing method of combined geometry shells include plastic deformation of sheet metal to achieve desired shape and further resulted in thickness changes in entire specimen. Previous studies on similar geometries showed that it is obligatory to simulate deep-drawing method to mimic the effect of residual stress and strains on specimen and enhance reliability of numerical studies (Alper Tasdemirci, Kara, et al., 2015; Alper Tasdemirci, Sahin, et al., 2015). Thus, manufacturing of both geometries from sheet metal was also modeled in this thesis study.

Finite element model of deep-drawing method included 4 different parts namely as bottom mold, compression plate, blank and forming die. Critical points of deep-drawing numerical model are simulating the application of force on blank by compression plate to prevent wrinkling of edges and creating a robust contact between

forming die and blank. Force applied to blank by compression plate during real process was maintained by springs with a constant of 25.7 N/mm. In the numerical model, LOAD_RIGID_BODY card was occupied and equivalent force of 8 kN was applied by compression plate to mimic the behavior. In addition, contact of parts to blank was successfully simulated by using FORMING_ONE_WAY_SURFACE_TO_SURFACE algorithm. This contact method is typically used in simulations of metal forming and advantageous over penetration problems of rigid and deformable materials. All of the parts included in numerical simulations were represented using Belytschko-Tsay shell elements with seven integration points through the thickness. Non-deforming components of deep-drawing simulation were modeled as rigid parts and blank was modeled using MAT_SIMPLIFIED_JOHNSON_COOK with constants given in Table 4.2. As the real process was completed at very low die velocities by a hydraulic press, mass scaling was applied by reducing the density of blank and increasing the punch velocity. Numerical model of deep-drawing process is given in Figure 4.27.

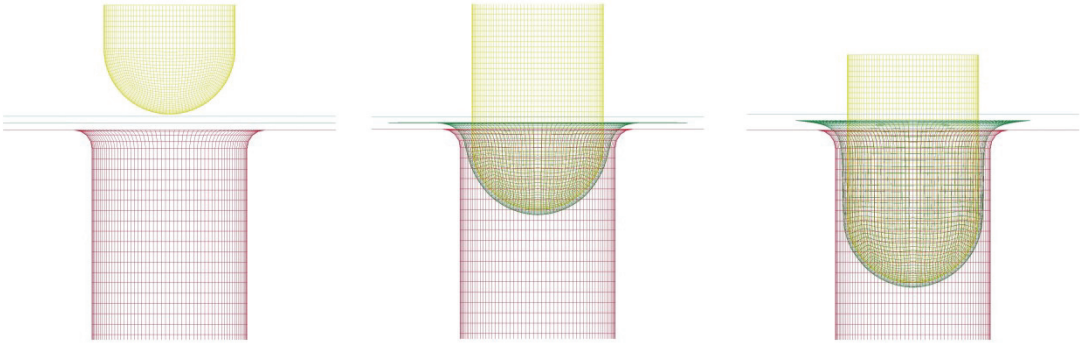

Figure 4.27. Finite element model of deep-drawing method.

FEA study was again conducted on LS-DYNA and distribution of effective plastic strain through the workpiece at the final step of numerical forming is given in Figure 4.28a. It can be seen from figure that thickness distribution tends to change throughout the entire length of specimen. Moreover, it is observed that thickness is far more reduced in hemispherical region since center point of blank is subjected to highest level of displacement, resulting in thinning due to nature of plastic deformation. Numerical thickness values were also compared with measured thicknesses and given in Figure 4.28b. Good agreement is observed between measured and numerical

thicknesses except junction point of hemispherical cap and cylindrical segment. It is presumed that usage of constant friction coefficient had led into difference in thickness levels as friction coefficient may change with change in die displacement due to lubircant film thickness.

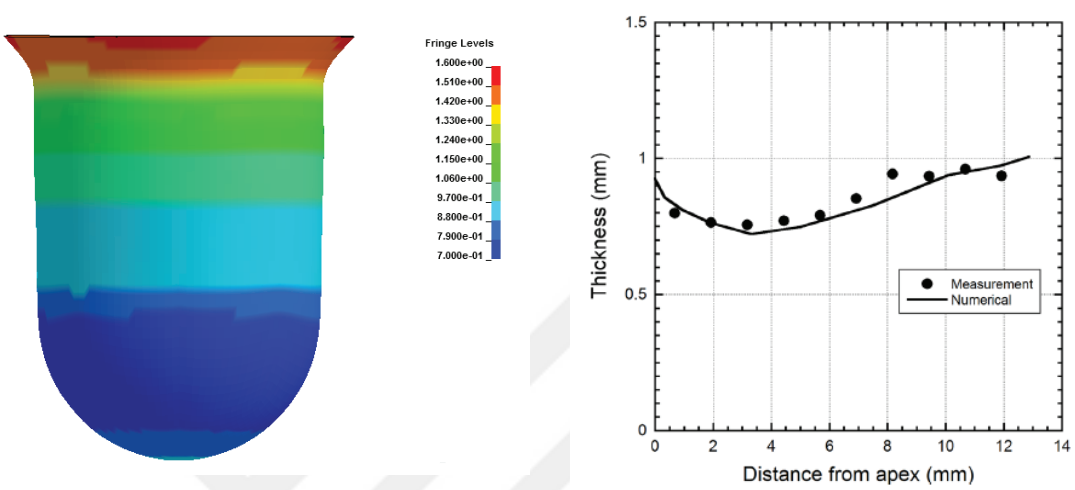

(a) (b)

Figure 4.28. (a) Thickness change of R75 t1 specimen, (b) comparison of measured and numerical thicknesses (Source: Alper Tasdemirci, Sahin, et al., 2015).

After modeling of the core manufacturing is completed, study focused on finite element modeling of quasi-static penetration behavior of hemispherical core structure against penetrators given in experimental study.

In order to model the behavior of core structure under loading, *MAT_SIMPLIFIED_JOHNSON_COOK (MAT_098) material model was used in LS-DYNA with parameters given in Table 4.2. As stated previously, manufacturing process plastically deforms blank material and operation results in residual stress and strain levels. Thus, it was assumed that combined geometry core was deformed up to a certain level and failure criterion due to effective plastic strain was determined by numerical studies. In addition, indenter and specimen holder were assumed to be non-deforming during tests and MAT_RIGID was selected to represent their behavior in numerical studies. This material model requires only fundamental mechanical properties such as density, modulus of elasticity and yield stress and hence general parameters that can be found online were used in this study.

Numerical studies included 3 main parts namely as indenter, combined geometry core and stationary specimen holder. During initial studies, benchmark study was conducted on element types of indenter and a comparison of force-displacement curves was made between the element types of eight-node solid and Belytschko-Tsay type shell. It was noted that modeling the indenter with Belytschko-Tsay shell elements resulted in nearly identical results with reduced CPU times and hence selected as indenter element type. Combined geometry shell was also modeled with Belytschko-Tsay shell elements while eight-node solid elements were occupied to model stationary specimen holder. Effect of mesh size was also investigated by conducting mesh sensitivity analyses. Results showed that average element size of 0.5 mm enables capturing the penetration behavior.

During experimental study, it was also noted that deformation mainly occurs due to displacement of indenter and no notable deformation was observed at core structure-specimen holder interface. Therefore, two different types of contact algorithms were selected to be used in FE models. Contact type ERODING_NODES_TO_SURFACE or ERODING_SINGLE_SURFACE was selected to represent the erosion induced contact between indenter and specimen while AUTOMATIC_SURFACE_TO_SURFACE was used between non-deforming core structure-specimen interfaces. SOFT 1 card in eroding contact was also occupied with static and dynamic friction coefficients of 0.15 and 0.1, respectively, while increased friction was applied in non-deforming contact with static and dynamic friction coefficient of 0.3 and 0.2, respectively. Finite element model before initiation of indenter displacement were given in Figure 4.29 for each indenter type.

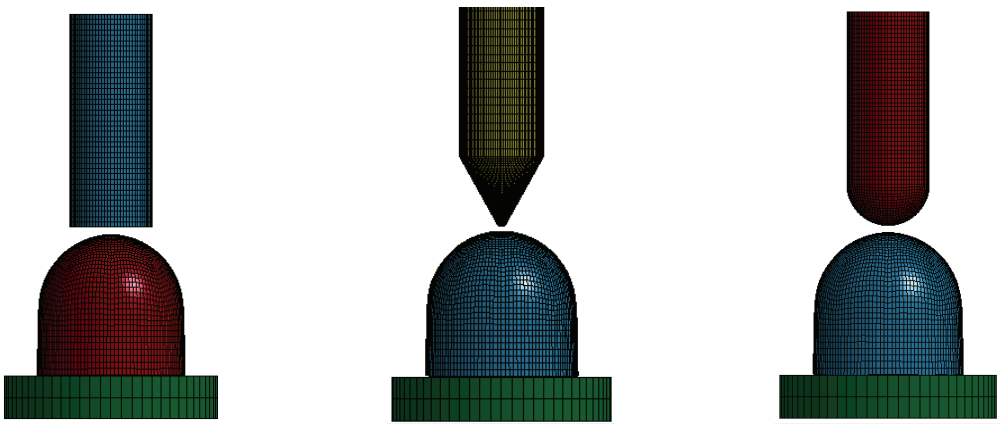

Figure 4.29. Finite element model of core structure against various types of indenters.

Numerical modeling studies on penetration tests of R75t1 core units were initiated with tests against blunt tipped indenter. Comparative results of force-displacement curves and deformation behavior with actual tests were presented in Figure 4.30 and 4.31, respectively. Force-displacement curves given in Figure 4.28 indicated that numerical model agrees well with experimental study in terms of local maximums of force and fracture displacement values. Deformation observed in performance evaluation tests was also captured with numerical study and it can be concluded that numerical model successfully mimics the behavior of R75t1 core structure against blunt tipped indenter.

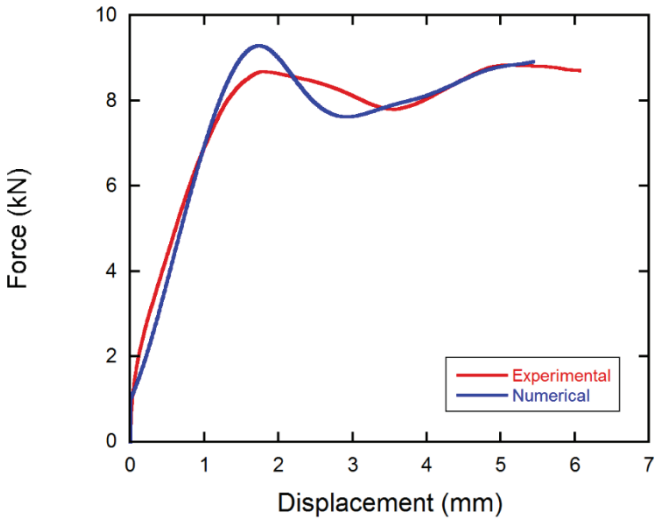

Figure 4.30. Comparison of experimental and numerical force-displacement curves of R75t1 core structure against blunt tipped indenter (1.3 $mm.s^{-1}$).

Figure 4.31. Comparison of experimental and numerical deformation of R75t1 core structure against blunt tipped indenter (1.3 $mm.s^{-1}$).

Results of quasi-static performance evaluation test of R75t1 core structure against conical tipped indenter was compared with numerical study in terms of force-displacement curves in Figure 4.32. It was observed that numerical behavior matched well with experimental force-displacement curve and general trend. Small difference noted on magnitude of local maximums was related with differences of residual stresses and strains of experimental and numerical specimens.

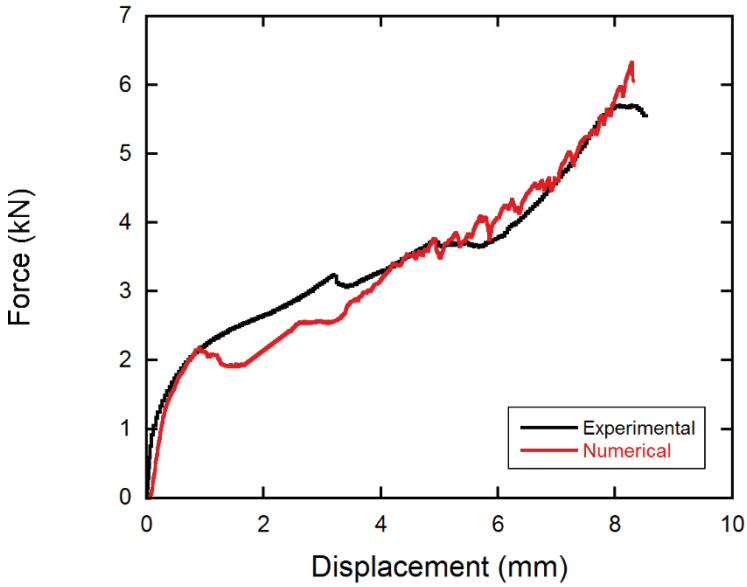

Figure 4.32. Comparison of experimental and numerical force-displacement curves of R75t1 core structure against conical tipped indenter (1.3 $mm.s^{-1}$).

Numerical studies of as-received R75t1 structure was completed by modeling of geometry against hemispherical tipped indenter and results were compared in Figure 4.33. It can be seen from figure that numerical model correlates well with experimental study and represent the behavior very well, indicating nearly coincident results with experimental study in terms of local and maximum points of forc-displacement curves. General form of deformation was also noted as inversely formed hemispherical domed cone for numerical study and coherent with test results. Sectioned numerical specimen and experimental one were given in Figure 4.34.

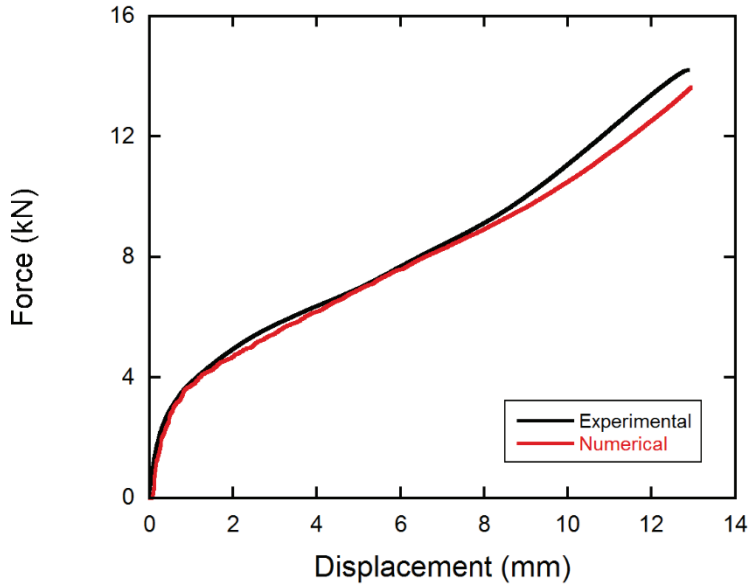

Figure 4.33. Comparison of experimental and numerical force-displacement curves of R75t1 core structure against hemispherical tipped indenter (1.3 $mm.s^{-1}$).

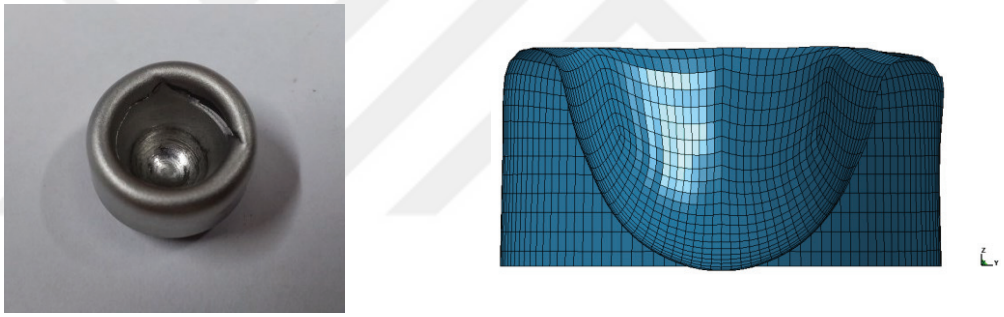

Figure 4.34. Comparison of experimental and numerical deformation of R75t1 core structure against hemispherical tipped indenter (1.3 $mm.s^{-1}$).

Results of quasi-static performance evaluation test of R75t05 core structure against blunt tipped indenter was compared with numerical study in terms of force-displacement curves and deformation behavior in Figure 4.35 and 4.36, respectively. It can be seen from Figure 4.35 that numerical study corresponds very well with experimental curve in general trend as well as local maximum and minimums of force. Deformation on core structure was found to be similar in numerical study with performance evaluation tests and indicated progressive inverse folding, as presented in Figure 4.36.

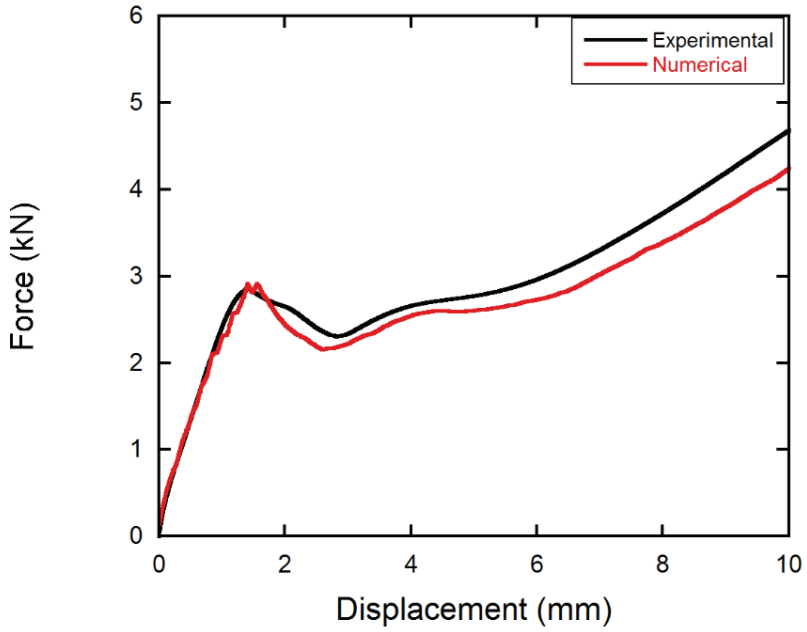

Figure 4.35. Comparison of experimental and numerical force-displacement curves of R75t05 core structure against blunt tipped indenter (0.13 mm.s^{-1}).

Figure 4.36. Comparison of experimental and numerical deformation of R75t05 core structure against blunt tipped indenter (1.3 mm.s^{-1}).

Tests of R75t05 core unit with conical tipped indenter was also modeled and numerical force-displacement curve in comparsion with experimental one was presented in Figure 4.37. Results indicate that numerical model is able to catch the experimental behavior for initial displacement levels. However, when the displacement is between 2-5.5 mm, numerical model overshoots force response of core structure. After the displacement of 5.5 mm, experimental force levels tends to be above the numerical curve, indicating difference in behavior that cannot be neglected. Aforementioned

difference can be rooted back to difference of actual and numerical thicknesses after forming operation as well as numerical instabilities.

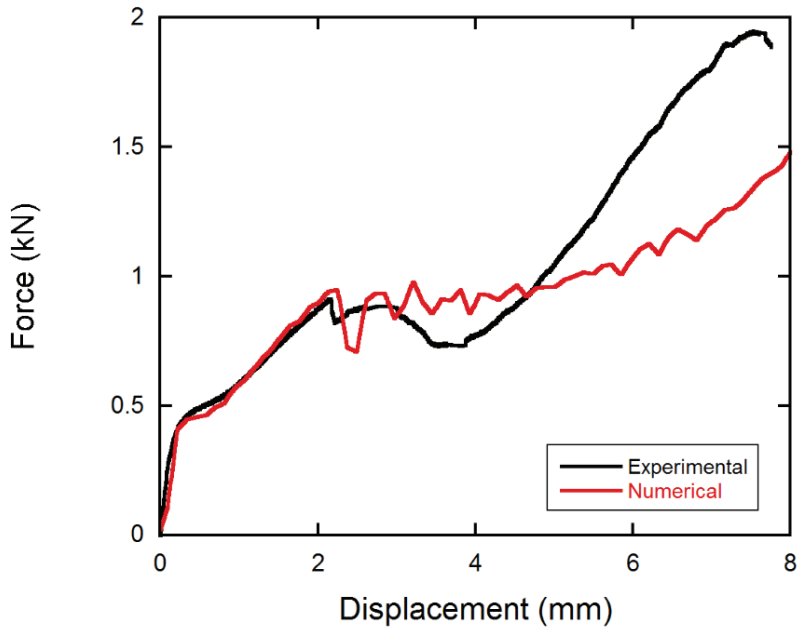

Figure 4.37. Comparison of experimental and numerical force-displacement curves of R75t05 core structure against conical tipped indenter (0.13 $mm.s^{-1}$).

Numerical studies on R75t05 core units were finalized by conducting modeling work on tests with hemispherical tipped indenter. Results given in Figure 4.38 show that model is able to mimic the experimental behavior very well by successfully capturing the critical points of bi-linear shaped force-displacement curve. Deformation of core units in both studies were found to be very similar, which was previously defined as inversely formed hemispherical domed cones. Comparison of experimentally and numerically deformed core units were presented in Figure 4.39.

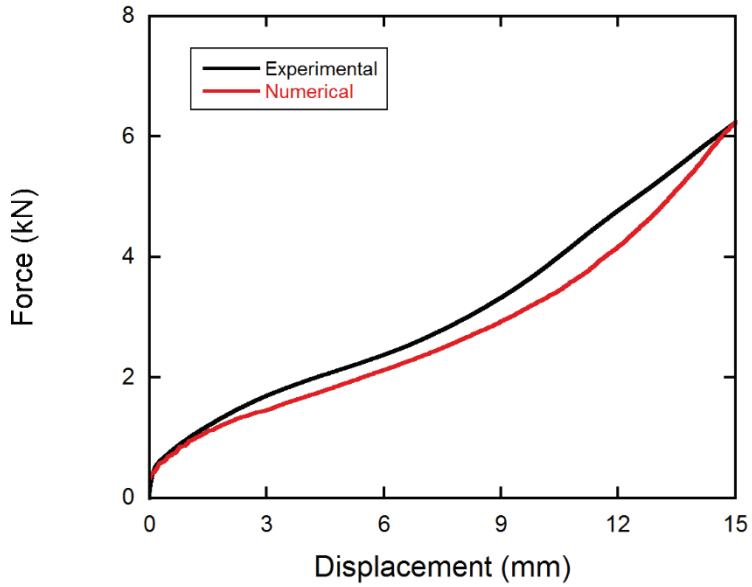

Figure 4.38. Comparison of experimental and numerical force-displacement curves of R75t05 core structure against hemispherical tipped indenter (1.3 mm.s^{-1}).

Figure 4.39. Comparison of experimental and numerical deformation of R75t05 core structure against hemispherical tipped indenter (1.3 mm.s^{-1}).

Tests conducted on intermediate velocity levels were also modeled in LS-DYNA commercially available software and successful finite element models given in previous pages were taken as a baseline. Contact algorithms previously occupied for low velocity tests were also used with constants given above. Also, material model included the constants given previously. When compared with quasi-static models, numerical studies of intermediate velocity tests included differences in velocity profile and impact mass of indenter. In order to represent the physics of weight dropping mechanism, INITIAL_VELOCITY_RIGID_BODY card was activated, which enable changing

velocity of indenter during test rather than constant velocity of indenter in models of quasi-static tests. Measured weight of indenter assembly on experimental study was added to the numerical indenter by invoking MASS_PART card.

Modeling studies of R75t1 were done on tests with blunt and conical indenters as hemispherical tipped indenter indicated problems related with misalignment and slipping to the sides of core units. Results of numerical force-displacement curves in comparison with experimental ones conducted with blunt indenter were given in Figure 4.40. As can be seen from graph that numerical curve shows good correlation with actual test result in terms of general form as well as local minimum and maximums. Also, numerical deformation around the contact zone of indenter revealed that thinning of hemispherical portion of the core unit is present due to shearing caused by increasing displacement of indenter. Figure 4.41 indicates the amount of thinning is around 0.2 mm where initial and final thicknesses were around 0.8 and 0.6 mm, respectively. Results also indicate that approach on numerical modeling of intermediate velocity tests are good and can be used in further studies.

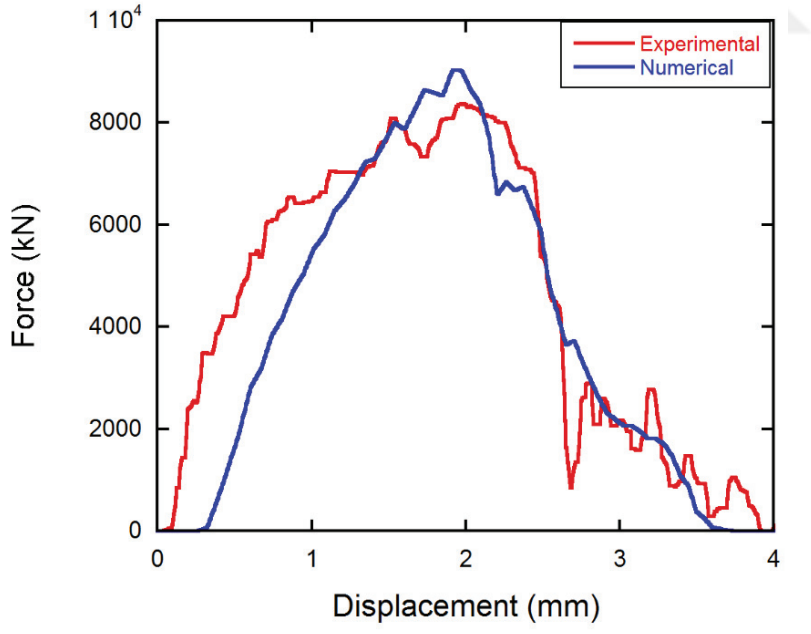

Figure 4.40. Comparison of experimental and numerical force-displacement curves of R75t1 core structure against blunt tipped indenter (3.5 $m.s^{-1}$).

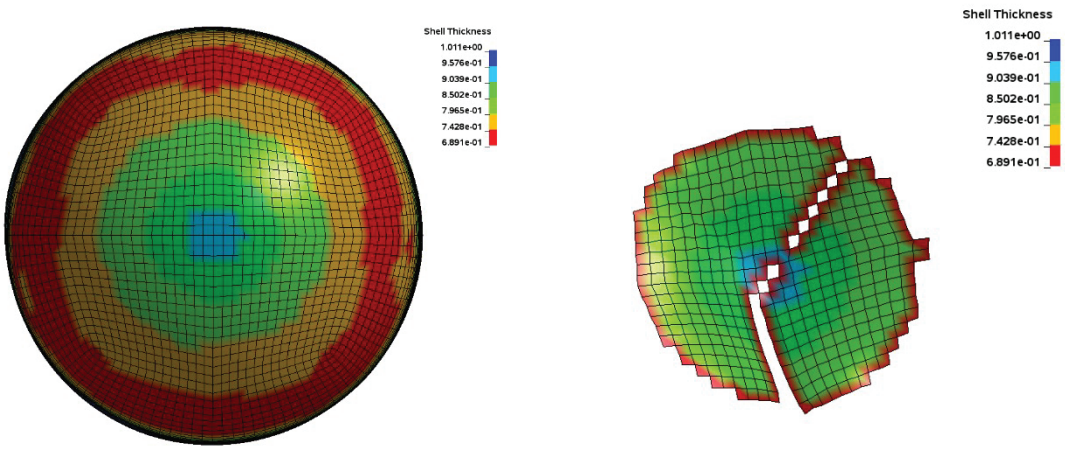

Figure 4.41. Thickness distribution of R75t1 core units in initial (on the left) and final stages of deformation.

Experimental and numerical results were compared in terms of force and energy levels and values were given in Table 4.3. In this table, P_i is initial peak force, P_m is mean force, P_{max} is maximum force, AEF is the absorbed energy up to failure and SAE is the specific absorbed energy which is termed as ratio of absorbed energy to weight of the structure. Experimental study showed that regardless of core unit thickness, a unique behavior for each indenter geometry was noted with its own characteristics which resulted in different values of local and maximum peaks. Tabulated results show that average of force and energy levels tend to change with each experimental combination. Tests on R75t05 core units indicated that highest AEF value of 39.91 kJ/kg was recorded on tests against blunt tipped indenter, followed by tests on hemispherical and conical indenters with AEF values of 30.13 and 8.05 kJ/kg, respectively. When the thickness of core geometry was increased and R75t1 core geometry was investigated, highest AEF value was noted during tests against hemispherical tipped indenter with 93.96 kJ/kg, followed by blunt and conical indenters with AEFs calculated as 46.79 kJ/kg and 26.89 kJ/kg, respecitvely. Thickness of core units also has an effect on AEF values as experimental work indicates that AEF values increase with thickness regardless of indenter type. However, with the increase of weight due to thickness increase, SAE of core units against blunt tipped indenter tends to decrease with increasing thickness. It was observed that strain rate also had a negative effect on AEF and SAE values as experimental work on R75t1 core units show that AEF and SAE decrease around 72% for tests with blunt indenter and 65% with conical indenter, with the increasing strain rate.

Table 4.3. Experimental and numerical results.

Specimen	Penetrator Type	Test Type	Result	P_i (kN)	P_m (kN)	P_{max} (kN)	AEF (J)	SAE (kJ/kg)
R75t05	Blunt	Quasi-static	Exp.	2.86	3.30	5.63	39.9	20.78
			Num.	2.92	2.97	4.91	36.4	19.05
R75t05	Conical	Quasi-static	Exp.	0.91	1.04	1.94	8.05	4.19
			Num.	0.94	0.98	1.75	8.74	4.55
R75t05	Hemisphere	Quasi-static	Exp.	0.61	2.51	4.77	30.1	15.69
			Num.	0.66	2.21	4.18	26.5	13.83
R75t05	Blunt	Drop weight	Exp.	2.87	2.62	3.95	31.6	16.47
			Num.	2.81	2.91	4.16	33.7	17.55
R75t05	Conical	Drop weight	Exp.	0.80	1.04	1.85	9.02	4.69
			Num.	0.76	1.03	1.89	9.03	4.70
R75t1	Blunt	Quasi-static	Exp.	8.68	7.84	8.83	46.7	13.60
			Num.	9.29	7.73	9.29	47.3	13.76
R75t1	Conical	Quasi-static	Exp.	3.23	3.35	5.68	26.8	7.81
			Num.	2.18	3.32	5.81	25.6	7.45
R75t1	Hemisphere	Quasi-static	Exp.	4.82	7.83	13.3	93.9	27.32
			Num.	4.32	7.61	12.6	91.3	26.56
R75t1	Blunt	Drop weight	Exp.	6.21	5.17	8.24	17.8	5.18
			Num.	8.02	5.51	9.01	15.7	4.56
R75t1	Conical	Drop weight	Exp.	2.8	3.15	5.25	9.29	2.70
			Num.	2.05	4.07	5.18	12.1	3.51

4.5. Strain Rate and Micro-inertia Effects

Crushing behavior, which is represented in load-displacement curve, defines the classification of energy absorbing structures as Type I and TYPE II (C. R. Calladine & English, 1984; Tam & Calladine, 1991; Zhang & Yu, 1989). Load-displacement curves with a relatively flat-topped form is classified as Type I whereas load-displacement curves with steep declines are termed as Type II. Previous studies indicate that, with the inertia and strain rate changes, behavior of Type II structures is affected more when compared to Type I and their energy absorption capability is increased with the strain rate sensitivity of base material (C. R. Calladine & English, 1984; Tam & Calladine,

1991; Zhang & Yu, 1989). As the investigated core structure includes both Type I (hemispherical segment) and Type II (cylindrical segment) portions, effect of the inertia and strain rate must be numerically investigated by conducting additional FEA work at increased penetrator velocities. Effect of strain rate is defined by the difference of force-displacement behavior under quasi-static and high velocity penetration while effect of micro-inertia is investigated under high velocity penetration by setting the strain rate parameter on and off for deforming structure's material model.

In order to investigate the aforementioned effects, finite element models of R75t1 structure against hemispherical tipped indenter were taken as case study. Strain rate and micro-inertia effects were investigated by increasing the indenter velocity to 300 m.s-[1] and setting the strain rate parameter 0.067 and 0 for Johnson-Cook material model. Comparison of force-displacement curves for strain rate and micro-inertia effects were given in Figure 4.42. As depicted in graph, core unit has indicated both micro-inertia and strain rate effects while change in behavior due to increased strain rate is found to be much higher. At initial displacement values, behavior is found to be common for models with increased indenter velocities. However, force-displacement curves become distinct when displacement is beyond 3 mm and strain rate effects were found to be more dominant when compared with the quasi-static model.

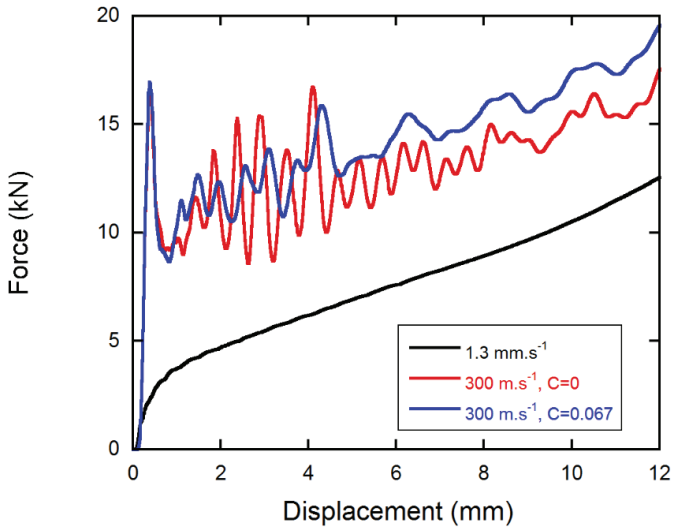

Figure 4.42. Effect of strain rate and inertia on behavior of R75t1 core units.

Strain rate and micro-inertia effects were also investigated on R75t05 core structure against hemispherical tipped indenter and results were given in Figure 4.43. Again, indenter velocity was selected as 300 $m.s^{-1}$ to include the effect of strain rate and strain rate parameter was set as on and off to investigate the change in behavior due to micro-inertia effects. It can be seen from figure that behavior of core structure is mainly changed due to strain rate whereas strain rate effects were noted to be dominant beyond displacement levels of 5 mm.

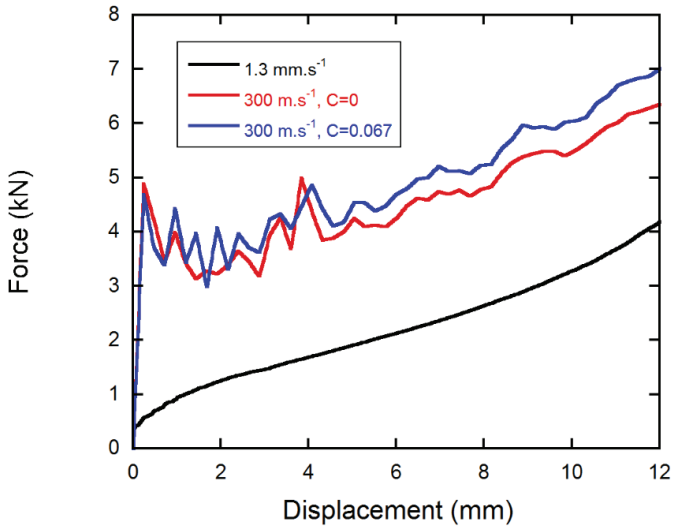

Figure 4.43. Effect of strain rate and inertia on behavior of R75t05 core units.

CHAPTER 5

EXPERIMENTAL AND NUMERICAL INVESTIGATION OF EFFECT OF HEAT TREATMENT ON PENETRATION BEHAVIOR

Core geometry investigated in this thesis was manufactured by using deep-drawing method which results in residual stresses and strains on various levels. It is known from previous studies that heat-treatment operations conducted on such structures relieve the stresses and strains caused by manufacturing method and hence may have an effect on penetration behavior of structure (Alper Tasdemirci, Kara, Turan, Sahin, & Guden, 2016). This chapter of the study investigates the effect of heat treatment on penetration behavior of target core structure.

5.1. Heat Treatment of Core Structures

Before the study was initiated, main parameters on investigation of effect of heat treatment on penetration behavior of core structure were defined as steps of heat treatment operation to be applied, test conditions and testing equipment to be used in experimental study.

Previous study on a similar structure also applied heat treatment to investigate the effects on blast response (Alper Tasdemirci et al., 2016). Study concluded that, conducting a heat treatment operation at a specific temperature with a duration of 2 hours results in a microstructure which is ductile yet strong and is mostly favored in applications where impact energy absorption is required. Thus, heat treatment operation conducted on core structures followed the same methodology applied by Tasdemirci et. al, which includes heating of the specimens up to 1100 °C and were held at that temperature for 2 hours, followed by immediate air quenching at room temperature. In this procedure, temperature level was selected to reach fully austenitic structure and duration of stable temperature was chosen as 2 hours since it was reported that there is no significant change on behavior on longer durations (Alper Tasdemirci et al., 2016). Heat treatment was conducted using an electric furnace and image of specimens before

and after operation were given in Figure 5.1, with heat treated core structure given on the right.

Figure 5.1. Specimens before and after heat treatment operation.

In order to set a correct basis and achieve a successful comparison with previous experimental results, tests were conducted at same penetrator velocity levels with as-received core structures and same testing equipment was used. Comparison of test results are presented in next sections.

5.2. Performance Evaluation Tests of Heat Treated Core Structure

After specimen preparation was completed, performance evaluation tests were conducted on both geometries at quasi-static strain rates. Experimental study was initiated with tests of R75t1 core geometry against blunt tipped indenter at penetrator velocities of 0.013, 0.13 and 1.3 $mm.s^{-1}$ and results were given in Figure 5.2. It was noted from experimental results that heat-treated core structure first exhibits a linear region which ends around a displacement level of 2 mm. Beyond that point, a plateau region was observed which was followed by densification of material and tests were stopped when displacement crossed 12 mm. It can also be seen from figure that heat treated R75t1 core structure does not indicate a velocity dependent behavior against blunt tipped indenter.

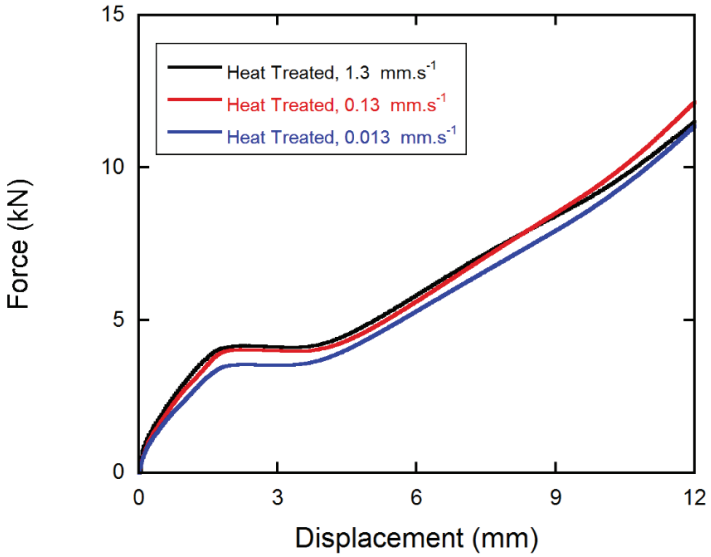

Figure 5.2. Comparison of test results of heat treated R75t1 structure against blunt tipped indenter.

Heat treated R75t1 core structure was also tested against conical tipped indenter at low strain rates and results were presented in Figure 5.3. Experimental results showed that structure indicated a steep linear region which was related with initial localized deformation on hemispherical cap of geometry. After that, densification was observed as main deformation mode and experimental study also indicated that behavior of heat treated R75t1 structure against conical tipped indenter is independent from penetrator velocity in current velocity levels and variation in results are in negligible order.

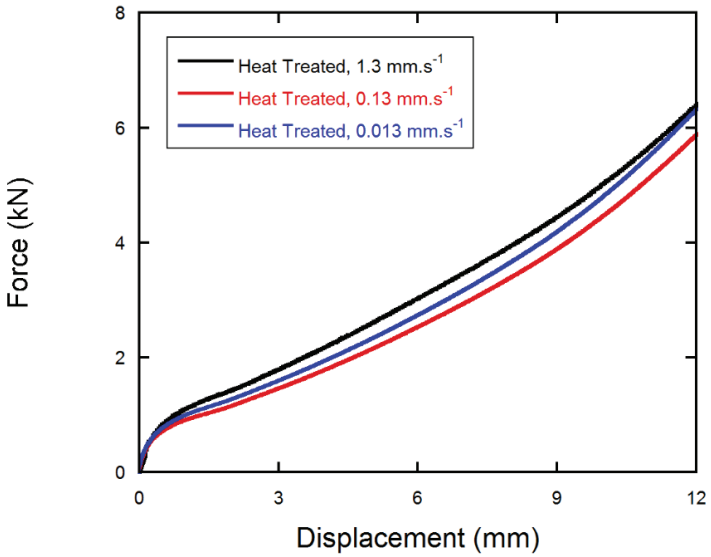

Figure 5.3. Comparison of test results of heat treated R75t1 structure against conical tipped indenter.

Performance evaluation tests of heat treated R75t1 core structure was completed by conducting quasi-static tests against hemispherical tipped indenter and results were given in Figure 5.4. It can be seen from test results that heat-treated core structure first indicated a linear region which was followed by densification region with increasing slope. It was noted that structure did not exhibited a penetrator velocity dependent behavior and thus, further tests at the lowest penetrator velocity of 0.013 $mm.s^{-1}$ were not conducted.

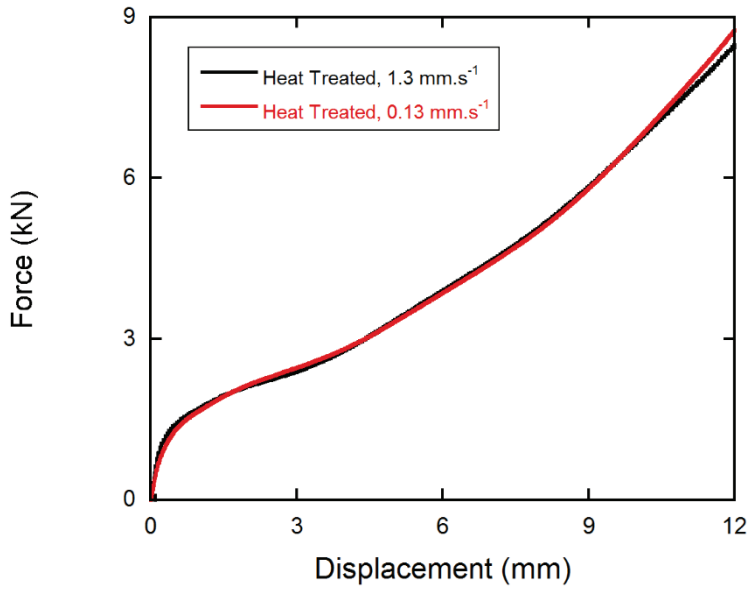

Figure 5.4. Comparison of test results of heat treated R75t1 structure against hemisphere tipped indenter.

Effect of heat treatment on penetration behavior was also investigated on R75t05 core structure. Performance evaluation tests were initiated by conducting quasi-static tests against blunt tipped indenter and results were presented in Figure 5.5. It was noted from results that structure indicated a linear region with a local maximum of 1.25 kN around a displacement of 1.2 mm. Beyond that point, indenter progressively deformed hemispherical and cylindrical portions, respectively and force-displacement behavior was also noted as independent from penetrator velocity on heat treated R75t05 core structure as the experimental results at different velocity levels were found to be nearly coincident.

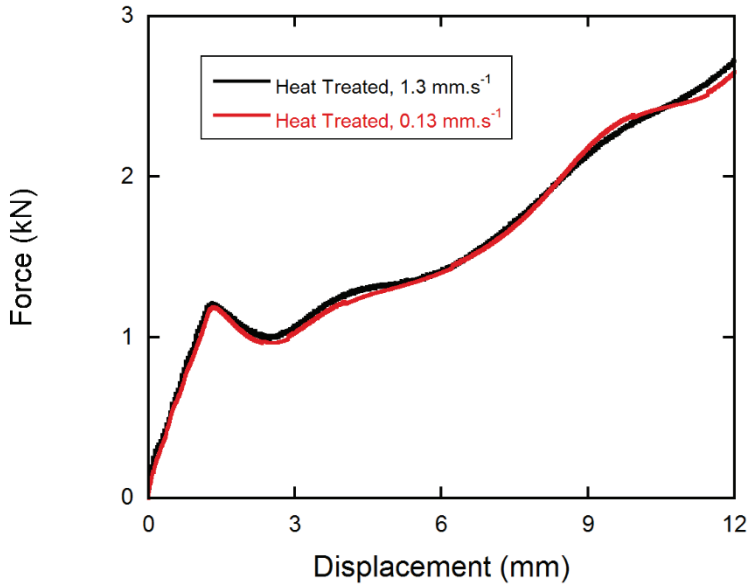

Figure 5.5. Comparison of test results of heat treated R75t05 structure against blunt tipped indenter.

Heat treated R75t05 core structure was also tested against conical tipped indenter at quasi-static strain rates and results were given in Figure 5.6. Core structure indicated bilinear force-displacement curve which included a steeper linear region followed by densification area with decreased slope. Test results also indicated that behavior was independent from change in penetrator velocity.

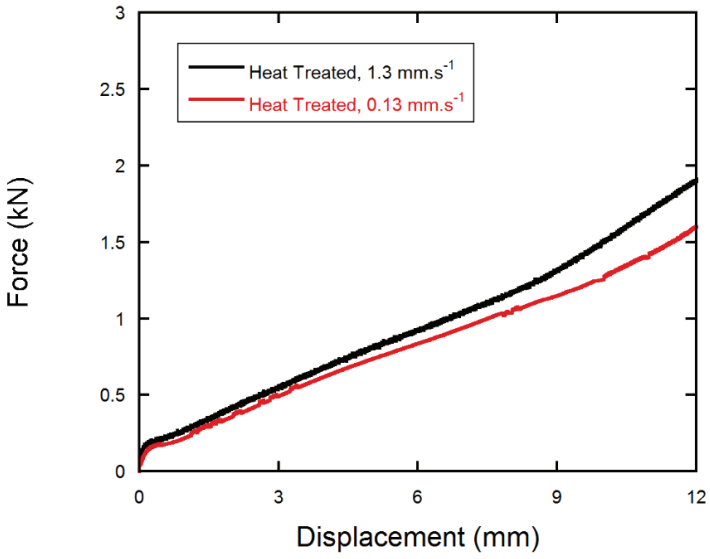

Figure 5.6. Comparison of test results of heat treated R75t05 structure against conical tipped indenter.

Performance evaluation tests of heat treated R75t05 core structure was completed by conducting tests against hemisphere tipped indenter at quasi-static strain rates. It can be noted from results that bilinear behavior was observed and experimental results indicated that behavior of core structure was not changing with penetrator velocity and hence, further tests at lowest cross-head velocity (0.013 $mm.s^{-1}$) were not conducted. Comparison of force-displacement curves of heat treated R75t05 core structure against hemispherical tipped indenter was given in Figure 5.7.

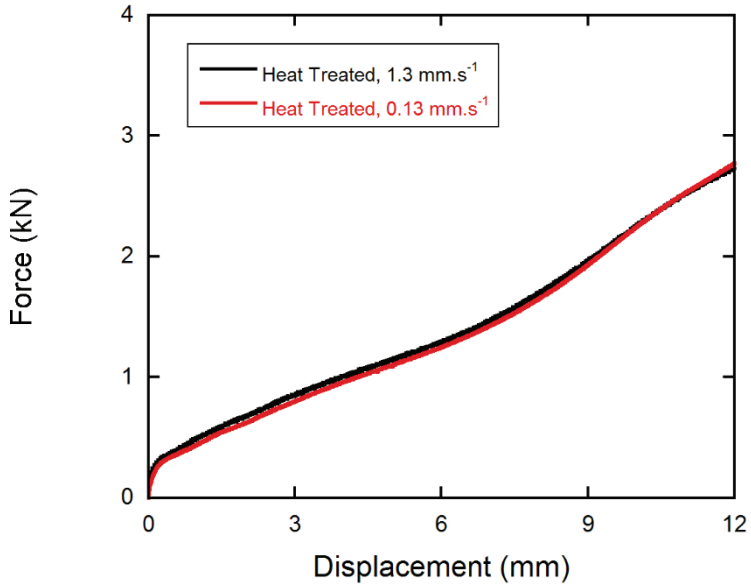

Figure 5.7. Comparison of test results of heat treated R75t05 structure against hemisphere tipped indenter.

Results of performance evaluation tests of as-received (AR) and heat treated (HT) core structures were compared in terms of fracture displacement, fracture force, mean force, total absorbed energy and specific absorbed energy (SAE) against constant indenter velocity of 0.13 $mm.s^{-1}$. Tabulated results in Table 5.1 indicated that highest fracture force was noted in tests of heat treated R75t1 core structure against hemispherical tipped indenter while highest fracture displacement was observed in tests of heat treated R75t1 core structure against conical tipped indenter. Experimental study also indicated that increase of thickness resulted in an increase in fracture force of both as-received and heat-treated core structures. It can be seen from results that, in each core structure type, total absorbed energy up to fracture was found to be lowest in tests against conical tipped indenter since more localized deformation altered the general trend of force-displacement curve. In contrast, more globalized deformation observed

during tests of hemispherical tipped indenter resulted in highest absorbed energy levels in each core structure. Comparative results from experimental study also showed that heat treatment operation mostly increased the fracture displacement. It is believed that reducing the level of residual stresses and strains due to manufacturing has led into softening of structure and behavior which was similar to inverse forming of geometry was observed. Specific absorbed energy (SAE), which is defined as ratio of absorbed energy to weight, of each type of core structure was also calculated and given in Table 5.1. It was observed from experimental results that highest SAE values were recorded in tests of as received R75t05 core structure against blunt tipped indenter and heat treated R75t1 core structure against conical and hemispherical tipped indenters, respectively. Results of SAE values indicated that heat treated R75t1 core structure performed better than alternatives tested in this study.

Table 5.1. Comparison of performance evaluation tests' results of as-received and heat treated core structures.

Specimen	**Indenter**	**Displacement (mm)**	**Force (Mean, kN)**	**Force (Max, kN)**	**Energy (J)**	**SAE (kJ/kg)**
R75t05 AR	Blunt	12	3.30	5.63	39.91	20.78
R75t05 AR	Conical	7.75	1.04	1.94	8.05	4.19
R75t05 AR	Hemisphere	12	2.51	4.77	30.13	15.69
R75t05 HT	Blunt	12	1.56	2.65	18.81	9.79
R75t05 HT	Conical	12	0.83	1.61	9.98	5.19
R75t05 HT	Hemisphere	12	1.37	2.77	16.45	8.56
R75t1 AR	Blunt	6.2	7.84	8.83	46.79	13.60
R75t1 AR	Conical	8	3.35	5.68	26.89	7.81
R75t1 AR	Hemisphere	12	7.83	13.39	93.96	27.32
R75t1 HT	Blunt	12	6.21	12.13	74.36	21.61
R75t1 HT	Conical	12	2.74	5.88	32.98	9.58
R75t1 HT	Hemisphere	12	4.21	8.76	50.61	14.71

5.3. Numerical Studies on Performance Evaluation Tests of Heat Treated Core Structure

As stated on previous chapters, numerical deep drawing operation successfully imitated the thickness distribution on core structure and was used in modeling studies of performance evaluation tests of as-received core structure. In order to mimic the effects of heat treatment numerically, it is required to remove the residual stresses and strains caused by deep drawing. This was achieved by deleting the nodal and elemental histories of core structures on *INITIAL card of LS-DYNA (Alper Tasdemirci et al., 2016).

Core structure was modeled using MAT_JOHNSON_COOK material model with constants given previously (Alper Tasdemirci, Sahin, et al., 2015). As the indenter and specimen fixture was not deformed, MAT_RIGID material model was used to model their behavior. Deforming contact algorithm was created between indenter and core structure while non-deforming contact between core structure and specimen fixture was ensured using AUTOMATIC_SURFACE_TO_SURFACE contact algorithm. Friction coefficients in both types of contacts were selected as 0.4 for static and 0.3 for dynamic contacts, respectively.

Modeling of penetration behavior of heat treated core structure was initiated by numerical studies of R75t05 core geometry against blunt tipped indenter at indenter velocity of 1.3 $mm.s^{-1}$. Study was based on numerical model of as-received structure at same testing conditions and residual stresses and strains on core structure were deleted to mimic the effect of heat treatment. Comparison of experimental and numerical force-displacement curves given in Figure 5.8 showed very good correlation of experimental and numerical work which further indicated that proposed method is the correct approach to model the penetration behavior of heat treated core structures. In addition to study conducted on R75t05 core units, behavior of heat treated R75t1 core units was modeled and results were presented in Figure 5.9. For this study, tests conducted with hemispherical tipped indenter at the cross-head velocity of 0.13 $mm.s^{-1}$ were taken to observe the capability of the modeling approach under different core unit thickness, indenter type and velocity, respectively. Results show that methodology applied previously in modeling of heat treated core units of R75t05 is also able to mimic the penetration behavior of R75t1 structure very well. Force-displacement curve indicates a

successful example of bi-linear behavior as noted in experimental work with local maximum and minimums nearly coincident with test results.

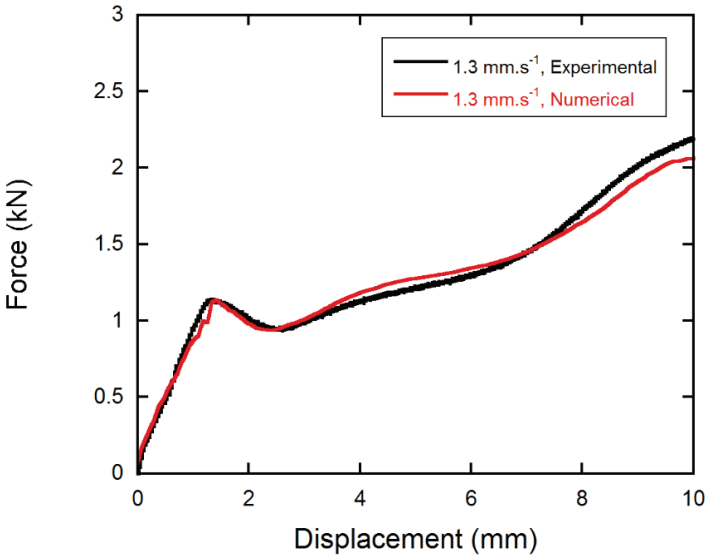

Figure 5.8. Comparison of experimental and numerical force-displacement curves of heat treated R75t05 core structure against blunt tipped indenter (1.3 $mm.s^{-1}$).

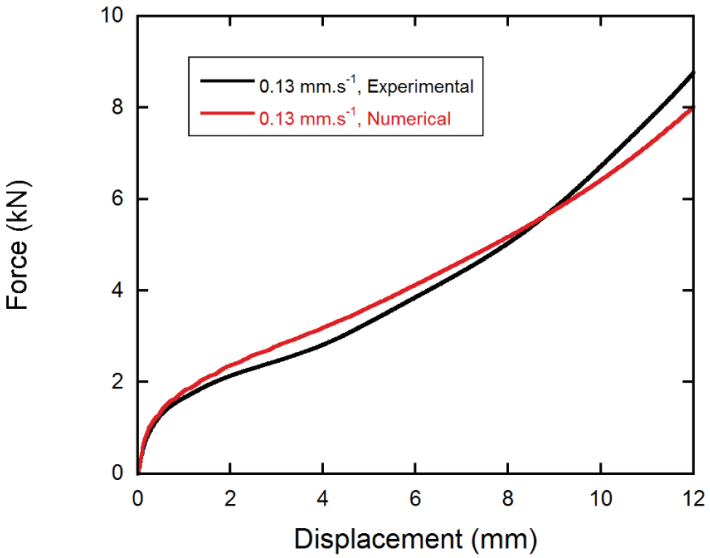

Figure 5.9. Comparison of experimental and numerical force-displacement curves of heat treated R75t1 core structure against hemispherical tipped indenter (0.13 $mm.s^{-1}$).

CHAPTER 6

INVESTIGATION OF EFFECT OF CONFINEMENT ON PENETRATION BEHAVIOR

Experimental study given in this chapter includes investigation of effect of confinement on core structure. For this purpose, experimental study conducted on single core element was repeated but specimens were radially confined using a special fixture. Comparative results were given in following subsections.

6.1. Materials and Method

Experimental study of this chapter was initiated with defining the testing procedure. As the aim of the study was to investigate whether radial confinement has an effect on penetration behavior, experimental methodology followed the testing procedure used during performance evaluation tests of single core structure in order to compare the results regardless of test method. Same indenters and testing equipment which was used during previous experimental study was occupied. As an addition, confinement of core structure was achieved by using the previously designed face of specimen fixture; investigated specimen was positioned at the center and was surrounded by non-deforming core units, realizing the physical condition of deformation of single core structure in a fully confined environment. Technical drawing of specimen fixture and image taken before confinement tests are given in Figure 6.1.

Figure 6.1. Specimen fixture used in experimental study and actual image captured before tests.

6.2. Performance Evaluation Tests of Radially Confined Core Units

Performance evaluation tests were conducted on core structures to investigate the effect of confinement against blunt, conical and hemispherical tipped indenters. During experimental study, 0.13 $mm.s^{-1}$ was selected as reference indenter velocity and comparative Force-Displacement curves with unconfined tests' results were created. In addition to as-received core structure, heat treated specimens were also tested. Each specimen group included average of three tests' results and were presented in this subsection.

Investigation of effect of confinement was initiated with performance evaluation tests of as-received R75t1 structure against blunt tipped indenter and results are given in Figure 6.2. It can be seen from figure that confinement does not have an effect against blunt tipped indenter; force-displacement curves are very close in terms of local maximums and minimums as well as general trend. Final form of deformation was found to be plugging for both types of tests.

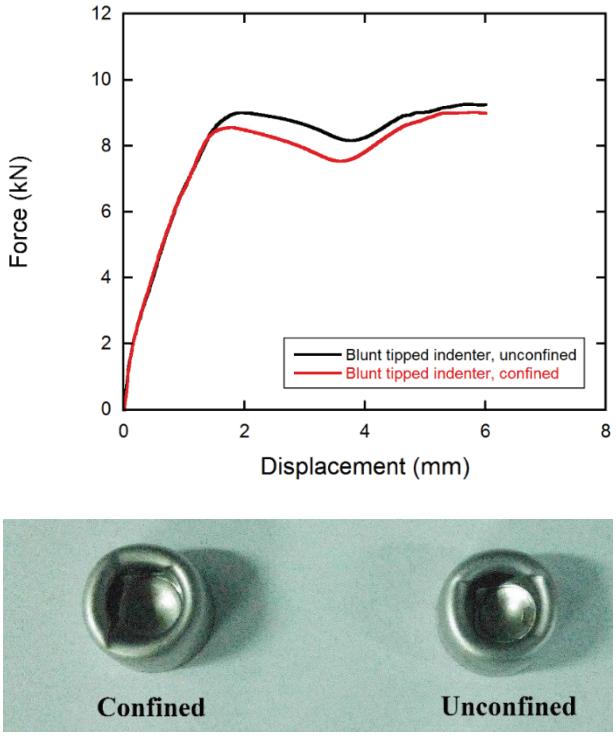

Figure 6.2. Comparison of test results and deformed specimens with confined and unconfined states (R75t1 core units against blunt tipped indenter).

Experimental study was continued with confined tests of as-received R75t1 structure against conical tipped indenter. It is evident from force-displacement curves that penetration behavior was affected from confinement and trend of curve was changed drastically. Maximum point of force was noted to be shifted to lower displacement values and second local maximum point was formed around a displacement level of 9 mm. Full fracture occurred around a force level of 5.5 kN and symmetrical tearing was observed as failure mode for both types of tests. Results of confined and unconfined tests were given in Figure 6.3.

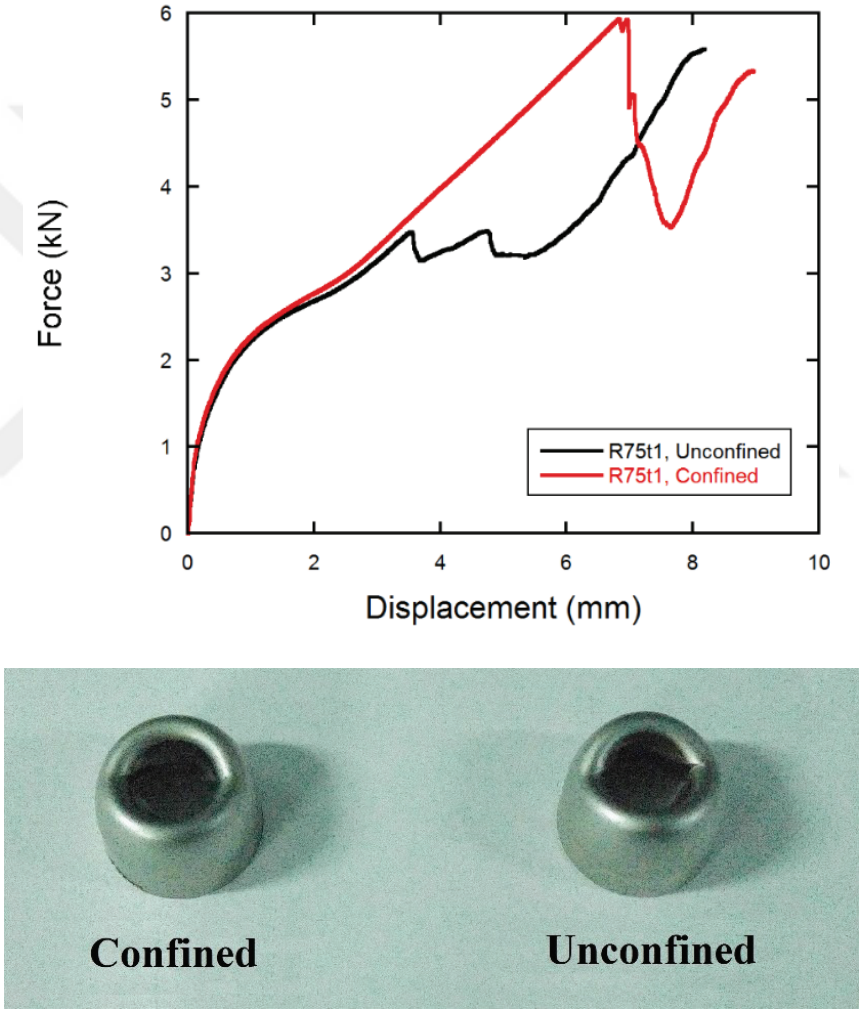

Figure 6.3. Comparison of test results and deformed specimens with confined and unconfined states (R75t1 core units against conical tipped indenter).

As-received R75t1 core structure was also tested against hemispherical tipped indenter at an average indenter velocity of 0.13 $mm.s^{-1}$ and comparison of force-displacement curves were given in Figure 6.4. It was noted from figure that confinement

has no effect on penetration behavior of structure against hemispherical tipped indenter as the both experimental curves fell nearly coincident. Tests were finished around a displacement level of 12 mm and radial tearing of inversely formed conical dome was observed on both confined and unconfined core structures.

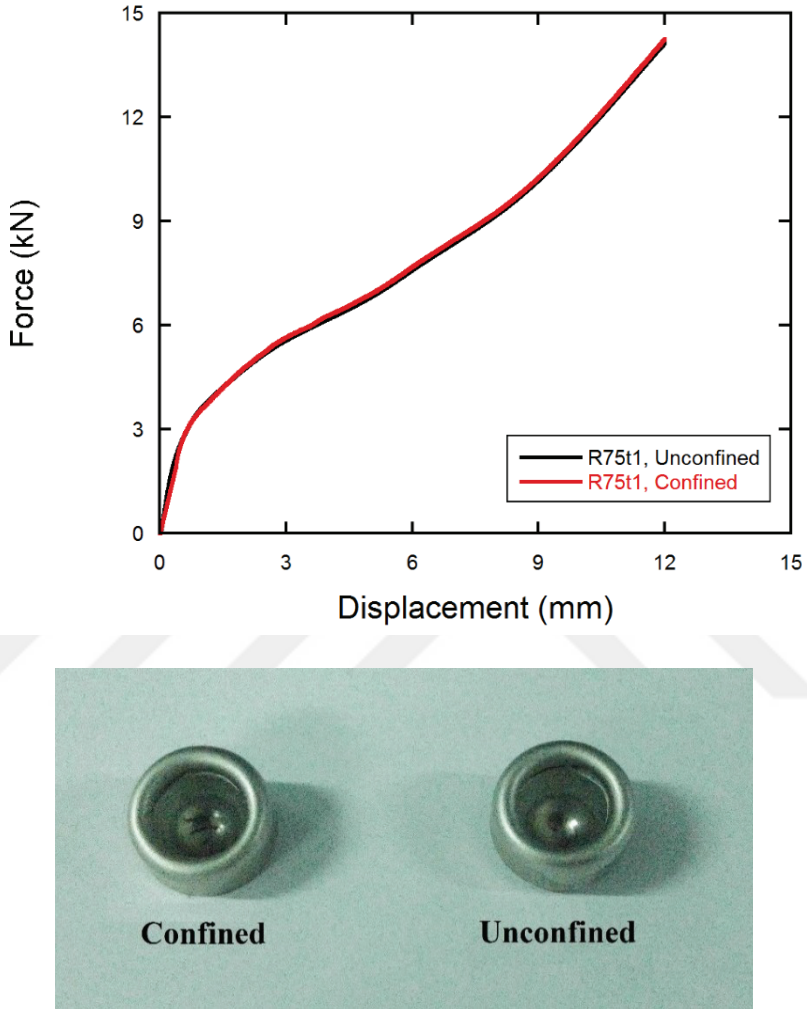

Figure 6.4. Comparison of test results and deformed specimens with confined and unconfined states (R75t1 core units against hemisphere tipped indenter).

Heat treated state of R75t1 core structure was subjected confined performance evaluation tests and comparative force-displacement curves of confined and unconfined core structure against blunt tipped indenter is given in Figure 6.5. A negligible difference was observed on general trend of curves and minor increase in maximum value of force was noted due to confinement. Final form of deformation was found to be plugging after both types of test and formation of hexagon shape was noted on outer

shell of core structure due to interaction of core unit with confining elements. Image taken after both tests were also given in Figure 6.5.

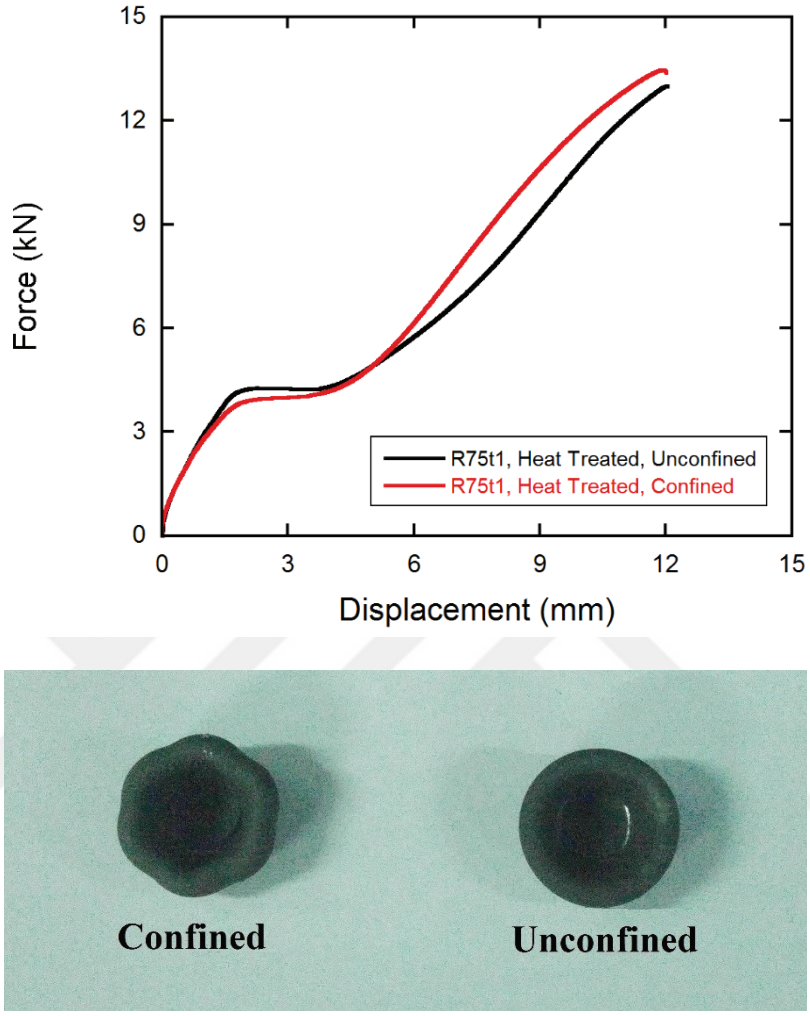

Figure 6.5. Comparison of test results and deformed specimens with confined and unconfined states (heat treated R75t1 core units against blunt tipped indenter).

Heat treated R75t1 core structure was also tested against conical tipped indenter and comparison of results against unconfined tests are given in Figure 6.6. It is evident from graph that confinement does not have an effect on penetration behavior of structure as the force-displacement curves are nearly identical which shows force of 6 kN was reached at the displacement of 12 mm. Structure was failed indicating radial tearing as dominant deformation mode for unconfined structure while confined structure indicated radial and symmetrical tearing. Final form of deformation for both structures was also given in Figure 6.6.

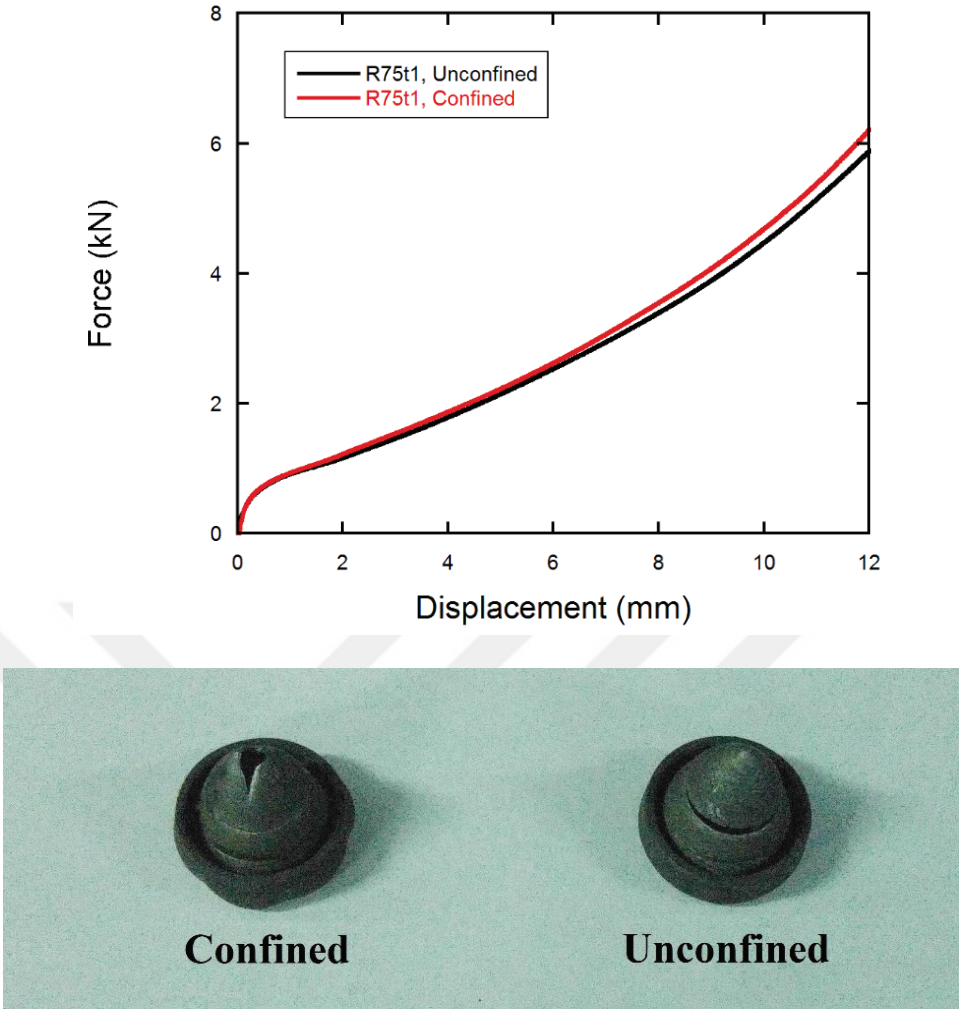

Figure 6.6. Comparison of test results and deformed specimens with confined and unconfined states (heat treated R75t1 core units against conical tipped indenter).

Heat treated and radially confined R75t1 structure was finally tested against hemispherical tipped indenter and force-displacement curves of single and confined structure was given in Figure 6.7. It was concluded that effect of confinement on structure is negligible and small difference may be correlated with structure's deviation originating from manufacturing method. Force levels of 9.6 kN were reached on displacement of 12 mm and final form of deformation was noted as radial tearing of hemisphere domed inverse cone, as given in Figure 6.7.

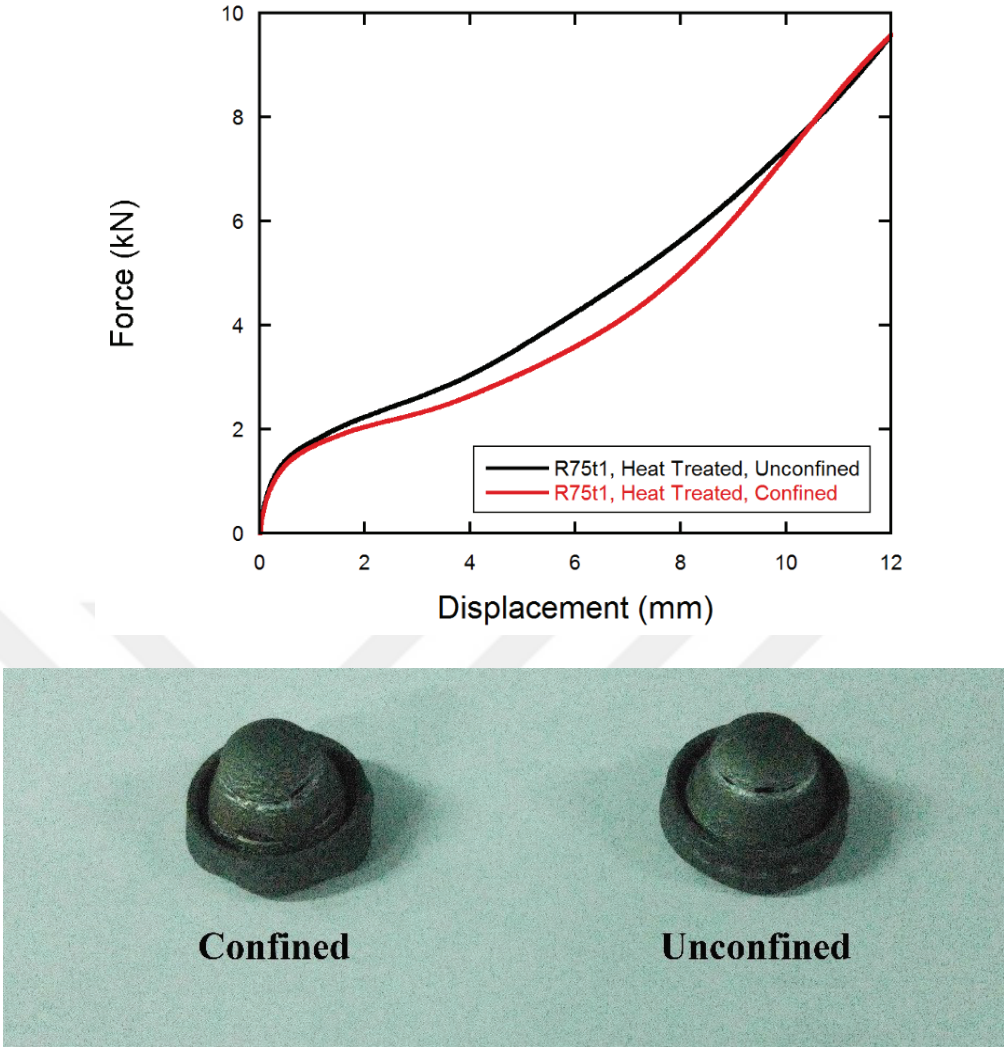

Figure 6.7. Comparison of test results and deformed specimens with confined and unconfined states (heat treated R75t1 core units against hemispherical tipped indenter).

Radially confined R75t05 core structure was also tested against blunt tipped indenter and force-displacement curves of confined and unconfined specimens were given in Figure 6.8. It was observed from figure that both experimental curves are identical in terms of general trend and local maximum-minimum points which indicate that confinement does not have an effect on penetration behavior of R75t05 structure. Inversely formed cone with plug formation was noted in both confinement conditions and nearly identical form of post-test specimens also confirms the comment above.

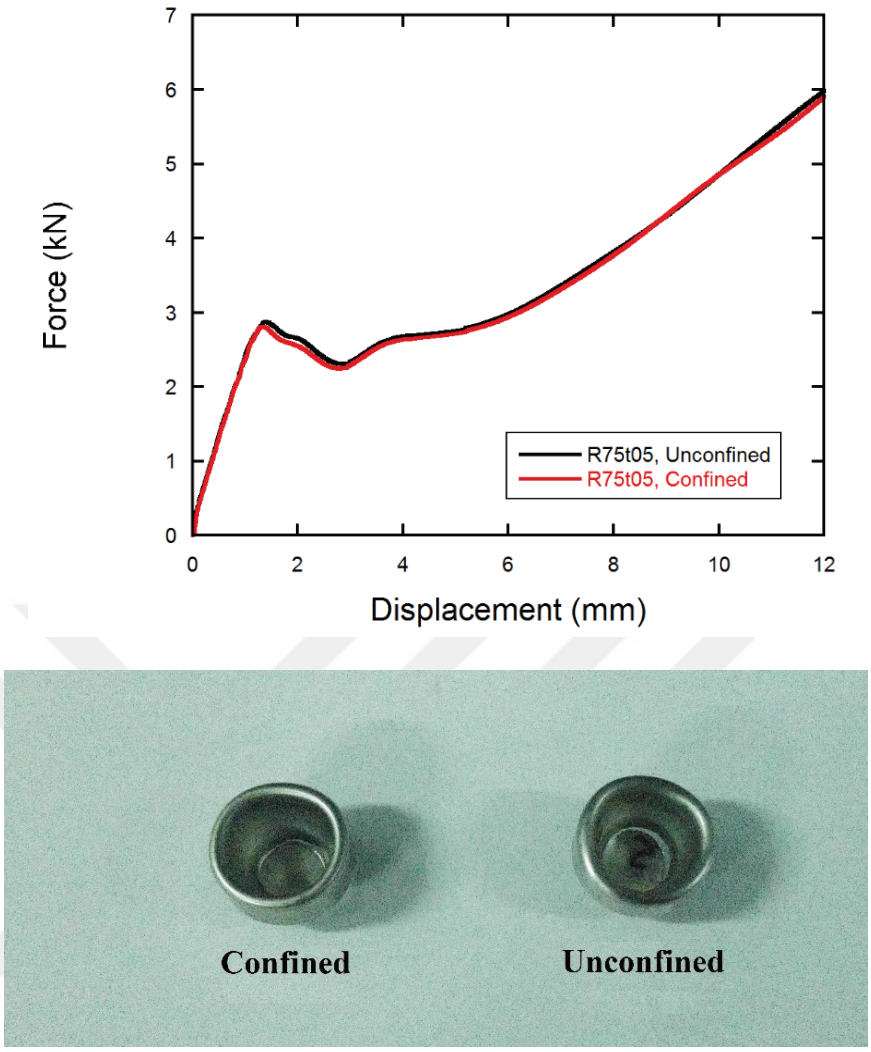

Figure 6.8. Comparison of test results and deformed specimens with confined and unconfined states (R75t05 core units against blunt tipped indenter).

As-received R75t05 core structure in radial confinement was tested against conical tipped indenter and results were compared with unconfined tests' results in Figure 6.9. both of the tests indicated a local maximum followed by a slight decrease in force with increase in displacement. As explained in previous chapters, this sudden decrease is related with initiation of tearing of hemispherical dome of core structure and was followed by densification of structure. Force-displacement curves of confined and unconfined tests tend to be similar and deformation was noted as symmetrical tearing, as given in Figure 6.9.

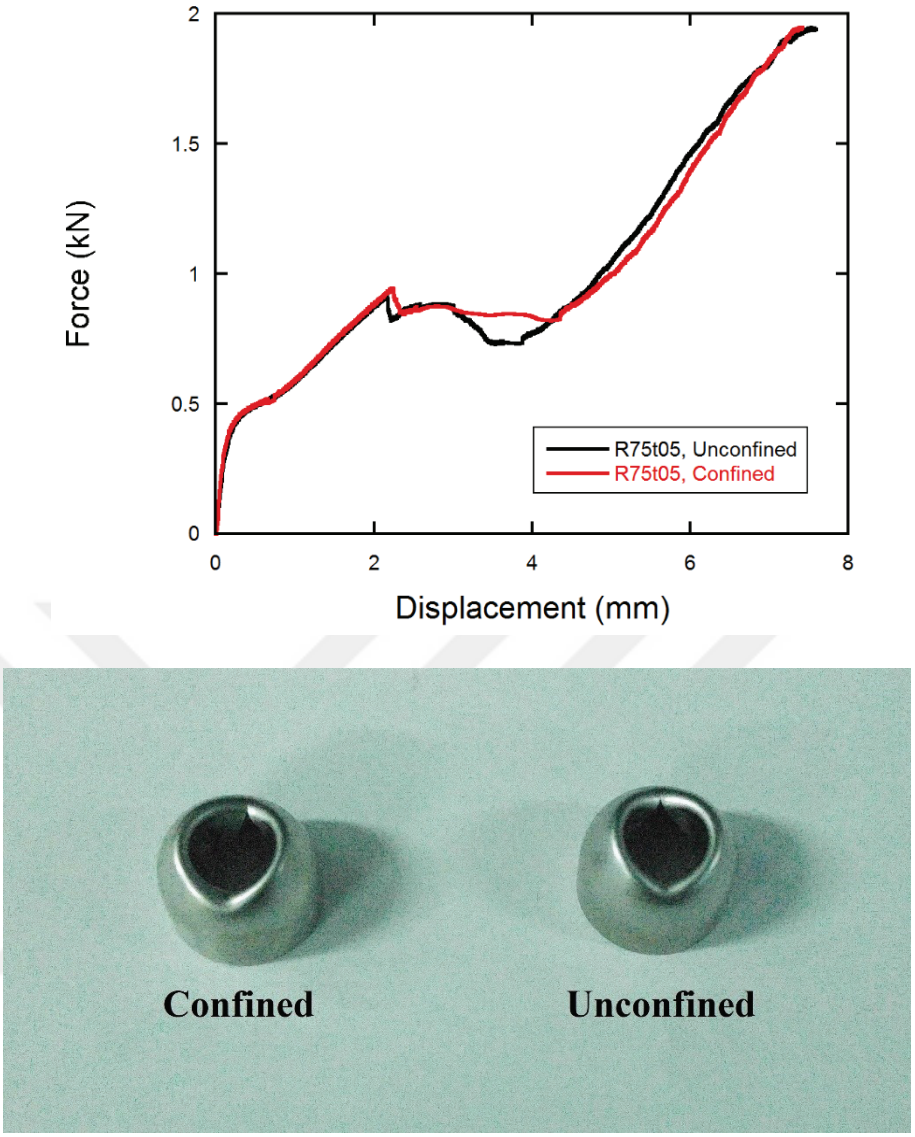

Figure 6.9. Comparison of test results and deformed specimens with confined and unconfined states (R75t05 core units against conical tipped indenter).

Last group of tests on radially confined as-received R75t05 core structure was conducted against hemispherical tipped indenter and experimental results were compared with unconfined tests in Figure 6.10. Experimental curves from both tests indicated a common, similar to bi-linear trend with no effect of confinement on structure against hemispherical tipped indenter. Radial tearing of hemispherical domed cone was noted in both types of experiments and deformed specimens after the tests were also given in Figure 6.10.

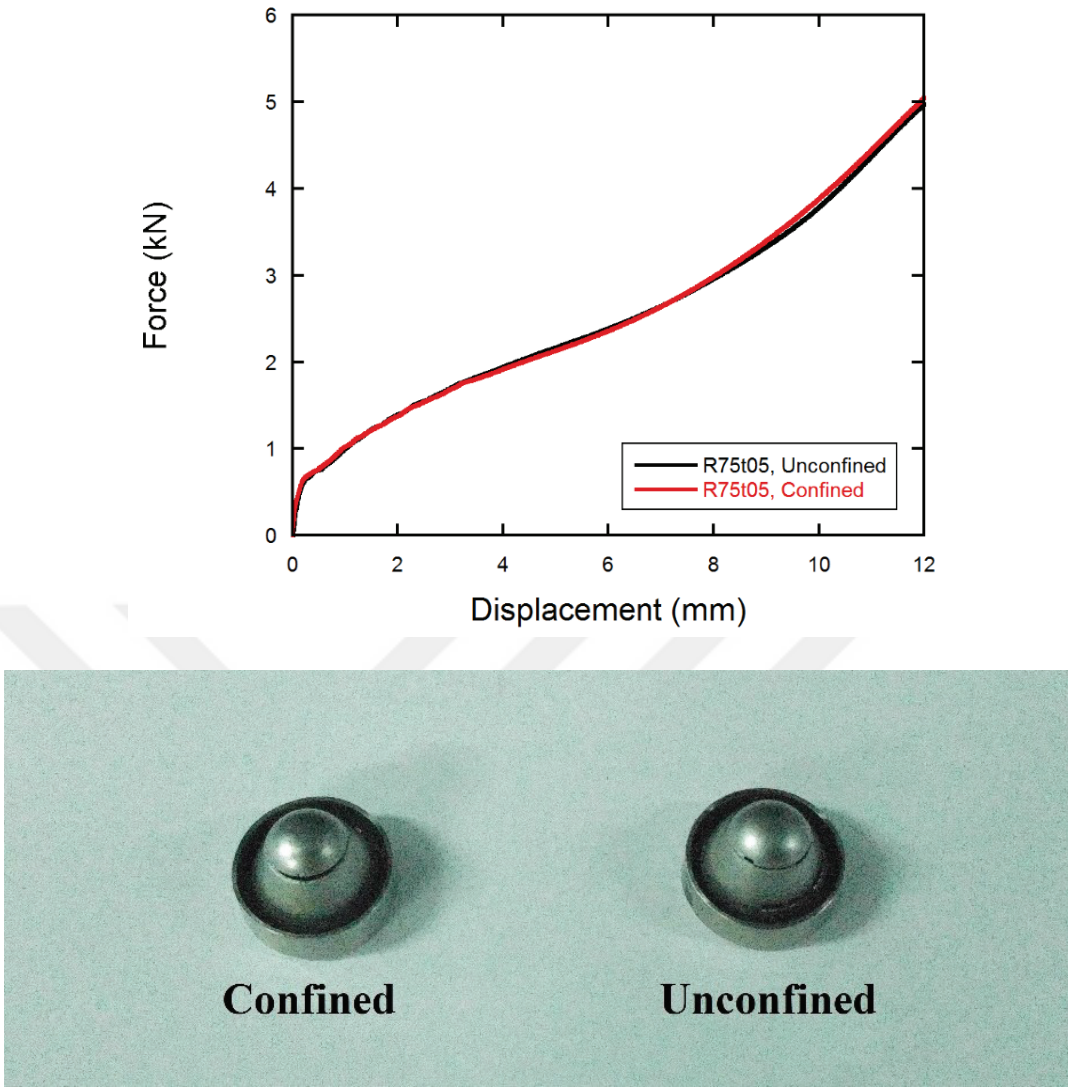

Figure 6.10. Comparison of test results and deformed specimens with confined and unconfined states (R75t05 core units against hemisphere tipped indenter).

Effect of radial confinement was also investigated on heat-treated R75t05 structure and experimental study was initiated with tests against blunt tipped indenter. Results given in Figure 6.11 indicate that behavior followed a common trend with unconfined structure. Deformation mode for both types of structure was found to be plugging of inversely formed cone and hexagonal shape was noted outer perimeter of confined specimen due to radial confinement. Specimens after the tests were also given in Figure 6.11.

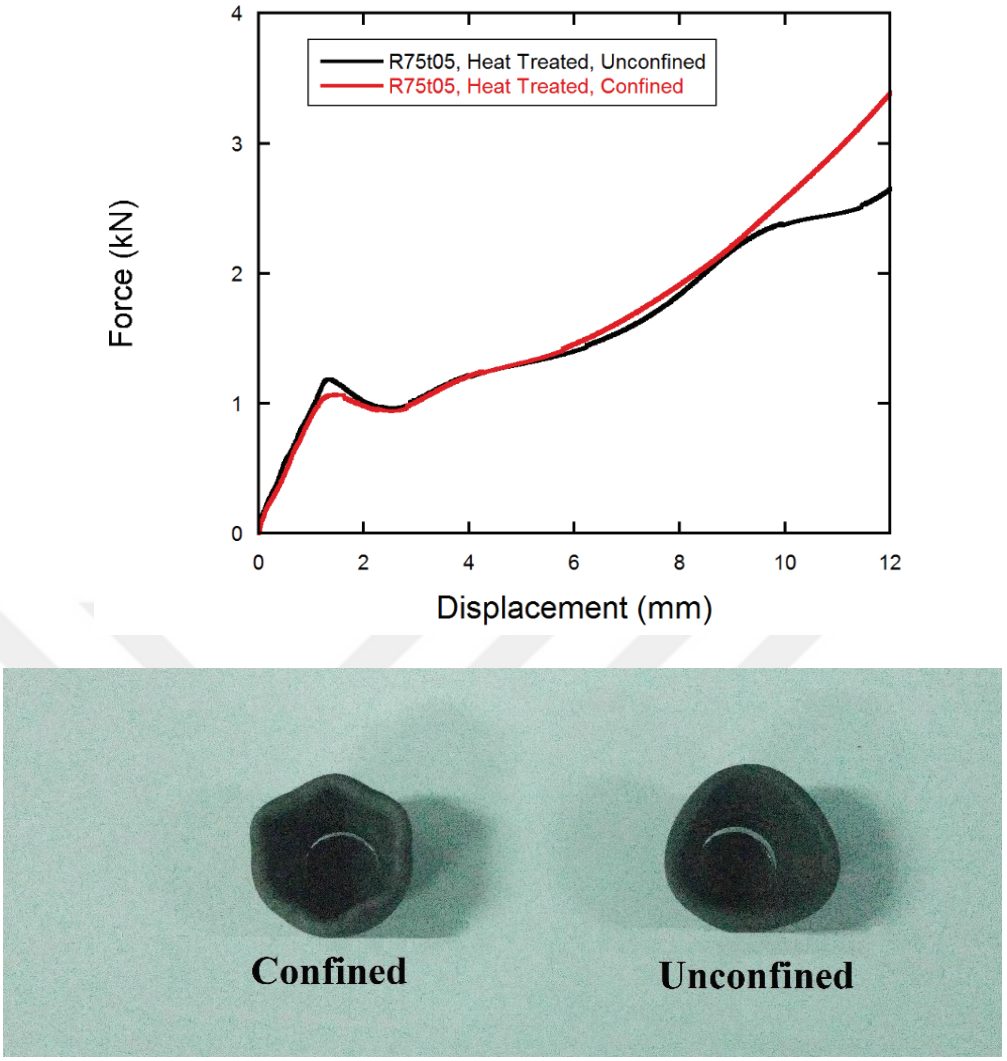

Figure 6.11. Comparison of test results and deformed specimens with confined and unconfined states (heat treated R75t05 core units against blunt tipped indenter).

Tests with conical tipped indenter on confined and heat-treated R75t05 structure was also conducted and comparative results with unconfined structure were given in Figure 6.12. It can be seen from force-displacement curves that both physical conditions produced a bi-linear behavior with similar fracture displacements, indicating that confinement does not have an effect on test results. Specimens after both tests also show symmetrical tearing and were given in Figure 6.12.

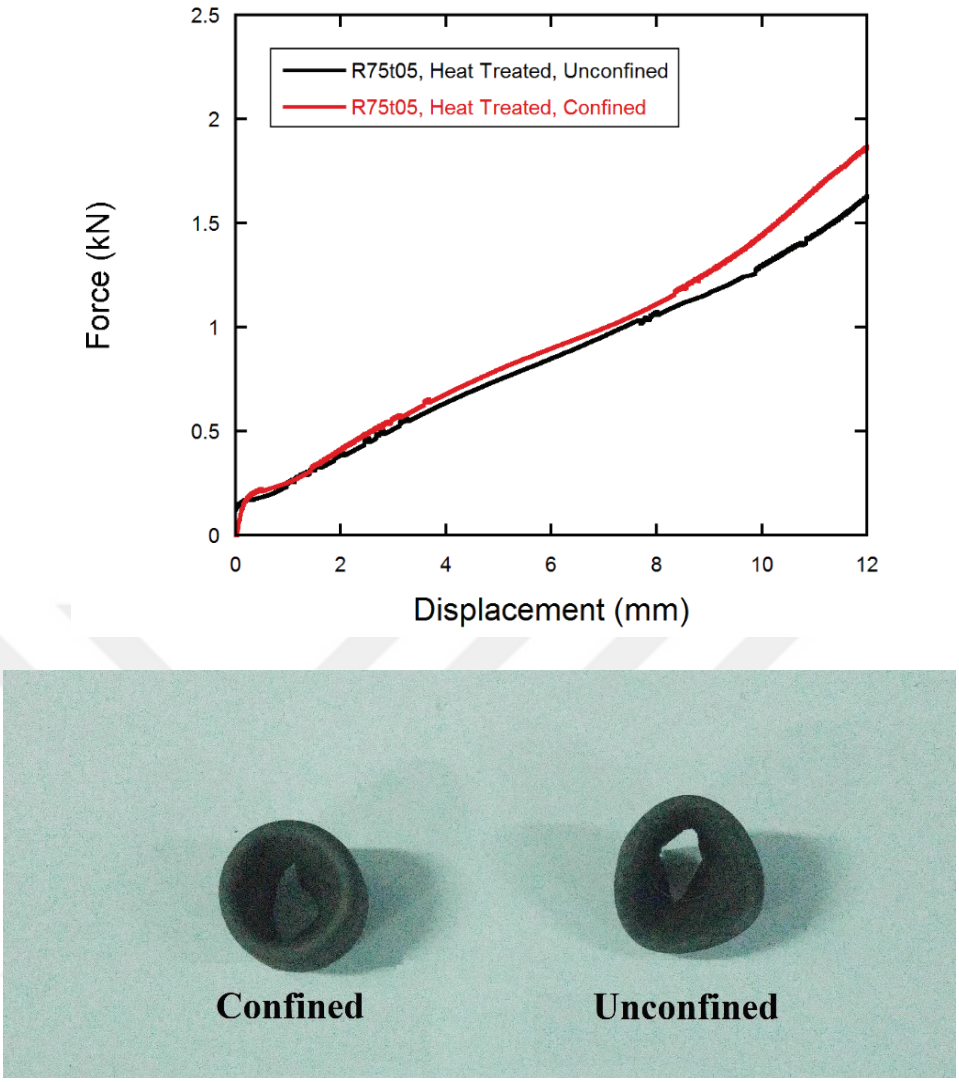

Figure 6.12. Comparison of test results and deformed specimens with confined and unconfined states (heat treated R75t05 core units against conical tipped indenter).

Experimental studies on investigations of confinement on penetration behavior were completed by conducting tests against hemisphere tipped indenter on heat-treated R75t05 structure. Comparative results given in Figure 6.13 indicate that general behavior is independent of confinement conditions and structure shows a bilinear force-displacement curve followed by rapid densification. Deformation mode was noted as radial tearing of hemispherical domed cone and photographs of fractured specimens were also given also in Figure 6.13.

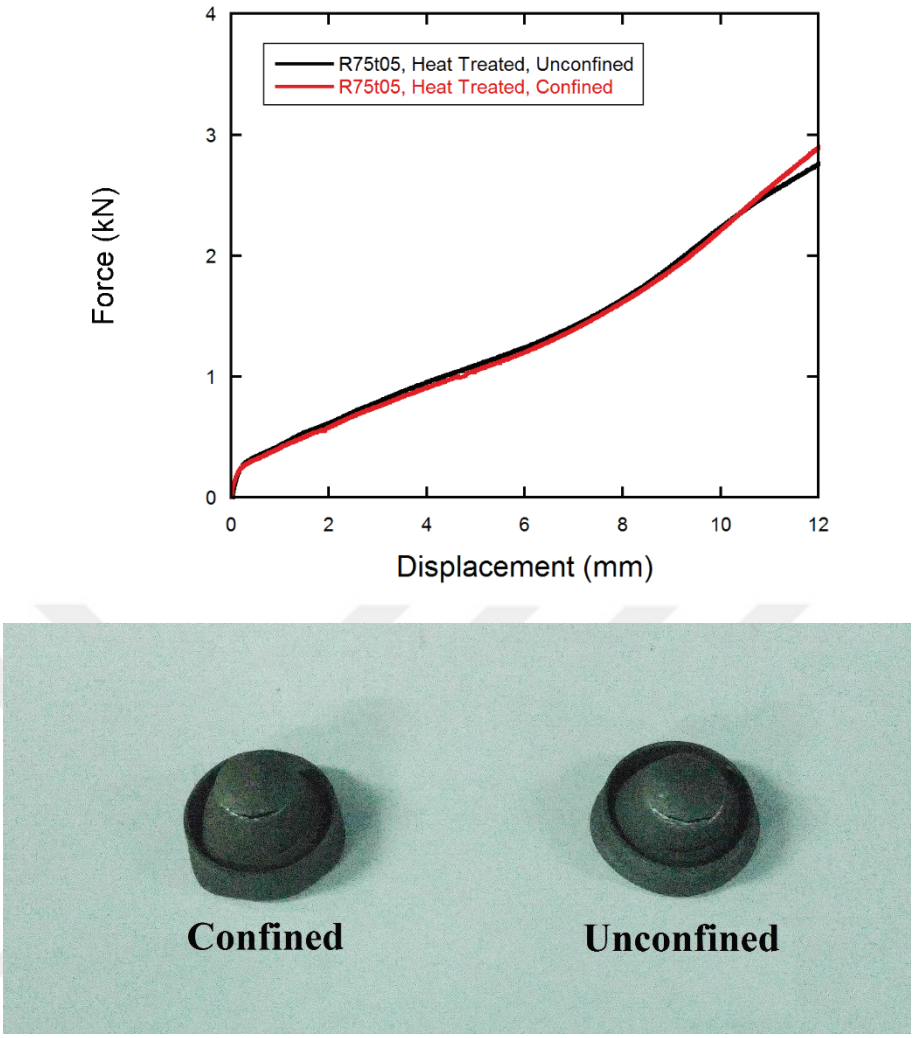

Figure 6.13. Comparison of test results and deformed specimens with confined and unconfined states (heat treated R75t05 core units against hemisphere tipped indenter).

CHAPTER 7

INVESTIGATION OF PERFORMANCE OF CORE STRUCTURE AGAINST BALLISTIC TESTS

This chapter focuses on ballistic performance of core structures when subjected to ballistic tests with varying impact velocities and changing condition of core units. Details of specimen conditions, test method and results were presented in following subsections.

7.1. Materials and Method

Core structures which were tested in previous experimental work was tested against intermediate velocity impact of a projectile by conducting ballistic tests in Dynamic Testing and Modelling Laboratory of IZTECH. For this purpose, sandwich structures with E-glass/Epoxy face sheets and combined geometry core structure were created, with each face sheet having a thickness of 5 mm. Dimensions of each core structure was noted to be 200 mm on impact-facing plane and thickness of 25 mm, indicating a sample weight of 820 g for R75t05 core structure and 1025 g for R75t1 core structure. Specimen holder of test chamber was designed to allow a square area with a side dimension of 150 mm for testing. Thus, in order to be able to trace the exact location of impact, bottom plate of each sandwich structure was marked with letters on columns and numbers on rows and each core structure was coded with permanent marker with a combination of a letter and number, regarding to its position. It should be noted that heat treated core structures were also used to investigate effect of treatment on ballistic test performance and sandwich structures with as-received and heat-treated core units were given in Figure 7.1a and 7.1b, respectively.

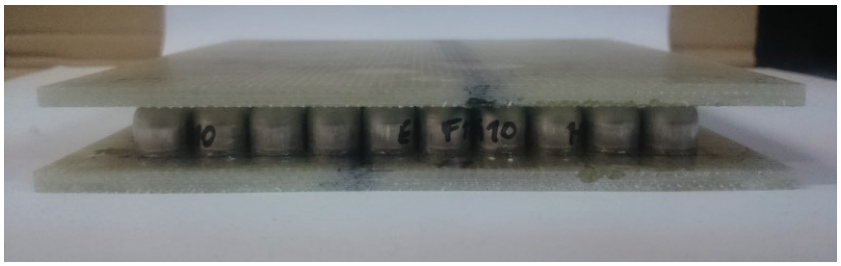

(a)

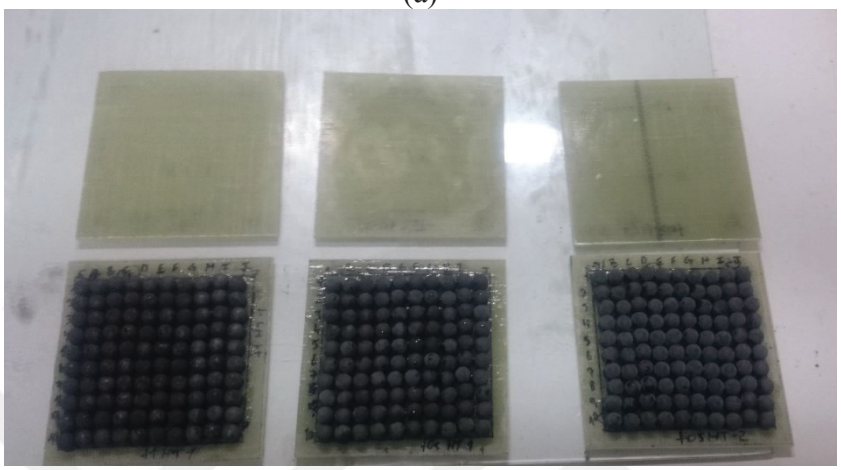

(b)

Figure 7.1. Sandwich structures with (a) as-received, (b) heat treated core units.

During experimental study, ballistic tests of core structure were done with following methodology: specimens were assembled to the specimen holder of impact chamber. Then, air is pressurized and transferred to the gas chamber of testing equipment while continuously monitored with pressure gauges. When the desired chamber pressure is reached, a polymeric sabot containing the projectile is put into the nozzle of gas chamber. Upon triggering of pressure discharge valve, projectile is accelerated with the force acting on sabot due to release of pressurized air and travels through the nozzle with sabot. At the very tip of the nozzle, sabot is pierced upon impact to the stripper and projectile continues to travel to its target, which is the sandwich structure in current study. Pre-impact velocity of projectile is recorded by laser sensors just after sabot and projectile is separate while post-impact velocity is also recorded if backing plate is fully penetrated. While the testing equipment is able to fire different kinds of projectiles, a steel ball having a diameter of 30 mm and a mass of 110 g was used during the experimental study. An image of test chamber in IZTECH is given in Figure 7.2.

Figure 7.2. Ballistic test chamber of IZTECH.

7.2. Ballistic Tests of Core Structure

Experimental study was done with two different pressure levels to observe if the behavior does change with impact velocity significantly. Thus, impact velocities were ranged between 140-180 $m.s^{-1}$, depending on pressure of impact chamber and total weight of projectile and sabot. Based on experimental data with 30 mm steel projectile with a weight of 110 g, chamber pressure-impact velocity data of testing equipment is given in Figure 7.3. This curve also represents the repeatability of the experimental method as recorded impact velocities were found to be very close for each level of chamber pressure.

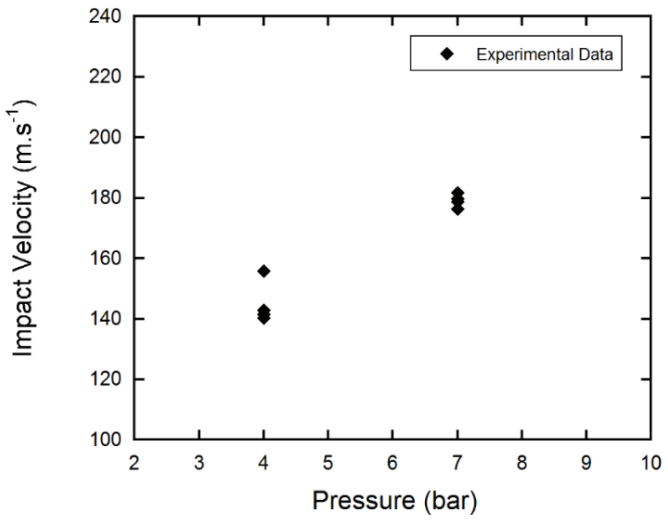

Figure 7.3. Change of impact velocity with chamber pressure.

Tests of as-received R75t1 core structure were conducted at chamber pressures of 4 and 7 bar which corresponded to the impact velocities of 141.44 and 179.69 $m.s^{-1}$, respectively. Initial tests on R75t1 core structure was conducted at impact velocity of 141.44 $m.s^{-1}$ and post-test photographs were given in Figure 7.4. Impact of spherical projectile had caused a full perforation on front plate and crushed the core structures on columns C-D and rows 3-4, damaging a total number of 4 core structures. Deformed core structures only indicated inward bending of spherical portions and cylindrical segment of core structures were remain undamaged. Instead of fully crushing or fracture of core units, cylindrical body of core units were noted to be pressed into the backing plate which caused localized fracture of fibers. It was also observed that core units were able to fully stop the projectile and backing plate was not perforated. Failure type of layer delamination was present as dominant damage mode.

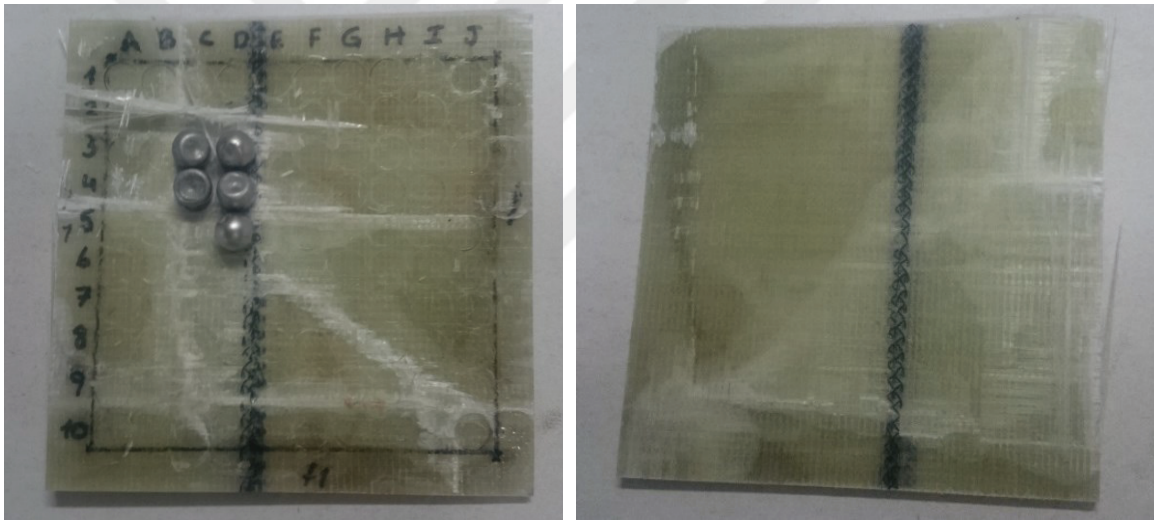

(a) (b)

Figure 7.4. Photographs of sandwich structure with R75t1 core units; (a) impacted core structure, (b) backing plate (impact velocity: 141.44 $m.s^{-1}$).

Post-test evaluation of sandwich structures with R75t1 core units at impact velocity of 179.69 $m.s^{-1}$ showed that projectile had fully perforated the front face and impacted the sandwich structure at columns G-H and rows 4-5, indicating a direct hit on 4 core structures. Due to the high velocity impact, hemispherical portions of core structure were folded inwardly. However, instead of full compression or fracture of core structure, cylindrical segments of core units were pushed into backing plate and a more localized damage in the form of a hollow tube was noted. Even though the impact damage was noted as localized, core structure was able to hold the penetrator and had

avoided the full perforation of backing plate. Layer delamination was observed on backing plate due to bending caused by impact. Photographs of sandwich structure after the test were given in Figure 7.5.

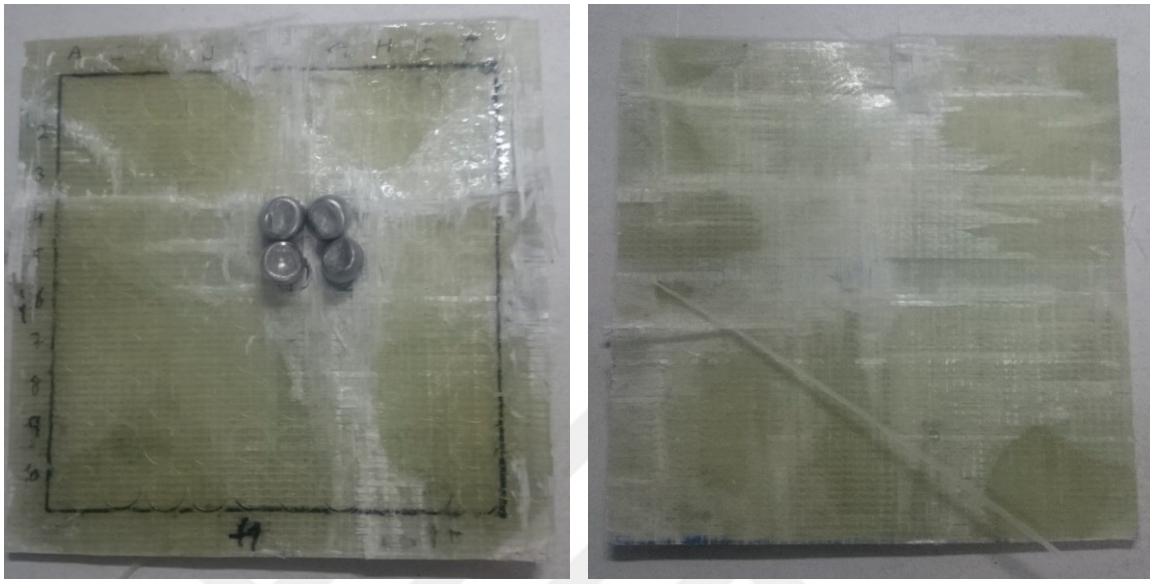

(a) (b)

Figure 7.5. Photographs of sandwich structure with R75t1 core units; (a) impacted core structure, (b) backing plate (impact velocity: 179.69 $m.s^{-1}$).

Sandwich structures with as-received R75t05 core structure were tested at impact velocities of 155.82 and 178.65 $m.s^{-1}$ against spherical projectile and post-test photographs of sandwich structure against lower impact velocity is given in Figure 7.6. As in tests of R75t1 core units, front plate was fully perforated with fiber fracture as main mode. Impact of projectile was marked on columns E-G and rows 3-5, indicating a total number of 7 core units directly deformed during experimental study. Instead of non-deformed cylindrical segments of R75t1 structure, some of the core units of R75t05 were noted to be fully crushed and total number of deformed core units were increased, indicating that impact energy is much more dissipated by core units when compared to previous tests. This comment is also verified with reduced local damage on backing plate, which was also governed by the damage mode of layer delamination and bending with no perforation.

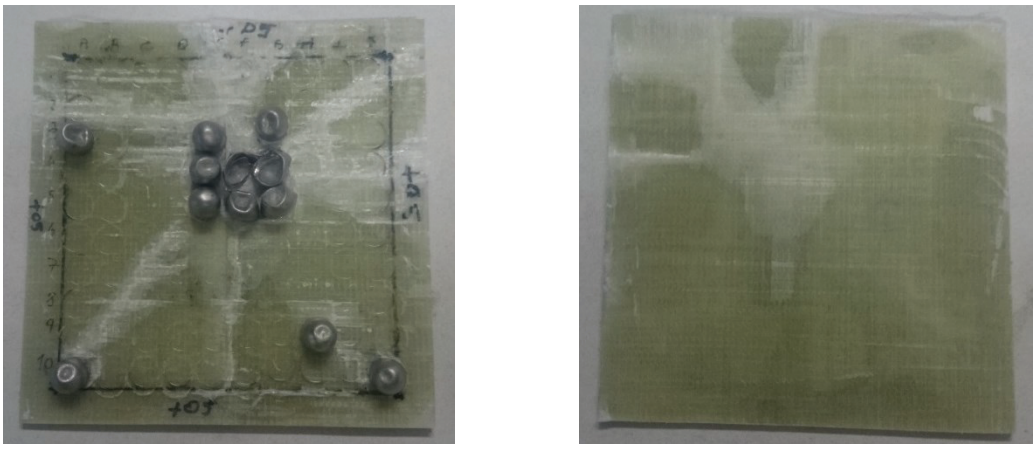

(a) (b)

Figure 7.6. Photographs of sandwich structure with R75t05 core units; (a) impacted core structure, (b) backing plate (impact velocity: 155.82 m.s^{-1}).

Last group of tests on as received core structures were conducted on sandwich specimens with R75t05 core units against an impact velocity of 178.65 m.s^{-1} and results were presented on Figure 7.7. Projectile had fully perforated the first layer of sandwich structure and had hit the core units on columns E-G and rows 3-5, directly damaging 8 pieces. Some of the aforementioned core units were observed to be fully crushed during testing while rest of them were deformed on hemispherical segments. Localized damage is evident on impact area since projectile had pushed the core units to the backing plate and resulted in partial perforation by fiber crushing. Backing plate was noted to be not fully perforated through the test and delamination of layers was observed as dominant damage mode.

(a) (b)

Figure 7.7. Photographs of sandwich structure with R75t05 core units; (a) impacted core structure, (b) backing plate (impact velocity: 178.65 m.s^{-1}).

Aforementioned core units were also heat treated to observe if heat treatment has an effect on the penetration behavior. Heat treatment operation followed the same process as in previous experimental study of core units and were bonded to the face sheets of composite structure with epoxy. Then, sandwich structures with heat treated core units were tested against spherical projectile at two different chamber pressures, resulting in impact velocities ranging between 142.94 and 181.63 $m.s^{-1}$. Test were initiated on sandwich structures with R75t1 heat treated core units against impact velocity of 142.94 $m.s^{-1}$ and post-test photographs were given in Figure 7.8. Front plate of the sandwich structure was noted to be fully perforated upon impact with localized fiber fracture at the impact location and delamination around impact area. Then, core units at columns F-G and rows 3-5 were crushed, indicating deformation on both hemispherical and cylindrical portions; rather than damaging only of the hemispherical portion as in tests of as-received core units. It should be noted that effect of heat treatment resulted in softening of core structure, leading to reduction of the amount perforation of core units to the backing plate. Total number of directly deformed core units were also increased from 4 to 10 which also indicates that impact energy was absorbed by more units and wider area, which in turn reduced the stresses related to impact on backing plate and prevented full perforation. Localized delamination of layers was noted as dominant damage mode on backing plate.

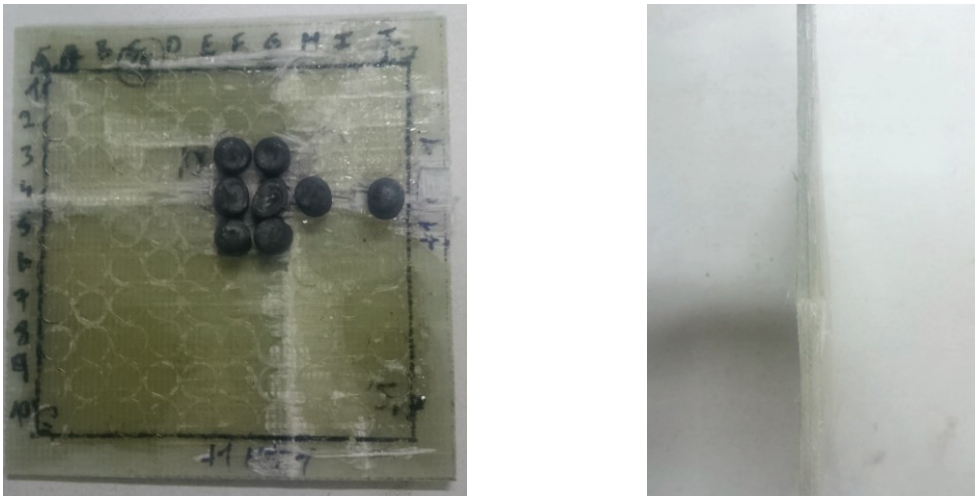

(a) (b)

Figure 7.8. Photographs of sandwich structure with R75t1HT core units; (a) impacted core structure, (b) backing plate (impact velocity: 142.94 $m.s^{-1}$).

After completion of initial tests on R75t1 heat treated core structure, impact velocity was increased to 181.63 $m.s^{-1}$ and photographs of sandwich structure after the tests were presented on Figure 7.9. Upon impact, front plate of sandwich structure was fully perforated and projectile had deformed the core units on column E-G and rows 5-6. Core units on impact area were noted to be deformed on both hemispherical and cylindrical portions as in previous impact velocity. In addition, increased impact velocity resulted in localized layer delamination in one of the main fiber directions (0°) on impact facing side of backing plate. Full perforation of projectile on backing plate was not observed during the tests.

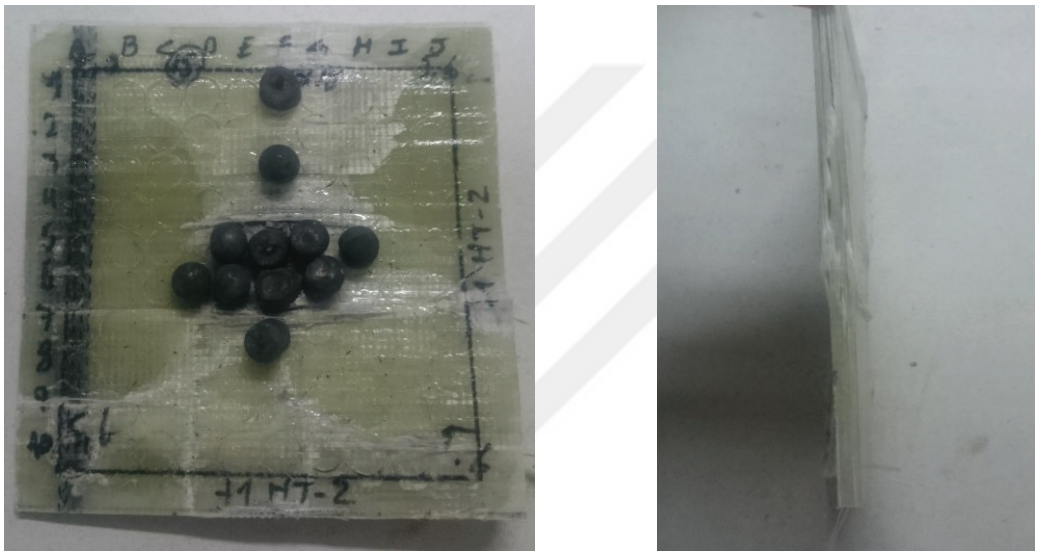

(a) (b)

Figure 7.9. Photographs of sandwich structure with R75t1HT core units; (a) impacted core structure, (b) backing plate (impact velocity: 181.63 $m.s^{-1}$).

Ballistic tests of sandwich structure were finished with the experimental study on sandwich structures with heat treated R75t05 core units against two different impact chamber pressures and photographs of test results conducted at impact velocity of 140.30 $m.s^{-1}$ were given in Figure 7.10. During the tests, projectile was fully perforated the front plate and had impacted the core units on columns D-F and rows 3-5, directly damaging 6 core units. It was noted that impact of projectile caused crushing of core units on hemispherical and cylindrical portions with no perforation of core units to the backing plate. In addition, core units were able to stop the projectile and damage on backing plate was noted to be dominated by layer delamination as in previous tests.

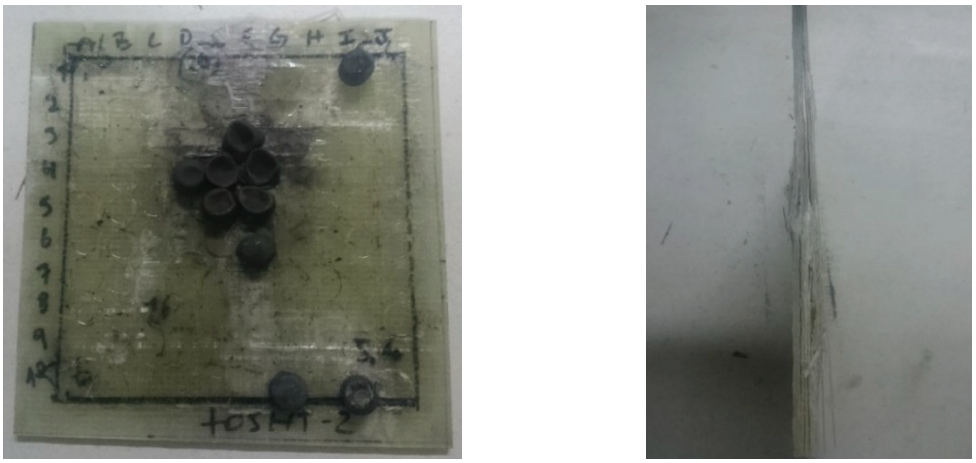

(a) (b)

Figure 7.10. Photographs of sandwich structure with R75t05HT core units; (a) impacted core structure, (b) backing plate (impact velocity: 140.30 m.s^{-1}).

Last group of tests were done on sandwich structures with heat treated R75t05 core units against an impact velocity of 176.41 m.s^{-1} and photographs of sandwich structures after the test were given in Figure 7.11. It was observed that projectile had perforated the front plate and directly deformed 8 core units on columns E-H and rows 3- 5. Impacted core units indicated deformation on both portions of geometry while post-test study showed that impact caused global bending of sandwich structure and some of the surrounding core units were also deformed on hemispherical portions. Perforation was not observed on backing plate after the test.

(a) (b)

Figure 7.11. Photographs of sandwich structure with R75t05HT core units; (a) impacted core structure, (b) backing plate (impact velocity: 176.41 m.s^{-1}).

CHAPTER 8

CONCLUSIONS

In this study, penetration behavior of combined geometry novel core units with hemispherical cap and cylindrical segments were investigated against different types of indenter geometries at various indenter velocities, both experimentally and numerically. Effect of heat treatment on penetration behavior of deep drawn core units were also investigated, along with experimental work focusing on effect of radial confinement on deformation of core units. Finally, a case study was done with investigated geometry used as core units in a sandwich structure which was subjected to projectile impact at highest impact velocity around 180 $m.s^{-1}$.

Experimental and numerical results enabled to conclude following remarks throughout the study:

- Experimental study initiated with mechanical characterization of base material at low and high strain rates. As expected from previous studies on literature, AISI 304 L exhibited a strain rate dependent behavior where it can be modeled with a strain and strain rate hardening. In order to conduct successful numerical modeling studies, parameters of Johnson-Cook constitutive equation and damage model were used.
- Numerical studies also included the numerical modeling of manufacturing process of core structure as distribution of residual stresses and strains play an important role on both experimental and numerical results. Numerically deep-drawn core units with good correlation of thickness values with measured core units were used in modeling of performance evaluation tests on later stages.
- Performance evaluation tests were initiated by conducting experimental work on single core units with two different thickness levels. three different indenter geometries were used, namely as blunt, conical and hemispherical tipped indenters to observe their effect on penetration behavior. Experimental study showed that each indenter geometry yielded in different forms of deformation and force-

displacement curves with unique characteristics. Tests on R75t05 core units indicated that highest AEF value of 39.91 kJ/kg was recorded on tests against blunt tipped indenter, followed by tests on hemispherical and conical indenters with AEF values of 30.13 and 8.05 kJ/kg, respectively. When the thickness of core geometry was increased and R75t1 core geometry was investigated, highest AEF value was noted during tests against hemispherical tipped indenter with 93.96 kJ/kg, followed by blunt and conical indenters with AEFs calculated as 46.79 kJ/kg and 26.89 kJ/kg, respecitvely. Thickness of core units also has an effect on AEF values as experimental work indicates that AEF values increase with thickness regardless of indenter type. However, with the increase of weight due to thickness increase, SAE of core units against blunt tipped indenter tends to decrease with increasing thickness. It was observed that strain rate also had a negative effect on AEF and SAE values as experimental work on R75t1 core units show that AEF and SAE decrease around 72% for tests with blunt indenter and 65% with conical indenter, with the increasing strain rate. Experimental results were tabulated in Table 8.1.

- Effect of heat treatment on penetration behavior was investigated by conducting a stress relieving operation on as received core units, followed by performance evaluation tests. Results indicated that force-displacement behavior of both core units changed significantly with removal of residual stresses and strains with heat treatment operation. When heat treatment was applied, work hardening effects were also vanished from core units and this resulted in alteration of all force-displacement curves as well as reduction of force related terms such as mean and maximum force levels. However, on tests of conical tipped indenter, absorbed energy levels were noted to increase with heat treatment operation such as tests of conical tipped indenter showed an increase of 1.93 J and 6.09 J for core units of R75t05 and R75t1, respectively. Significant improvement of absorbed energy was recorded in tests of R75t1 structure against blunt tipped indenter after heat treatment and difference of absorbed energy levels were calculated as 27.57 J. Increase in absorbed energy levels are fully related with increased displacements after heat treatment and this increase in obtained displacements can be commented as early failure displacements observed on as-received structures were related mostly with deformation history which was created on manufacturing process. Tests with hemispherical tipped indenter showed reduction of both force levels and absorbed energy as deformation

is global rather than local as in other tip geometries. Experimental results were given in Table 8.1.

- Numerical modeling studies of performance evaluation tests were conducted for both as received and heat-treated core units. As-received core units were taken from numerical modeling of deep drawing operation which is in good correlation with actual measurements while numerical heat treatment was done by eliminating residual stress and strain data from numerical core structure. Deforming contact between core units and indenters were defined with eroding contact algorithms and Johnson-Cook material model with constants found in experimental work was occupied. Numerical results indicated very good correlation for both as-received and heat-treated core units in terms of deformation types as well as force-displacement behavior. Consistence of experimental and numerical results further allowed to observe the effect of strain rate and inertia effects on a case study where both core units were subjected to impact by hemispherical tipped indenter at 300 $m.s^{-1}$. Numerical results showed that both strain rate and micro-inertia effects were dominant and force-displacement curves become distinct by favoring the strain rate effects over micro inertia over a threshold level for both core units. This threshold values were found to be 5 mm and 3 mm for R75t05 and R75t1 core units, respectively.
- Effect of confinement on penetration behavior of core units were investigated by conducting performance evaluation tests on specimens with special fixture. As-received and heat-treated core units of were radially confined with other non-deforming core elements and experimental procedure followed the same methodology with tests of single core units. Comparison of test results on single and confined units indicated similar values of force under same displacements on tests of both as-received and heat-treated units, indicating that radial confinement is found to be effective only on behavior of R75t1 core units against conical tipped indenter. Final deformation modes were noted to be mostly same with tests of single core units whereas formation of hexagonal shape on outer diameter of heat treated specimens was observed, which can be related with contact of relatively softer specimen with confining core units.
- Last part of the thesis included a case study where core units were sandwiched between composite face plates and were subjected to impact by a steel spherical projectile at impact velocities between 140 and 180 $m.s^{-1}$. Effect of heat treatment

was also added to the study by conducting experimental work with heat treated core units. Projectile impact tests conducted on ballistic chamber indicated that R75t1 structures in as-received condition were deformed only in hemispherical regions where R75t05 structures were fully deformed which resulted in reduced damage on backing plate. Total number of affected core units tend to increase with reduced core unit thickness and indicated that deformation is evolved from local to global. Heat treatment also increased the total number of deformed core units of sandwich structures and backing plate damage noted to be increased when compared with as-received core units. Both core geometries, either in as-received or heat-treated condition, were able to successfully hold the projectile up to impact velocities of 180 $m.s^{-1}$ as backing plates were not perforated during the tests. Delamination of layers and localized fiber fracture was observed on backing plate during experimental study.

Table 8.1. AEF values of core units against test velocity of 0.13 $mm.s^{-1}$.

Core Unit Geometry & Condition / Indenter Type	**Blunt Indenter**	**Conical Indenter**	**Hemispherical Indenter**
R75t05 AR	39.91	8.05	30.13
R75t05 HT	18.81	9.98	16.45
R75t05 AR, Confined	40.32	7.38	30.61
R75t05 HT,Confined	19.92	11.08	16.12
R75t1 AR	46.79	26.89	93.96
R75t1 HT	74.36	32.98	50.61
R75t1 AR, Confined	45.43	34.45	94.71
R75t1 HT,Confined	85.57	34.42	51.56

For future works, the following can be proposed:

- Investigation of multiple projectile impact on sandwich structure can be done by conducting both experimental and numerical studies. Multiple projectile impact caused by blast and explosion was previously observed on real life scenarios and

experimental and/or numerical studies may reveal unknown characteristics of proposed core structure.

- Optimization of core unit behavior by changing the shell thickness and overall dimensions can be studied to observe the effect of geometric parameters such as length, radius of hemispherical portion etc. on penetration behavior and SAE of the structure.
- Conducting further experimental study on sandwich structures by changing the indenter type and velocity levels to further investigate the behavior of sandwich structure and core units when subjected to different types threats.

REFERENCES

AISI 4140 Steel, oil quenched, 205°C (400°F) temper, 25 mm (1 in.) round. Retrieved May 9, 2018, from www.matweb.com/search/DataSheet.aspx?MatGUID=757684bcff76455eaf94b20102617988

Aktay, L., Toksoy, A. K., & Güden, M. (2006). Quasi-static axial crushing of extruded polystyrene foam-filled thin-walled aluminum tubes: Experimental and numerical analysis. *Materials & Design, 27*(7), 556-565. doi: http://dx.doi.org/10.1016/j.matdes.2004.12.019

Alavi Nia, A., & Hoseini, G. R. (2011). Experimental study of perforation of multi-layered targets by hemispherical-nosed projectiles. *Materials & Design, 32*(2), 1057-1065. doi: http://dx.doi.org/10.1016/j.matdes.2010.07.001

Amiri, S. N., & Rasheed, H. A. (2012). Plastic buckling of thin hemispherical shell subjected to concentrated load at the apex. *Thin-Walled Structures, 53*, 72-82. doi: 10.1016/j.tws.2011.11.009

Babaei, B., Shokrieh, M. M., & Daneshjou, K. (2011). The ballistic resistance of multi-layered targets impacted by rigid projectiles. *Materials Science and Engineering: A, 530*, 208-217. doi: http://dx.doi.org/10.1016/j.msea.2011.09.076

Børvik, T., Hopperstad, O. S., Langseth, M., & Malo, K. A. (2003). Effect of target thickness in blunt projectile penetration of Weldox 460 E steel plates. *International Journal of Impact Engineering, 28*(4), 413-464. doi: http://dx.doi.org/10.1016/S0734-743X(02)00072-6

Børvik, T., Langseth, M., Hopperstad, O. S., & Malo, K. A. (1999). Ballistic penetration of steel plates. *International Journal of Impact Engineering, 22*(9–10), 855-886. doi: http://dx.doi.org/10.1016/S0734-743X(99)00011-1

Børvik, T., Langseth, M., Hopperstad, O. S., & Malo, K. A. (2002). Perforation of 12 mm thick steel plates by 20 mm diameter projectiles with flat, hemispherical and conical noses: Part I: Experimental study. *International Journal of Impact Engineering, 27*(1), 19-35. doi: http://dx.doi.org/10.1016/S0734-743X(01)00034-3

Børvik, T., Leinum, J. R., Solberg, J. K., Hopperstad, O. S., & Langseth, M. (2001). Observations on shear plug formation in Weldox 460 E steel plates impacted by blunt-nosed projectiles. *International Journal of Impact Engineering, 25*(6), 553-572. doi: http://dx.doi.org/10.1016/S0734-743X(00)00069-5

Calladine, A. J. M. C. R. (1969). The local strength of a thin spherical shell loaded radially through a rigid boss. *Proc. of 1st Int. Conf. on Pressure Vessel Technology*.

Calladine, C. R., & English, R. W. (1984). Strain-rate and inertia effects in the collapse of two types of energy-absorbing structure. *International Journal of Mechanical Sciences, 26*(11), 689-701. doi: https://doi.org/10.1016/0020-7403(84)90021-3

Chen, X. W., Yang, Y. B., Lu, Z. H., & Chen, Y. Z. (2008). Perforation of metallic plates struck by a blunt projectile with a soft nose. *International Journal of Impact Engineering, 35*(6), 549-558. doi: http://dx.doi.org/10.1016/j.ijimpeng.2007.05.002

De Oliveira, J. G., & Wierzbicki, T. (1982). CRUSHING ANALYSIS OF ROTATIONALLY SYMMETRIC PLASTIC SHELLS. *Journal of Strain*

Analysis for Engineering Design, 17(4), 229-236. doi: 10.1243/03093247v174229

Deng, Y., Zhang, W., & Cao, Z. (2012). Experimental investigation on the ballistic resistance of monolithic and multi-layered plates against hemispherical-nosed projectiles impact. *Materials & Design, 41*, 266-281. doi: http://dx.doi.org/10.1016/j.matdes.2012.05.021

Deng, Y., Zhang, W., & Cao, Z. (2013). Experimental investigation on the ballistic resistance of monolithic and multi-layered plates against ogival-nosed rigid projectiles impact. *Materials & Design, 44*, 228-239. doi: http://dx.doi.org/10.1016/j.matdes.2012.06.048

Dey, S., Børvik, T., Teng, X., Wierzbicki, T., & Hopperstad, O. S. (2007). On the ballistic resistance of double-layered steel plates: An experimental and numerical investigation. *International Journal of Solids and Structures, 44*(20), 6701-6723. doi: http://dx.doi.org/10.1016/j.ijsolstr.2007.03.005

DIN. (2014). Stainless steels – Part 3: Technical delivery conditions for semi-finished products, bars, rods, wire, sections and bright products of corrosion resisting steels for general purposes (Vol. DIN EN10088-3:2014, pp. 77). Berlin: DIN Deutsches Institut für Normung e. V.

Forrestal, M. J., Luk, V. K., & Brar, N. S. (1990). Perforation of aluminum armor plates with conical-nose projectiles. *Mechanics of Materials, 10*(1), 97-105. doi: http://dx.doi.org/10.1016/0167-6636(90)90020-G

Guo, K., Zhu, L., Li, Y., Yu, T. X., Shenoi, A., & Zhou, Q. (2018). Experimental investigation on the dynamic behaviour of aluminum foam sandwich plate under repeated impacts. *Composite Structures, 200*, 298-305. doi: https://doi.org/10.1016/j.compstruct.2018.05.148

Gupta, N. K., Iqbal, M. A., & Sekhon, G. S. (2006). Experimental and numerical studies on the behavior of thin aluminum plates subjected to impact by blunt- and hemispherical-nosed projectiles. *International Journal of Impact Engineering, 32*(12), 1921-1944. doi: http://dx.doi.org/10.1016/j.ijimpeng.2005.06.007

Gupta, N. K., Iqbal, M. A., & Sekhon, G. S. (2008). Effect of projectile nose shape, impact velocity and target thickness on the deformation behavior of layered plates. *International Journal of Impact Engineering, 35*(1), 37-60. doi: http://dx.doi.org/10.1016/j.ijimpeng.2006.11.004

Gupta, N. K., Mohamed Sheriff, N., & Velmurugan, R. (2008a). Analysis of collapse behaviour of combined geometry metallic shells under axial impact. *International Journal of Impact Engineering, 35*(8), 731-741. doi: http://dx.doi.org/10.1016/j.ijimpeng.2008.01.005

Gupta, N. K., Mohamed Sheriff, N., & Velmurugan, R. (2008b). Experimental and theoretical studies on buckling of thin spherical shells under axial loads. *International Journal of Mechanical Sciences, 50*(3), 422-432. doi: http://dx.doi.org/10.1016/j.ijmecsci.2007.10.002

Gupta, N. K., & Venkatesh. (2004). Experimental and numerical studies of dynamic axial compression of thin walled spherical shells. *International Journal of Impact Engineering, 30*(8–9), 1225-1240. doi: http://dx.doi.org/10.1016/j.ijimpeng.2004.03.009

Hou, W., Zhu, F., Lu, G., & Fang, D.-N. (2010). Ballistic impact experiments of metallic sandwich panels with aluminium foam core. *International Journal of Impact Engineering, 37*(10), 1045-1055. doi: http://dx.doi.org/10.1016/j.ijimpeng.2010.03.006

Huang, X., Zhang, W., Deng, Y., & Jiang, X. (2018). Experimental investigation on the ballistic resistance of polymer-aluminum laminated plates. *International Journal of Impact Engineering, 113*, 212-221. doi: https://doi.org/10.1016/j.ijimpeng.2017.12.002

Johnson, G. R., and William H Cook. (1983). A Constitutive Model and Data for Metals Subjected to Large Strains, High Strain Rates and High Temperatures. *Proceedings 7th International Symposium on Ballistics*, 7.

Jordan, J. B., & Naito, C. J. (2014). An experimental investigation of the effect of nose shape on fragments penetrating GFRP. *International Journal of Impact Engineering, 63*, 63-71. doi: http://dx.doi.org/10.1016/j.ijimpeng.2013.08.002

Jover, N., Shafiq, B., & Vaidya, U. (2014). Ballistic impact analysis of balsa core sandwich composites. *Composites Part B: Engineering, 67*, 160-169. doi: http://dx.doi.org/10.1016/j.compositesb.2014.07.002

Kara, A. (2015). *Experimental and numerical approaches to evaluate the crushing behavior of combined geometry core sandwich structures against blast.* (Ph. D.), Izmir Institute of Technology, Izmir. Retrieved from http://openaccess.iyte.edu.tr/handle/11147/4453

Karnesky, J., Damazo, J., Chow-Yee, K., Rusinek, A., & Shepherd, J. E. (2013). Plastic deformation due to reflected detonation. *International Journal of Solids and Structures, 50*(1), 97-110. doi: https://doi.org/10.1016/j.ijsolstr.2012.09.003

Kolopp, A., Rivallant, S., & Bouvet, C. (2013). Experimental study of sandwich structures as armour against medium-velocity impacts. *International Journal of Impact Engineering, 61*, 24-35. doi: http://dx.doi.org/10.1016/j.ijimpeng.2013.05.007

Kõrgesaar, M., Romanoff, J., Remes, H., & Palokangas, P. (2018). Experimental and numerical penetration response of laser-welded stiffened panels. *International Journal of Impact Engineering, 114*, 78-92. doi: https://doi.org/10.1016/j.ijimpeng.2017.12.014

Kpenyigba, K. M., Jankowiak, T., Rusinek, A., Pesci, R., & Wang, B. (2015). Effect of projectile nose shape on ballistic resistance of interstitial-free steel sheets. *International Journal of Impact Engineering, 79*, 83-94. doi: http://dx.doi.org/10.1016/j.ijimpeng.2014.10.007

Kyner, A., Dharmasena, K., Williams, K., Deshpande, V., & Wadley, H. (2018). Response of square honeycomb core sandwich panels to granular matter impact. *International Journal of Impact Engineering, 117*, 13-31. doi: https://doi.org/10.1016/j.ijimpeng.2018.02.009

Lee, D.-W., Park, B.-J., Park, S.-Y., Choi, C.-H., & Song, J.-I. (2018). Fabrication of high-stiffness fiber-metal laminates and study of their behavior under low-velocity impact loadings. *Composite Structures, 189*, 61-69. doi: https://doi.org/10.1016/j.compstruct.2018.01.044

Lee, Y.-W., Woertz, J. C., & Wierzbicki, T. (2004). Fracture prediction of thin plates under hemi-spherical punch with calibration and experimental verification. *International Journal of Mechanical Sciences, 46*(5), 751-781. doi: http://dx.doi.org/10.1016/j.ijmecsci.2004.05.004

Li, D., Hou, H., Chen, C., Zhu, X., Li, M., & Yi, Q. (2018). Experimental study on the combined damage of multi-layered composite structures subjected to close-range explosion of simulated warheads. *International Journal of Impact Engineering, 114*, 133-146. doi: https://doi.org/10.1016/j.ijimpeng.2017.12.007

Li, X., Zhang, X., Guo, Y., Shim, V. P. W., Yang, J., & Chai, G. B. (2018). Influence of fiber type on the impact response of titanium-based fiber-metal laminates.

International Journal of Impact Engineering, 114, 32-42. doi: https://doi.org/10.1016/j.ijimpeng.2017.12.011

Lichtenfeld, J. A., Van Tyne, C. J., & Mataya, M. C. (2006). Effect of strain rate on stress-strain behavior of alloy 309 and 304L austenitic stainless steel. *Metallurgical and Materials Transactions A, 37*(1), 147-161. doi: 10.1007/s11661-006-0160-5

Lundberg, P., Renström, R., & Lundberg, B. (2006). Impact of conical tungsten projectiles on flat silicon carbide targets: Transition from interface defeat to penetration. *International Journal of Impact Engineering, 32*(11), 1842-1856. doi: http://dx.doi.org/10.1016/j.ijimpeng.2005.04.004

Lupker, H. A. (1990). LPG rail tank cars under head-on collisions. *International Journal of Impact Engineering, 9*(3), 359-376. doi: https://doi.org/10.1016/0734-743X(90)90008-J

Manes, A., Serpellini, F., Pagani, M., Saponara, M., & Giglio, M. (2014). Perforation and penetration of aluminium target plates by armour piercing bullets. *International Journal of Impact Engineering, 69*, 39-54. doi: http://dx.doi.org/10.1016/j.ijimpeng.2014.02.010

Maurel-Pantel, A., Fontaine, M., Thibaud, S., & Gelin, J. C. (2012). 3D FEM simulations of shoulder milling operations on a 304L stainless steel. *Simulation Modelling Practice and Theory, 22*, 13-27. doi: https://doi.org/10.1016/j.simpat.2011.10.009

Mines, R. A. W., Roach, A. M., & Jones, N. (1999). High velocity perforation behaviour of polymer composite laminates. *International Journal of Impact Engineering, 22*(6), 561-588. doi: http://dx.doi.org/10.1016/S0734-743X(99)00019-6

Mohagheghian, I., McShane, G. J., & Stronge, W. J. (2015). Impact perforation of monolithic polyethylene plates: Projectile nose shape dependence. *International Journal of Impact Engineering, 80*, 162-176. doi: http://dx.doi.org/10.1016/j.ijimpeng.2015.02.002

Mohan, S., & Velu, S. (2014). Ballistic impact behaviour of unidirectional fibre reinforced composites. *International Journal of Impact Engineering, 63*, 164-176. doi: http://dx.doi.org/10.1016/j.ijimpeng.2013.07.008

Nasto, A., Ajdari, A., Lazarus, A., Vaziri, A., & Reis, P. M. (2013). Localization of deformation in thin shells under indentation. *Soft Matter, 9*(29), 6796-6803. doi: 10.1039/C3SM50279A

Nasto, A., & Reis, P. M. (2014). Localized Structures in Indented Shells: A Numerical Investigation. *Journal of Applied Mechanics, 81*(12), 121008-121008. doi: 10.1115/1.4028804

Nesterenko, V. F., Goldsmith, W., Indrakanti, S. S., & Gu, Y. (2003). Response of hot isostatically pressed Ti–6Al–4V targets to normal impact by conical and blunt projectiles. *International Journal of Impact Engineering, 28*(2), 137-160. doi: http://dx.doi.org/10.1016/S0734-743X(02)00052-0

Nishida, E., Song, B., Maguire, M., Adams, D., Carroll, J., Wise, J., . . . Palmer, T. (2015). Dynamic compressive response of wrought and additive manufactured 304L stainless steels. *EPJ Web of Conferences, 94*, 01001.

Qin, Q., Zheng, X., Zhang, J., Yuan, C., & Wang, T. J. (2018). Dynamic response of square sandwich plates with a metal foam core subjected to low-velocity impact. *International Journal of Impact Engineering, 111*, 222-235. doi: https://doi.org/10.1016/j.ijimpeng.2017.09.011

Ramadhan, A. A., Abu Talib, A. R., Mohd Rafie, A. S., & Zahari, R. (2013). High velocity impact response of Kevlar-29/epoxy and 6061-T6 aluminum laminated panels. *Materials & Design, 43*, 307-321. doi: http://dx.doi.org/10.1016/j.matdes.2012.06.034

Rosenberg, Z., & Dekel, E. (2009). On the deep penetration and plate perforation by rigid projectiles. *International Journal of Solids and Structures, 46*(24), 4169-4180. doi: http://dx.doi.org/10.1016/j.ijsolstr.2009.07.027

Shariati, M., & Allahbakhsh, H. R. (2010). Numerical and experimental investigations on the buckling of steel semi-spherical shells under various loadings. *Thin-Walled Structures, 48*(8), 620-628. doi: https://doi.org/10.1016/j.tws.2010.03.002

Steichen, J. M. (1973). High Strain Rate Tensile Properties of AISI Type 304 Stainless Steel. *Journal of Engineering Materials and Technology, 95*(3), 182-185. doi: 10.1115/1.3443147

Stout, M. G., & Follansbee, P. S. (1986). Strain Rate Sensitivity, Strain Hardening, and Yield Behavior of 304L Stainless Steel. *Journal of Engineering Materials and Technology, 108*(4), 344-353. doi: 10.1115/1.3225893

Tabiei, A., & Nilakantan, G. (2009). Axial crushing of tubes as an energy dissipating mechanism for the reduction of acceleration induced injuries from mine blasts underneath infantry vehicles. *International Journal of Impact Engineering, 36*(5), 729-736. doi: https://doi.org/10.1016/j.ijimpeng.2008.10.004

Tam, L. L., & Calladine, C. R. (1991). Inertia and strain-rate effects in a simple plate-structure under impact loading. *International Journal of Impact Engineering, 11*(3), 349-377. doi: https://doi.org/10.1016/0734-743X(91)90044-G

Tan, V. B. C., & Khoo, K. J. L. (2005). Perforation of flexible laminates by projectiles of different geometry. *International Journal of Impact Engineering, 31*(7), 793-810. doi: http://dx.doi.org/10.1016/j.ijimpeng.2004.04.003

Tasdemirci, A. (2008). The effect of tube end constraining on the axial crushing behavior of an aluminum tube. *Materials & Design, 29*(10), 1992-2001. doi: http://dx.doi.org/10.1016/j.matdes.2008.04.011

Tasdemirci, A., Kara, A., Turan, K., & Sahin, S. (2015). Dynamic crushing and energy absorption of sandwich structures with combined geometry shell cores. *Thin-Walled Structures, 91*, 116-128. doi: http://dx.doi.org/10.1016/j.tws.2015.02.015

Tasdemirci, A., Kara, A., Turan, K., Sahin, S., & Guden, M. (2016). Effect of heat treatment on the blast loading response of combined geometry shell core sandwich structures. *Thin-Walled Structures, 100*, 180-191. doi: http://dx.doi.org/10.1016/j.tws.2015.12.012

Tasdemirci, A., Sahin, S., Kara, A., & Turan, K. (2015). Crushing and energy absorption characteristics of combined geometry shells at quasi-static and dynamic strain rates: Experimental and numerical study. *Thin-Walled Structures, 86*, 83-93. doi: http://dx.doi.org/10.1016/j.tws.2014.09.020

Tasdemirci, A., Tunusoglu, G., & Güden, M. (2012). The effect of the interlayer on the ballistic performance of ceramic/composite armors: Experimental and numerical study. *International Journal of Impact Engineering, 44*, 1-9. doi: http://dx.doi.org/10.1016/j.ijimpeng.2011.12.005

Teng, X., Wierzbicki, T., & Huang, M. (2008). Ballistic resistance of double-layered armor plates. *International Journal of Impact Engineering, 35*(8), 870-884. doi: http://dx.doi.org/10.1016/j.ijimpeng.2008.01.008

Wang, B., Xiong, J., Wang, X., Ma, L., Zhang, G.-Q., Wu, L.-Z., & Feng, J.-C. (2013). Energy absorption efficiency of carbon fiber reinforced polymer laminates under

high velocity impact. *Materials & Design, 50*, 140-148. doi: http://dx.doi.org/10.1016/j.matdes.2013.01.046

Warren, T. L., & Forrestal, M. J. (1998). Effects of strain hardening and strain-rate sensitivity on the penetration of aluminum targets with spherical-nosed rods. *International Journal of Solids and Structures, 35*(28), 3737-3753. doi: http://dx.doi.org/10.1016/S0020-7683(97)00211-4

Warren, T. L., & Tabbara, M. R. (2000). Simulations of the penetration of 6061-T6511 aluminum targets by spherical-nosed VAR 4340 steel projectiles. *International Journal of Solids and Structures, 37*(32), 4419-4435. doi: http://dx.doi.org/10.1016/S0020-7683(99)00148-1

Wei, Z., Yunfei, D., Sheng, C. Z., & Gang, W. (2012). Experimental investigation on the ballistic performance of monolithic and layered metal plates subjected to impact by blunt rigid projectiles. *International Journal of Impact Engineering, 49*, 115-129. doi: http://dx.doi.org/10.1016/j.ijimpeng.2012.06.001

Wen, H. M. (2000). Predicting the penetration and perforation of FRP laminates struck normally by projectiles with different nose shapes. *Composite Structures, 49*(3), 321-329. doi: http://dx.doi.org/10.1016/S0263-8223(00)00064-7

Yang, B., Wang, Z., Zhou, L., Zhang, J., Tong, L., & Liang, W. (2015). Study on the low-velocity impact response and CAI behavior of foam-filled sandwich panels with hybrid facesheet. *Composite Structures, 132*, 1129-1140. doi: http://dx.doi.org/10.1016/j.compstruct.2015.07.058

Zeng, H. B., Pattofatto, S., Zhao, H., Girard, Y., & Fascio, V. (2010). Perforation of sandwich plates with graded hollow sphere cores under impact loading. *International Journal of Impact Engineering, 37*(11), 1083-1091. doi: http://dx.doi.org/10.1016/j.ijimpeng.2010.05.002

Zhang, T. G., & Yu, T. X. (1989). A note on a 'velocity sensitive' energy-absorbing structure. *International Journal of Impact Engineering, 8*(1), 43-51. doi: https://doi.org/10.1016/0734-743X(89)90030-4

Zhao, H., Elnasri, I., & Girard, Y. (2007). Perforation of aluminium foam core sandwich panels under impact loading—An experimental study. *International Journal of Impact Engineering, 34*(7), 1246-1257. doi: http://dx.doi.org/10.1016/j.ijimpeng.2006.06.011

Zhou, X., Mei, Z., & Zhang, Y. (2018). Low-velocity impact response and energy dissipation mechanism of composite multilayer array structures – Experimental and finite element analysis. *Composite Structures, 197*, 89-105. doi: https://doi.org/10.1016/j.compstruct.2018.05.036

Zhu, L., Guo, K., Li, Y., Yu, T. X., & Zhou, Q. (2018). Experimental study on the dynamic behaviour of aluminium foam sandwich plates under single and repeated impacts at low temperature. *International Journal of Impact Engineering, 114*, 123-132. doi: https://doi.org/10.1016/j.ijimpeng.2017.12.001

Zhu, W., Huang, G.-y., Feng, S.-s., & Stronge, W. J. (2018). Conical nosed projectile perforation of polyethylene reinforced cross-ply laminates: Effect of fiber lateral displacement. *International Journal of Impact Engineering, 118*, 39-49. doi: https://doi.org/10.1016/j.ijimpeng.2018.04.005

VITA

Ali Kıvanç Turan was born in Malatya in October 10, 1986. After graduation from Department of Mechanical Engineering-Celal Bayar University, he attended to İzmir Institute of Technology for his M.Sc. and Ph.D. studies. He worked as project and research assistant in the Dynamic Testing and Modeling Laboratory of Mechanical Engineering Department during his studies in both M.Sc and Ph.D. programmes.

Education

- ***Ph.D.*** in English, 2018, Mechanical Engineering, İzmir Institute of Technology.
- ***M.Sc.*** in English, 2012, Mechanical Engineering, İzmir Institute of Technology.
- ***B.Sc.*** in Turkish, 2009, Mechanical Engineering, Celal Bayar University.

Publications

- Taşdemirci, A.; Kara, A.; **Turan, A. K.**; Şahin, S.; Güden, M.; "Effect of heat treatment on the blast loading response of combined geometry shell core sandwich structures", Thin-Walled Structures, 03/2016, **SCI Indexed.**
- Taşdemirci, A.; Kara, A.; **Turan, A. K**.; Şahin, S.; "Dynamic crushing and energy absorption of sandwich structures with combined geometry shell cores", Thin Walled Structures, 06/2015, **SCI Indexed.**
- Taşdemirci, A.; Şahin, S.; Kara, A.; **Turan, A. K.**, "Crushing and energy absorption characteristics of combined geometry shells at quasi-static and dynamic strain rates: Experimental and numerical study", Thin Walled Structures, 01/2015, **SCI Indexed.**
- Demir, M. M.; Horzum, N.; Taşdemirci, A.; **Turan, A. K.**; Güden, M.; "Mechanical Interlocking between Porous Electrospun Polystyrene Fibers and an Epoxy Matrix." , ACS Applied Materials & Interfaces, 12/2014, **SCI Indexed.**
- Taşdemirci, A.; **Turan, A. K.**; Güden, M.; "The effect of strain rate on the mechanical behavior of Teflon foam", Polymer Testing Vol. 31, 09/2012, **SCI Indexed.**